공학박사학위논문

Modal Behavior of a Two-Dimensional Beam with a Transverse Crack: An Analytical Approach Considering Mode I and II Loadings with Experimental Verification Using Surface-Bonded Piezoelectric Wafers

동아대학교 대학원

토 목 공 학 과

임 태 정

2 0 2 3 학 년 도

Modal Behavior of a Two-Dimensional Beam with a Transverse Crack: An Analytical Approach Considering Mode I and II Loadings with Experimental Verification Using Surface-Bonded Piezoelectric Wafers

by
LIM, TAE JEONG

Submitted to

The Graduate School of Dong-A University in Partial Fulfillment
of the Requirements for the degree of Doctor of Engineering
in
Civil Engineering

December 2023

Modal Behavior of a Two-Dimensional Beam with a Transverse Crack: An Analytical Approach Considering Mode I and II Loadings with Experimental Verification Using Surface-Bonded Piezoelectric Wafers

by LIM, TAE JEONG

I have examined the final copy of this dissertation for format and content and recommend that it be accepted in partial fulfillment of the requirements for the degree of Doctor of Engineering, with a major in Civil Engineering.

Committee Chair Dr. Kwang Kyu Choi

We have read this dissertation and recommend its acceptance:

Committee Vice-chair Dr. Hyun Woo Park

Committee Member Dr. Won Ho Kang

Committee Member Dr. Yeun Chul Park

Committee Member Dr. Jin Ho Lee

본 학위 논문은 학위청구자가 주저자 및 공동저자로 참여한 다음의 논문에 기초하여 작성되었으며, 공동저자의 “학술지 게재 논문의 학위논문 작성 동의서”를 득하였음.

This dissertation is written on the basis of the journal published papers in which the current candidate participated as a first author and a co-author. The current candidate acquired “Agreement form on the use of journal published papers” from the co-authors of the papers.

1) H.W. Park, T. Lim, A closed-form frequency equation of an arbitrarily supported beam with a transverse open crack considering axial-bending modal coupling, Journal of Sound and Vibration. 477 (2020) 115336.

2) T. Lim, H.W. Park, Investigating the modal behaviors of a beam with a transverse crack on a high-frequency bending node, International Journal of Mechanical Sciences 221 (2022) 107217.

국문초록

횡균열을 가진 2차원 보의 모달 거동: 균열모드 I 및 II에 대한 하중을 고려한 해석적 접근과 부착형 압전 소자를 이용한 실험적 검증

토목공학과 임 태 정
지도교수 박 현 우

본 논문은 보의 종횡비와 균열 위치에 관계없이 횡균열을 있는 2차원 보의 모드진동수를 예측할 수 있는 새로운 해석모델을 제안한다. 균열보의 모드진동수 예측에 대한 기존의 통상적인 방법은 균열 좌우의 회전각의 불연속만을 고려하여 모드진동수를 예측한다. 기존 방법은 특히 종횡비가 작거나 높은 차수의 굽힘모드에 대한 균열보의 모드 진동수 예측에 오차를 발생시킨다. 구조물 건전성 감시에서 정확한 모드진동수 예측은 필수적이므로 기존 방법의 이러한 한계는 실제 적용에 제약을 초래한다. 따라서 횡균열을 가진 모든 보를 정확하게 해석하고 기존 방법의 한계를 극복할 수 있는 해석 모델이 필요하다.

모드 차수가 높아지거나 보의 종횡비가 작은 경우에는 보의 전단변형과 회전관성이 더욱 중요해짐에 따라 티모센코 보 이론을 기반으로 스펙트럴 해를 제안한다. 2차원 보의 횡방향 열린 균열에서는 균열 좌우에

대한 처짐각 불연속과 함께 균열모드1에 의한 축-굽힘 모드연성과 균열모드2에 의한 전단의 영향이 동시에 발생한다. 이를 바탕으로 축-굽힘-전단 모드연성을 고려한 진동수 방정식을 제안한다. 이 방정식은 균열에서의 회전각, 축변위, 횡변위에 대한 불연속을 나타내는 적합조건식을 사용한다. 제안된 방법은 균열위치와 지점조건을 변화시키며 유한요소해석 및 실험 결과와 비교하여 검증한다. 또한, 계산된 모드진동수를 균열 양쪽의 스펙트럴 해에 적용하여 모드형상을 예측하고 균열열림현상과 전단형상을 시각적으로 분석한다.

본 연구에서는 부착형 압전소자를 사용하여 신호를 주고받아 실험적 검증을 수행한다. 이 접근법은 두 가지 주요 장점을 가지고 있습니다. 첫째, 부착형 압전소자는 축모드와 굽힘모드의 신호를 동시에 얻을 수 있어, 실험의 효율성을 높입니다. 둘째, 이 방법은 차단주파수 이내에서 다양한 진동수를 포괄하는 광대역 신호 측정이 가능하여, 실험적 검증의 범위를 확장할 수 있다.

제안된 방법에 사용된 적합조건식에는 총 5개의 국부유연도가 사용된다. 국부유연도를 선택적으로 사용하여 특정조건에서의 모드진동수를 예측할 수 있는 닫힌 형태의 진동수 방정식을 유도할 수 있다. 첫번째로, 균열모드1에 해당하는 국부유연도만 사용하여 균열이 굽힘모드의 안티노드에 위치하는 경우에 대한 닫힌 형태의 진동수 방정식을 제안한다. 두번째로, 균열모드2에 해당하는 국부유연도만 사용하여 균열이 굽힘모드의 노드에 위치하는 경우의 닫힌 형태의 진동수 방정식을 나타낼 수 있다. 특히 진동수방정식에서 유도된 근사해를 통해 균열이 노드에 위치

하는 경우 진동수 감소가 발생하지 않는다는 기존연구자들의 전제가 성립하지 않음을 규명하였다. 닫힌 형태의 진동수 방정식들은 균열이 보의 중앙에 위치한 경우의 수치예제에 적용하여 유한요소해석과 실험의 결과와 비교하여 검증하였다. 보의 중앙에 위치하게 되면 홀수차모드에서는 균열이 굽힘모드의 안티노드에 위치하고 짝수차모드에서는 균열이 굽힘모드의 노드에 위치하기 때문에 사용하였다. 본 논문에서는 균열의 위치에 따른 역학적 의미를 밝힘으로써 구조물의 손상진단에 중요한 기여를 할 것으로 기대된다.

주요어: 티모센코 보 이론, 균열보, 열린균열모드(균열모드I), 전단균열모드(균열모드II), 모드진동수, 진동수 방정식, 부착형 압전소자, 모드형상, 축-굽힘 모드연성, 손상진단, 구조물건전성감시

Contents

I. Introduction ····· 1
1.1 Research Background ····· 1
1.2 Limitations of Previous Studies ····· 3
1.3 Literature Review ····· 6
1.3.1 Uncoupled Bending Mode ····· 6
1.3.2 Coupled Bending Mode ····· 7
1.4 Significance and Contribution ····· 10
1.5 Objectives and Scopes ····· 12
1.6 Notations ····· 15

II. Cracked Beam with Axial-Bending-Shear Modal Coupling ····· 19
2.1 Cracked Beam Modeling ····· 20
2.1.1 Deriving Local Flexibility ····· 20
2.1.2 Deriving the Compatibility Equation ····· 25
2.1.3 Calculation of F_{ss} ····· 27
2.2 Spectral Solution ····· 29
2.2.1 Axial Motion ····· 29
2.2.2 Bending Motion ····· 29
2.2.3 Dynamic Behaviors ····· 31
2.3 Deriving the Frequency Equation ····· 32
2.4 Frequency Equation in Matrix Form ····· 34
2.5 Newton-Raphson Method for Solving the Nonlinear Equation ····· 36
2.5.1 Newton-Raphson Iteration Process ····· 36
2.5.2 Derivatives Used in the Newton-Raphson Method ····· 37
2.6 Validation ····· 39
2.6.1 Numerical Example ····· 39
2.6.2 Experimental Setup ····· 41
2.6.3 Finite Element Analysis Setup ····· 44
2.6.4 Case 1: Free-Free Beam with a Center Crack ····· 44
2.6.5 Case 2: Free-Free Beam with a Crack at 0.45L Away from the Left End of the Beam ····· 54
2.6.6 Case 3: Cantilever Beam with a Crack at Varying Locations ····· 59

III. Beam with a Crack in the Bending Antinodes ····· 63
3.1 Cracked Beam Modeling ····· 63
3.1.1 Compatibility Equation of the Crack ····· 63
3.1.2 Spectral Solution ····· 64
3.1.3 Dynamic Behaviors ····· 65
3.2 Derivation of the Closed Form Frequency Equation ····· 66
3.2.1 Twelve Equations for Twelve Unknowns ····· 66
3.2.2 Process of Eliminating Unknowns ····· 68
3.2.3 Process of Simplifying Equations ····· 72
3.3 Implication of the Frequency Equation ····· 73
3.4 Extending the Frequency Equation to Other Support Conditions ····· 76
3.5 Newton-Raphson Method for a Solving Nonlinear Equation ····· 80
3.6 Validation ····· 85
3.6.1 Numerical Example ····· 85
3.6.2 Experimental Setup ····· 86
3.6.3 Finite Element Analysis Setup ····· 88
3.6.4 Free-Free Beam with a Crack at the Bending Antinode for an Aspect Ratio of 19.8 ····· 89

IV. Beam with a Crack in the Bending Node ····· 99
4.1 Cracked Beam Modeling Considering Mode II Crack ····· 99
4.1.1 Compatibility Equation of the Crack ····· 99
4.1.2 Spectral Solution ····· 100
4.1.3 Dynamic Behaviors ····· 101
4.2 Derivation of the Closed Form Frequency Equation ····· 102
4.2.1 Eight Equations for Eight Unknowns ····· 102
4.2.2 Process of Eliminating Unknowns ····· 104
4.3 Extending the Frequency Equation to Other Support Conditions ····· 105
4.4 Approximate Solution ····· 107
4.4.1 Derivation Process of the Approximate Solution ····· 107
4.4.2 Approximate Solution Considering Mode II crack ····· 109
4.4.3 Comparison with Approximated Solution Considering Mode I Crack ····· 110
4.5 Newton-Raphson Method for Solving a Nonlinear Equation ····· 113
4.6 Validation ····· 115
4.6.1 Numerical Example ····· 115
4.6.2 Experimental Setup ····· 116
4.6.3 Finite Element Analysis Setup ····· 118

4.6.4 Free-Free Beam with a Crack at the Bending Node for an Aspect Ratio of 19.8 ····· 119

V. Conclusion ····· 129

Appendices ····· 134
References ····· 157
Abstract ····· 169

List of Tables

Table 2.1 K_{ss} evaluated from the contour integral method provided in ABAQUS-standard and g_{ss} obtained from Eq. (2.9c)····· 28
Table 2.2 Contribution of modes I and II crack to the four kinds of vibration modes of a free-free deep beam with a center crack based on the compatibility conditions ····· 41
Table 2.3 Experimental results for the cracked beam in Fig. 2.3(a): (a) The values of experimental modal frequencies of four intact beams (unit: kHz); (b) Fractional reduction in the modal frequency of cracked beams compared to that of the intact beam (unit: %)····· 45
Table 2.4 Experimental results for a cracked beam in Fig. 2.3(b): (a) The values of experimental modal frequencies of four intact beams (unit: kHz); (b) The mean values of the fractional reduction in the modal frequency of cracked beams compared to that of the intact beam (unit: %) ····· 54
Table 3.1 Phase shift at the left and right end of a beam according to support conditions ····· 77
Table 3.2 Phase shift at the left and right end of a beam according to support conditions, differentiated with respect to k_p ····· 84
Table 3.3 Experimental results: (a) mean experimental modal frequencies of intact beams (unit: kHz); (b) mean fractional reduction values in the modal frequency of a cracked beam compared to that of an intact beam (unit: %) ····· 90
Table 4.1 Phase shift at the left and the right end of a beam according to support conditions····· 106
Table 4.2 Experimental results: (a) The mean values of experimental modal frequencies of intact beams (unit: kHz); (b) The mean fractional reduction values

in the modal frequency of cracked beams compared to that of an intact beam (unit: %) ····· 120

List of Figures

<Figure 1.1> Distinction between Timoshenko and Euler-Bernoulli beam theories for the aspect ratio of each mode order for a simply supported beam ····· 2
<Figure 1.2> The compatibility equations used in the conventional method ····· 3
<Figure 1.3> A numerical model of an aluminum beam featuring a crack located at 0.45L from the left end ····· 4
<Figure 1.4> Numerical modal analysis results for a two-dimensional free-free aluminum beam ····· 5
<Figure 1.5> Two-dimensional version of the crack mode ····· 6
<Figure 1.6> Literature review based on the type of beam theory and the presence or absence of modal coupling····· 9
<Figure 1.7> The compatibility equations for modes I and II crack ····· 10
<Figure 2.1> Cracked beam model ····· 20
<Figure 2.2> Unknowns representing axial and bending motions of a cracked beam through a dual coordinate system ····· 31
<Figure 2.3> Numerical example for free-free beams with a transverse crack ·· 40
<Figure 2.4> Experimental setup ····· 43
<Figure 2.5> Comparison of NMF of odd-numbered modes with respect to crack depth ratio ····· 47
<Figure 2.6> Comparison of NMF of even-numbered modes with respect to crack depth ratio ····· 48
<Figure 2.7> Comparison of NMFS with odd-numbered modes for varying crack depth ratios ····· 49
<Figure 2.8> Comparison of NMFS with even-numbered modes for varying crack

depth ratios ····· 51
<Figure 2.9> Mutually exclusive evolution of modes I and II crack in the vicinity of a center crack in a free-free in Fig. 2.3(a) ····· 53
<Figure 2.10> Comparison of NMF with respect to crack depth ratio ····· 55
<Figure 2.11> NMFS with respect to mode number for varying crack depth ratios ····· 57
<Figure 2.12> Combined evolution of modes I and II crack in the vicinity of a crack in a free-free beam in Fig. 2.3(b) ····· 58
<Figure 2.13> Cantilever beam with a transverse crack at varying locations ··· 60
<Figure 2.14> NMFS with respect to mode number for varying crack depth ratios and relative crack locations of the cantilever beam ····· 61
<Figure 3.1> Compatibility equations at the crack in case considering mode I crack ····· 64
<Figure 3.2> Dynamic behaviors of a cracked beam by neglecting all incident evanescent wave modes associated with bending motions ····· 66
<Figure 3.3> ABMC factor for crack depth ratio in Eq. (3.34) ····· 76
<Figure 3.4> The physical implications of t_L and t_R from an axial wave perspective ····· 79
<Figure 3.5> The physical implications of $\bar{t}_L$ and $\bar{t}_R$ from a bending wave perspective ····· 80
<Figure 3.6> Free-free beam with a transverse crack at the center of a beam with an aspect ratio of 19.8 ····· 85
<Figure 3.7> Experimental setup ····· 88
<Figure 3.8> Comparison of modal frequencies proposed by frequency equation to those of finite element analysis and experiments with respect to crack depth ratio ····· 91
<Figure 3.9> Normalized modal frequencies with respect to crack depth ratios 93

<Figure 3.10> Normalized modal frequency shifts with respect to mode number for various crack depth ratios ····· 96
<Figure 3.11> Evolution of ABMC in odd-numbered axial mode shapes with respect to crack depth ratio ····· 98
<Figure 4.1> Compatibility equations at the crack in case considering mode II crack ····· 100
<Figure 4.2> The dynamic behaviors of a cracked beam by omitting all incident evanescent wave motions that are assumed to be negligible ····· 101
<Figure 4.3> NMFS-factor for different support conditions and the simplified NMFS-factor ····· 110
<Figure 4.4> Comparison of simplified NMFS-factors for mode II crack ($\tilde{\psi}_{II}$) and mode I crack ($\tilde{\psi}_{I}$) as a function of frequency normalized by the cut-off frequency ····· 113
<Figure 4.5> Experimental setup ····· 117
<Figure 4.6> Modal frequencies from the proposed frequency equation as a function of the crack depth ratio compared to those from finite element analysis and actual experiments ····· 121
<Figure 4.7> Normalized modal frequencies as a function of crack depth ratios for different bending modes ····· 124
<Figure 4.8> Normalized modal frequency shifts as a function of mode number for different crack depth ratios ····· 126
<Figure 4.9> Evolution of mode II crack in the vicinity of a crack in bending mode shapes as a function of the crack depth ratio for different bending modes ····· 128

Chapter 1
Introduction

1.1 Research Background

Modal analysis of beams has been a continuous subject of study for over 40 years [Chr84, Dim83, Pap88, She90, Dim96]. Within modal analysis, particular emphasis has been placed on the frequency analysis of beams with a transverse open crack, recognizing its importance as a fundamental aspect in the study of structural health monitoring [Fan11, Gom14, She94, Kim03a, Che05]. Examining the modal frequency of a cracked beam is a widely studied topic for damage assessment because it is easy and inexpensive to acquire, providing a low-cost structural assessment method [Sal97]. The prediction of frequency shifts is based on the phenomenon that the frequencies of cracked beams decrease compared to those of intact beams. This phenomenon is not attributed to a reduction in mass but rather to a decrease in local stiffness as a crack develops [Nah05].

Most previous studies have concentrated on modal analysis of the Euler-Bernoulli beam theory, which neglects the effects of shear deformation and rotational inertia [Cho01, Li02, Lee00, Cad09]. Furthermore, these studies focus on the first to third bending modes, which are determinable through modal testing methods such as the impact hammer test [Chi21, Chi01, Kim03b, Mei06]. However, the application of Timoshenko beam theory, which considers the effects of shear deformation and rotational inertia, becomes necessary when examining beams with increased

thickness or higher order modes (Fig. 1.1) [Loy22]. On the basis of the λ/2h = 5 criterion mentioned by Loya et al. [Loy22], Fig. 1.1 illustrates the distinction between Timoshenko and Euler-Bernoulli beams according to the aspect ratio for each mode number of a simply supported intact beam. When the mode wavelength is long compared to the beam thickness (λ/2h > 5), the Euler-Bernoulli beam theory is sufficient. Conversely, when the mode wavelength is short relative to the beam thickness (λ/2h < 5), the application of the Timoshenko beam theory is appropriate. When the aspect ratio exceeds 20, the bending modes up to the typically observed fourth order can be adequately analyzed using the Euler-Bernoulli beam theory. However, when the aspect ratio falls below 20, an accurate analysis becomes impossible without considering the Timoshenko beam theory. Consequently, it is appropriate to adopt the Timoshenko beam theory for a more accurate analysis of all beam types.

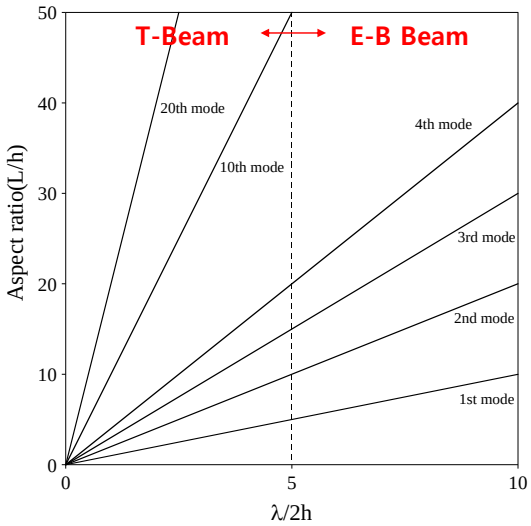


Fig. 1.1 Distinction between Timoshenko and Euler-Bernoulli beam theories for the aspect ratio of each mode order for a simply supported beam.

1.2 Limitations of Previous Studies

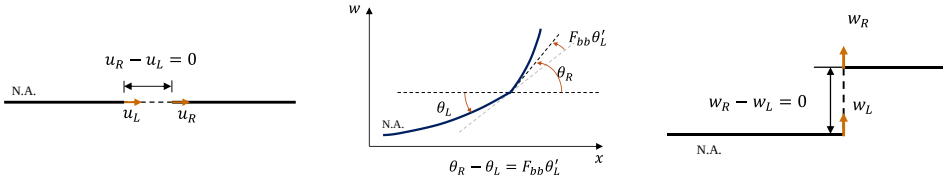
The conventional method used in most previous studies assumed that the frequency reduction of the bending mode in a cracked beam is caused by the discontinuity of the rotation angle at the crack [Car02, Lin04, Der21]. These conventional methods have mainly focused on the open crack. Sometimes, the modal frequencies for axial modes have also been predicted along with the bending modes, similar to the conventional method. The occurrence of a crack results in a frequency decrease, due to discontinuities in axial displacement for axial modes and rotational angle for bending modes. Notably, the axial and bending modes are assumed to be independent and have no effect on each other. Under this assumption, the compatibility equation for the bending behavior can be expressed as follows:

$$\theta_R - \theta_L = F_{bb}\theta_L' \tag{1.1a}$$

$$u_R - u_L = 0 \tag{1.1b}$$

$$w_R - w_L = 0 \tag{1.1c}$$

where θ_R, θ_L, u_R, u_L, w_R, and w_L denote the rotational angle, axial displacement, and transverse displacement of the beam at the right and left sides of a crack, respectively. F_{bb} is the local flexibility coefficient associated with mode I crack. Additionally, $'$ represents the spatial differential operator.



(a) axial displacement (b) rotational angle (c) transverse displacement

Fig. 1.2 The compatibility equations used in the conventional method.

Fig. 1.3 shows a numerical model of an aluminum beam featuring a crack located at 0.45 L from the left end of the beam. The conventional method for predicting cracked beams was applied to the numerical example in Fig. 1.3.

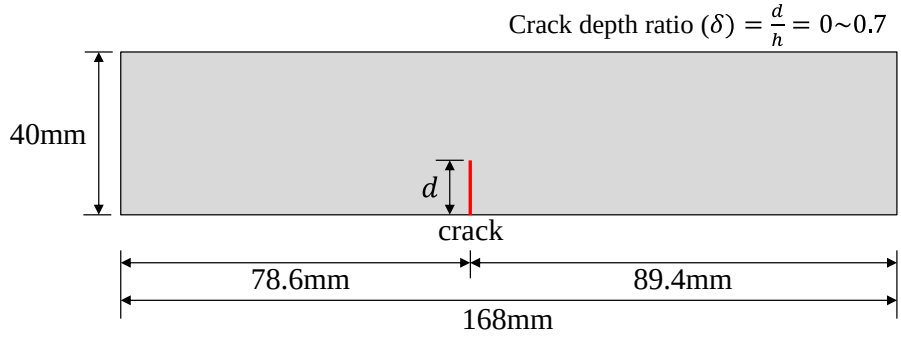
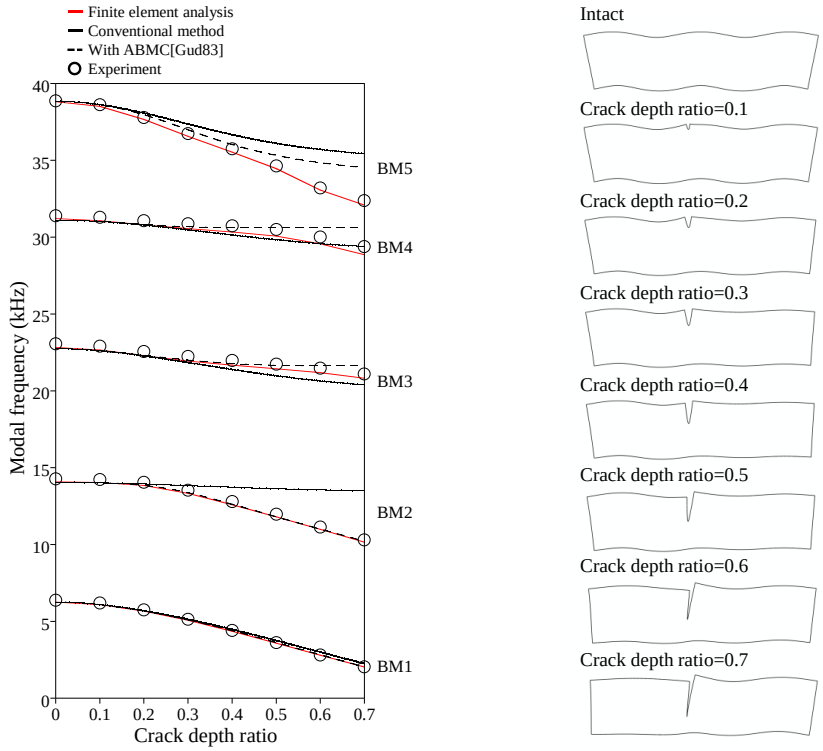


Fig. 1.3 A numerical model of an aluminum beam featuring a crack located at 0.45L from the left end.

The conventional method applied in the numerical example shown in Fig. 1.3 is compared with the results of finite element analysis and experiment, as illustrated in Fig. 1.4(a). This figure presents a comparison of the modal frequencies obtained by the conventional method, finite element analysis and experiment up to the fifth bending mode, which is below the cut-off frequency. The modal frequencies calculated by the finite element analysis, conventional method and experiment are represented by a red solid line, a black solid line and a circle, respectively. Fig. 1.4(a) displays notable discrepancies within the third bending mode, which is the primary observation range, indicating the potential limitations of the conventional method.



(a) modal frequency as a function of crack depth ratio for the bending modes

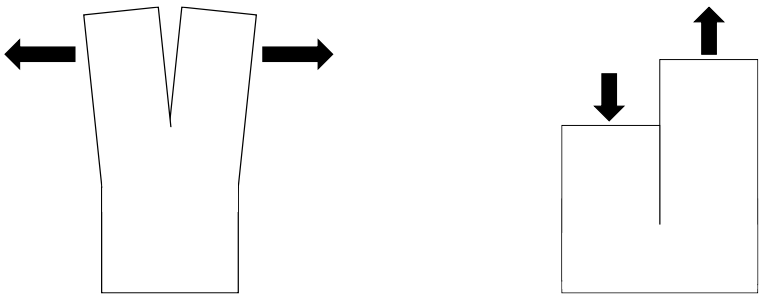
(b) evolution of the fifth bending mode shape for the crack depth ratio.

Fig. 1.4 Numerical modal analysis results for a two-dimensional free-free aluminum beam (bending mode is shown as "BM" on the right axis).

Fig. 1.4(b) shows the evolution of the fifth bending mode shapes with crack depth ratio obtained from the finite element analysis. As soon as a crack occurs, not only bending deformation is observed, but axial deformation also starts to appear in the bending modes from a crack depth ratio of 0.3. As the crack depth ratio reaches 0.5, shear deformation at the crack becomes evident. The mode shapes reveal that the reduction in the modal frequencies of bending modes in a cracked beam is influenced by both axial and shear deformations at the crack. By examining Fig. 1.4, it is clear that the conventional method used in the previous study needs to be re-evaluated.

1.3 Literature Review

In a two-dimensional cracked beam, the crack experiences mode I loading perpendicular to the crack plane, as shown in Fig. 1.5(a), and mode II loading parallel to the crack plane, as shown in Fig. 1.5(b). To prevent nomenclature confusion with vibration modes, the terms “mode I crack” and “mode II crack” are used to refer to the crack caused by mode I loading and mode II loading, respectively. It is important to note that a “mode I crack” refers to a crack caused by mode I loading, not the commonly known “mode I crack propagation” in fatigue fracture. In most studies on the bending modes of cracked beams, the reduction in the modal frequency is assumed to be due to the effects of the mode I crack. Consequently, mode II crack has not been the primary focus of research and is rarely applied in cracked beam studies.



(a) Opening crack mode (b) Sliding crack mode

Fig. 1.5 Two-dimensional version of the crack mode.

1.3.1 Uncoupled Bending Mode (Conventional Method)

Most studies based on the Euler-Bernoulli beam theory, as shown in Fig. 1.2, also assume that the axial and transverse displacements are continuous and that the

frequency reduction occurs only due to the discontinuity in the rotational angle at the crack [Fer02, Fer99, Ost91]. Using the Euler–Bernoulli beam theory, Rizos et al. [Riz90] and Narkis [Nar94] hypothesized a discontinuity in the rotational angles in beams with a single-edge crack to estimate the crack location. Rizos et al. focused on a cantilever support condition, and Narkis focused on a simply supported setup. Similarly, researchers employing the Timoshenko beam theory also align with the Euler-Bernoulli beam theory, which attributes the reduction in frequencies of cracked beams entirely to the discontinuity in the rotational angle [Wan15, Lel02]. Khaji et al. [Kha09] focused on the rotational angles at the crack to predict the modal frequencies at various supports, comparing their results with those of finite element analysis. They also investigated the effect of the aspect ratio of the beam and found significant discrepancies between their results and those of finite element analysis in cases of low aspect ratios. They speculated that these discrepancies could be attributed to inaccuracies in the simulation of crack behavior. In addition, Altunışık et al. [Alt17, Alt19] and Shafiei and Khaji [Sha11] extended their research to predict modal frequencies by applying their methodologies to cases involving multiple cracks.

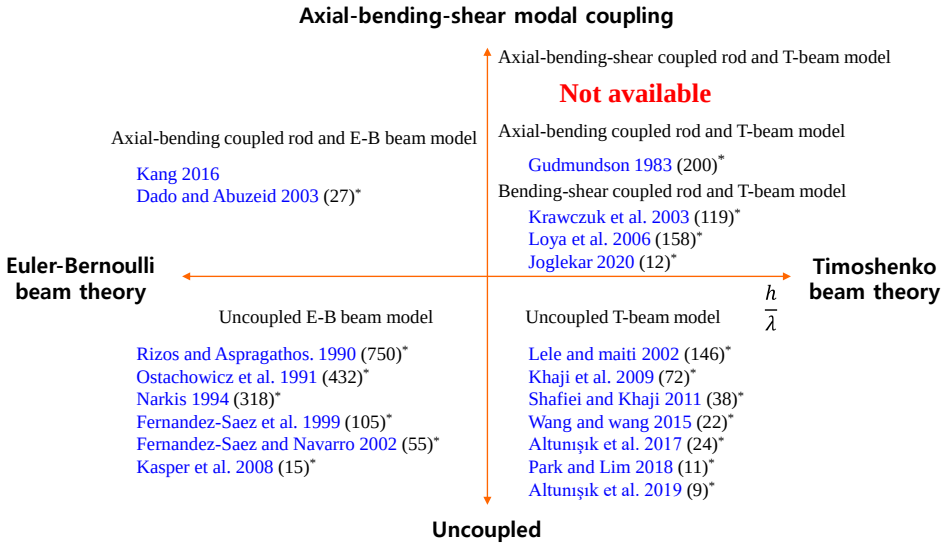
1.3.2 Coupled Bending Mode

Recently, new models have been proposed to investigate the causes of frequency reduction due to cracks by considering various vibration modes or crack modes. Park and Lim [Par18] observed uncoupled bending modes up to the 19th order, whose

frequency exceeded 100 kHz. They observed deviations between the equation and experimental results with increasing in crack depth ratios. This phenomenon was caused by the modal coupling between the axial and bending modes, referred to as axial-bending modal coupling (ABMC). Gudmundson [Gud83] accurately predicted the ABMC between the first axial and the third bending modes of a cracked cantilever beam using the Timoshenko beam theory. Studies using the Euler-Bernoulli beam theory have also addressed the ABMC corresponding to the mode I crack [Kan16, Dad03, Sar14]. Kang et al. [Kan19] derived a closed-form frequency equation for a cracked beam considering the ABMC based on the Euler-Bernoulli beam theory. They accurately predicted the ABMC between the first axial and the fifteenth bending modes of a free-free cracked beam, which was in good agreement with the experimental results. However, studies using the Euler-Bernoulli beam theory have not considered mode II crack. With the introduction of the Timoshenko beam theory, incorporating shear deformation of the beam, research began simultaneously considering both the rotational angle discontinuity at the crack and the transverse displacement discontinuity due to shear deformation [Kim18, Sam19]. Krawczuk et al. [Kra03] introduced a finite spectral element for a cracked Timoshenko beam, specifically for modal and elastic wave propagation analysis. They considered both modes I and II crack to derive the local flexibilities associated with a crack. Loya et al. [Loy06] and Joglekar [Jog20] also based their compatibility equation for the crack on the discontinuity in the rotational angle caused by the mode I crack and the discontinuity in transverse displacement caused by the mode II crack.

We have applied the method considering ABMC to a numerical example in Fig. 1.3 [Gud83]. In Fig. 1.4, the black dashed line represents the cracked beam analyzed using ABMC. The inability to accurately predict all modes, even with the application of ABMC, serves as evidence that the influence of mode II crack must also be considered. An important point to note, however, is the absence of research that addresses axial-bending-shear modal coupling that simultaneously considers the axial-bending modal coupling in mode I crack and the discontinuity in transverse displacement due to mode II crack.

Fig. 1.6 organizes the overall structure of the literature review presented in Section 1.3, categorizing it according to the type of beam theory and the presence or absence of modal coupling.



*Citation metric from the Web of Science (WoS)

Fig. 1.6 Literature review based on the type of beam theory and the presence or absence of modal coupling.

1.4 Significance and Contribution

1. Cracked beam considering modes I and II crack simultaneously

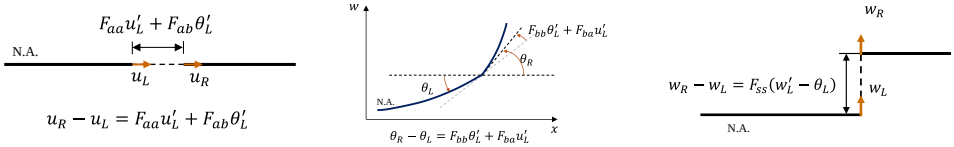
Inspired by the observation of axial and shear deformations in the bending modes in Fig. 1.4(b), it becomes evident that an effective predictive model for all cracked beams with a transverse crack requires the consideration of axial-bending-shear modal coupling. The compatibility equation that satisfies all discontinuities occurring in both modes I and II crack can be expressed as shown in Fig. 1.7.

$$u_R - u_L = F_{aa}u'_L + F_{ab}\theta'_L \quad (1.2a)$$

$$\theta_R - \theta_L = F_{bb}\theta'_L + F_{ba}u'_L \quad (1.2b)$$

$$w_R - w_L = F_{ss}(w'_L - \theta_L) \quad (1.2c)$$

where F_{aa}, F_{ab}, and F_{ba} are the local flexibility coefficients that account for the mode I crack, and F_{ss} is the local flexibility coefficient for the mode II crack.



(a) axial displacement (b) rotational angle (c) transverse displacement

Fig. 1.7 The compatibility equations for modes I and II crack.

Despite the various approaches to consider modes I and II crack, the lack of research that simultaneously addresses both modes in predicting the behavior of cracked beams raises questions. By considering both crack modes, it is expected that an analytical model will be developed that is capable of perfectly predicting all two-dimensional beams with transverse cracks, regardless of frequency range or aspect ratio.

2. Experiments for simultaneous observation of axial and bending modes over a broadband range

Several analytical studies have been conducted to predict the modal frequencies of cracked beams [Lia92, Mor93, Shi99]. In a typical modal frequency measurement experiment to verify this, the type of vibration mode obtained depends on the location of the impact, such as an impact hammer. Therefore, to measure the modal frequencies of the axial and bending modes, conducting experiments with the axial and bending modes separately is necessary. However, in a recent study, piezoelectric wafers made of lead titanate (PZT) were used to measure the modal frequencies of vibration modes [Par03]. These actuator and sensor piezoelectric wafers can generate or sense Lamb waves for structural health monitoring. A Lamb wave is a type of elastic wave that occurs in a thin plate or layer and contains the properties of both symmetric (bending) and anti-symmetric (axial) modes [Liu13]. Therefore, piezoelectric wafers can be used to simultaneously observe the axial and bending modes of the beam. The use of piezoelectric wafers allows the simultaneous measurement of axial and bending modes, which is efficient for observing axial-bending modal coupling.

In addition to the simultaneous measurement of multiple modes, PZT wafers have enabled the capture of modal frequencies of cracked beams at higher frequencies compared with conventional modal testing equipment [Liu20, Bha04, Wor07]. Worden et al. [Wor07] mention that higher modal frequencies are more sensitive to incipient crack initiation in a beam because the size of the crack that can be detected

from the changes in system dynamics is inversely proportional to the frequency range of the excitation. Therefore, to ensure high sensitivity to incipient damage, PZT wafers were used to measure electrical impedance at high frequencies in the range of 30-400 kHz. Consequently, while the primary use of PZT wafers is to detect sensitivity to early-stage cracks, their ability to measure over a wide frequency range further enhances their utility in comprehensive crack detection scenarios.

1.5 Objectives and Scopes

This study presents an analytical model that accurately predicts the behavior of two-dimensional beams with a transverse open crack. This study focused specifically on the analysis of open cracks. The methods and results discussed are only applicable to open crack scenarios and do not extend to other types of cracks, such as closure cracks. The conventional method, which assumes that the frequency reduction in bending modes results solely from discontinuities in the rotational angle at the crack, overlooks the effects of axial-bending modal coupling and the influence of the mode II crack. The proposed method provides a solution to address the limitations of the conventional method, particularly under low aspect ratios or higher frequency ranges.

Chapter 2 presents a frequency equation that accurately predicts the behavior of two-dimensional beams with a transverse crack. This method considers the modal coupling associated with both modes I and II crack, making it applicable across any frequency range or aspect ratio. The compatibility equations are derived from the constitutive equations at the crack and the principles of linear elasticity theory. These

compatibility equations for a crack allow for discontinuities in axial displacement, rotational angle, and transverse displacement, considering the necessity of axial-bending-shear modal coupling. The proposed method for the beam is based on the derivation of spectral solutions from both the Timoshenko beam theory and the elementary rod theory. The axial-bending mode characteristics of modes I and II crack are investigated using the proposed method. Finally, the accuracy of the proposed method is validated through numerical examples for beams with varying crack locations and by comparing the results with experimental data and finite element analysis.

Chapter 3 presents a closed-form frequency equation for beams with a crack located at the bending antinodes. When a crack is located at the bending antinodes, it is only affected by the mode I crack, eliminating the effects of the mode II crack. Since only the mode I crack is considered, the proposed method applies the compatibility equation from Chapter 2 by setting the local flexibility F_{ss} corresponding to the mode II crack to zero. Evanescent waves were not considered to simplify the formula because at high frequencies, evanescent waves have short wavelengths and tend to decay before reaching other supports or cracks. A numerical examples featuring a crack located at the bending antinode is used to validate the proposed method by comparing the results with those of finite element analysis and experimental data across crack depth ratios ranging from 0 to 0.7. In particular, examples with an aspect ratio of 19.8 are used to observe the behavior in the less familiar higher modes.

Chapter 4 presents a closed-form frequency equation for beams with a crack located at the bending node. When a crack is located at the bending node, it is only affected by mode II crack, eliminating the effects of the mode I crack. Since only mode II crack is considered, the proposed method applies the compatibility equation from Chapter 2, with the local flexibilities F_{aa}, F_{bb}, F_{ab}, and F_{ba} corresponding to the mode I crack set to zero. Similar to Chapter 3, the evanescent waves occurring at the cracks or supports are disregarded to enhance the simplicity of the formula. This study uses approximate solutions to investigate how sensitivity to frequency reduction varies in higher modes. A key area of investigation is understanding the causes of the frequency reduction at the bending nodes due to the crack formation. The proposed method is validated by comparison with finite element analysis and experiment. In addition, the mode shapes were examined to visually assess the frequency reduction effects, particularly the influence of mode II cracks at the bending node.

1.6 Notations

The symbols used in this study are defined where they first appear in the txet and whenever clarification is necessary. The most frequently used symbols are listed below.

adj[ ]	Adjugate of the matrix
ω	Angular frequency
u_R	Axial displacement of the beam at the right side of a crack
u_L	Axial displacement of the beam at the left side of a crack
P	Axial force
k	Axial wave number
M	Bending moment
$\bar{k}$	Bending wave numbers
$\Delta\omega$	Change in angular frequency
$\mathbf{C}$	Characteristic matrix
c_{ij}	Compliance coefficient vector
g_{ij}	Corresponding configuration correction factor
g_{aa}	Corresponding configuration correction factor for axial
g_{bb}	Corresponding configuration correction factor for bending
g_{ss}	Corresponding configuration correction factor for shear
α	Crack depth
$\bar{\alpha}$	Crack depth ratio

A	Cross-section of the beam
ρ	Density of the beam
k_{ij}	Displacement jump
a	Distances from the crack to the left end of the beam
b	Distances from the crack to the right end of the beam
E	Elastic modulus
U^c	Energy strain energy due to the crack
U^0	Energy strain energy of the intact
$J(A)$	Energy release rate
k_e	Evanescent bending wave number
$\hat{\varphi}$	group velocity of an intact beam
h	Height of the beam
P_j	Internal force vector
F_{aa}	Local flexibility coefficients associated with mode I crack
F_{ab}, F_{ba}	Local flexibility coefficients associated modal coupling of mode I crack
F_{bb}	Local flexibility coefficient associated with mode I crack
F_{ss}	Local flexibility coefficient associated with mode II crack
d	Maximum crack depth
E'	Modified elastic modulus
$\hat{\psi}_I$	NMFS-factor for the mode I crack
$\hat{\psi}_{II}$	NMFS-factor for the mode II crack

$\widehat{\omega}$	*n*th modal frequency of an intact beam
β_L	Phase shift at the left end of the beam according to support conditions for axial wave
β_R	Phase shift at the right end of the beam according to support conditions for axial wave
$\bar{\beta}_L$	Phase shift at the left end of the beam according to support conditions for bending wave
$\bar{\beta}_R$	Phase shift at the right end of the beam according to support conditions for bending wave
k_p	Propagating bending wave number
$\hat{v}$	Phase velocity of an intact beam
r	Radius of rotation
θ_R	Rotational angle of the beam at the right side of a crack
θ_L	Rotational angle of the beam at the left side of a crack
I	Second moment of inertia
κ	Shear coefficient
V	Shear force
G	Shear modulus
c_q	Shear wave speed
$'$	Spatial differential operator
σ	Stress
k_{ij}	Stiffness matrix
K_{ij}	Stress intensity factor
K_{aa}	Stress intensity factor for axial

K_{bb}	Stress intensity factor for bending
K_{ss}	Stress intensity factor for shear
tr[ ]	Trace of the matrix
w_R	Transverse displacement of the beam at the right side of a crack
w_L	Transverse displacement of the beam at the left side of a crack
$\widehat{\ }$	Variable in which $\omega = \widehat{\omega}$
$\mathbf{w}$	Vector consisting of 12 unknowns
c_0	Wave speed
w	Width of the beam

Chapter 2
Cracked Beam with Axial-Bending-Shear Modal Coupling

A glance at Fig. 1.4 reveals the limited predictive capabilities of conventional methods, particularly in sections affected by axial-bending modal coupling (ABMC) and the influence of mode II crack. In contrast to the conventional method, it is noteworthy that Gudmundson [Gud83] introduced ABMC due to mode I crack, and Loya et al. [Loy06] discussed the modal coupling between mode II crack and the bending of mode I crack. However, both studies have limitations in providing accurate predictions, highlighting the continued necessity to simultaneously consider the effects of modes I and II crack. Nevertheless, as mentioned in the introduction, analytical models that consider both modes I and II crack are rare. Despite over 40 years of research on cracked beams, it raises questions as to why a generic frequency equation has not been developed for two-dimensional beams, irrespective of aspect ratio or crack location. Given the paramount significance of accurate predictions in structural health monitoring, this study proposes an analytical model universally applicable to two-dimensional beams with a transverse crack. The model attempts to provide a frequency equation applicable to any two-dimensional beam with an open transverse edge crack, regardless of its specific characteristics, using compatibility equations that consider both modes I and II crack simultaneously, as exemplified in Eq. (1.2).

2.1 Cracked Beam Modeling

Fig. 2.1 depicts the Timoshenko beam with a transverse crack. The supports are arbitrarily configured as simply supported beams. The crack is positioned at an arbitrary location, denoted at point *C* in Fig. 2.1, with the distances from the crack to the left and right ends of the beam denoted as a and b, respectively. The compatibility equations at the crack include both modes I and II crack, as expressed in Eqs. (1.2a)-(1.2c).

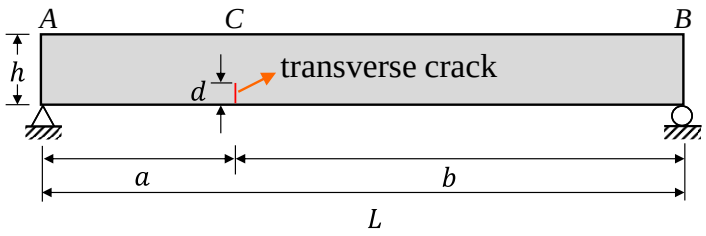


Fig. 2.1 Cracked beam model.

2.1.1 Deriving Local Flexibility

The local flexibility used in Eq. (1.2) can be derived from stress intensity factors, which are fundamental in fracture mechanics. The stress intensity factor for a beam with a transverse crack at the beam edge can be expressed as [Tad73]:

$$K_{ij} = \sigma\sqrt{\pi\alpha}\, g_{ij}(\bar{\alpha}) \tag{2.1}$$

where K_{ij}, σ, α, $\bar{\alpha}$, and g_{ij} represent the stress intensity factor, stress, crack depth, crack depth ratio, and corresponding configuration correction factor, respectively.

Eq. (2.1) expresses the stress intensity factors for a beam under axial force and

bending moment, which are characteristic of the mode I crack, and those resulting from shear force, which are characteristic of the mode II crack.

$$K_{aa} = \frac{P}{wh}\sqrt{\pi\alpha}\, g_{aa}(\bar{\alpha}) \tag{2.2a}$$

$$K_{bb} = \frac{6M}{wh}\sqrt{\pi\alpha}\, g_{bb}(\bar{\alpha}) \tag{2.2b}$$

$$K_{ss} = \frac{\kappa V}{wh}\sqrt{\pi\alpha}\, g_{ss}(\bar{\alpha}) \tag{2.2c}$$

where K_{aa}, K_{bb} and K_{ss} represent the stress intensity factors for axial, bending, and shear, respectively. P, M, and V represent the axial force, bending moment, and shear force, respectively. w and h denote the width and height of the beam, respectively.

The corresponding configuration correction factor was adopted from Tada [Tad19]. However, for g_{ss}, because the stress distribution of shear traction on the crack surface does not follow a parabolic shape in Tada's work, g_{ss} was obtained using finite element analysis software. Further details of this calculation are provided in Section 2.1.3.

$$g_{aa} = \sqrt{\frac{2\tan\left(\frac{\pi\bar{\alpha}}{2}\right)}{\pi\bar{\alpha}}}\,\frac{0.752 + 2.02\bar{\alpha} + 0.37\left\{1.0 - \sin\left(\frac{\pi\bar{\alpha}}{2}\right)\right\}^3}{\cos\left(\frac{\pi\bar{\alpha}}{2}\right)} \tag{2.3a}$$

$$g_{bb} = \sqrt{\frac{2\tan\left(\frac{\pi\bar{\alpha}}{2}\right)}{\pi\bar{\alpha}}}\,\frac{0.923 + 0.199\left\{1.0 - \sin\left(\frac{\pi\bar{\alpha}}{2}\right)\right\}^4}{\cos\left(\frac{\pi\bar{\alpha}}{2}\right)} \tag{2.3b}$$

$$g_{ss} = 2.7432\bar{\alpha}^4 - 0.76215\bar{\alpha}^3 - 3.4008\bar{\alpha}^2 + 4.7267\bar{\alpha} + 0.00063872 \tag{2.3c}$$

The energy release rate $J(A)$ is related to the squared sum of the stress intensity

factors for each crack mode [Dar04].

$$J(A) = \frac{1}{E'}\{(K_{aa} + K_{bb})^2 + (K_{ss})^2\} \tag{2.4}$$

where E' represents the modified elastic modulus. In the case of plane stress, $E' = E$, while for plane strain conditions, E' is defined as $\frac{1-\nu^2}{E}$ with ν being Poisson's ratio.

By substituting Eq. (2.2) into Eq. (2.4), the energy release rate of the plane strain conditions for axial deformation, bending deformation due to mode I crack, and shear deformation due to mode II crack can be represented as follows:

$$\begin{aligned} J(A) = \frac{\pi\alpha}{EA^2}\{&P^2 g_{aa}^2(\bar{\alpha}) + 12MPg_{aa}(\bar{\alpha})g_{bb}(\bar{\alpha}) + 36M^2 g_{bb}^2(\bar{\alpha}) \\ &+ \kappa^2 V^2 g_{ss}^2(\bar{\alpha})\} \end{aligned} \tag{2.5}$$

Using fracture mechanics principles, the elastic strain energy due to the crack can be determined from the energy release rate.

$$U^c = \int_A J(A)dA \tag{2.6}$$

where U^c represents the elastic strain energy due to the crack.

The strain energy at the crack in a two-dimensional beam is represented by substituting Eq. (2.5) into Eq. (2.6).

$$\begin{aligned} U^c = \int_0^d \int_{-\frac{w}{2}}^{\frac{w}{2}} \frac{\pi\alpha}{EA^2}\{&P^2 g_{aa}^2(\bar{\alpha}) + 12MPg_{aa}(\bar{\alpha})g_{bb}(\bar{\alpha}) + 36M^2 g_{bb}^2(\bar{\alpha}) \\ &+ \kappa^2 V^2 g_{ss}^2(\bar{\alpha})\}d\alpha d\beta \end{aligned} \tag{2.7}$$

where d are the maximum crack depth, respectively. The area integral is performed

over microelements with the vertical axis defined as α and the horizontal axis as β, for the crack depth "d" and width "w".

The compliance coefficients are derived using Castigliano's theorem, and the process is elaborated in Appendix (A1) [Pap87].

$$c_{ij} = \frac{\partial^2 U^c}{\partial P_i \partial P_j} \tag{2.8}$$

The compliance coefficients for the axial mode, bending mode, axial-bending modal coupling due to mode I crack, and shear mode due to mode II crack can be formulated as follows:

$$c_{aa} = \frac{\partial^2}{\partial P \partial P}\int_0^d \int_{-\frac{w}{2}}^{\frac{w}{2}} \frac{\pi\alpha}{EA^2}\left\{P^2 g_{aa}^2(\bar{\alpha}) + 12MP g_{aa}(\bar{\alpha}) g_{bb}(\bar{\alpha}) + 36M^2 g_{bb}^2(\bar{\alpha}) + \kappa^2 V^2 g_{ss}^2(\bar{\alpha})\right\} d\alpha d\beta \tag{2.9a}$$

$$c_{bb} = \frac{\partial^2}{\partial M \partial M}\int_0^d \int_{-\frac{w}{2}}^{\frac{w}{2}} \frac{\pi\alpha}{EA^2}\left\{P^2 g_{aa}^2(\bar{\alpha}) + 12MP g_{aa}(\bar{\alpha}) g_{bb}(\bar{\alpha}) + 36M^2 g_{bb}^2(\bar{\alpha}) + \kappa^2 V^2 g_{ss}^2(\bar{\alpha})\right\} d\alpha d\beta \tag{2.9b}$$

$$c_{ab} = c_{ba} = \frac{\partial^2}{\partial P \partial M}\int_0^d \int_{-\frac{w}{2}}^{\frac{w}{2}} \frac{\pi\alpha}{EA^2}\left\{P^2 g_{aa}^2(\bar{\alpha}) + 12MP g_{aa}(\bar{\alpha}) g_{bb}(\bar{\alpha}) + 36M^2 g_{bb}^2(\bar{\alpha}) + \kappa^2 V^2 g_{ss}^2(\bar{\alpha})\right\} d\alpha d\beta \tag{2.9c}$$

$$c_{ss} = \frac{\partial^2}{\partial V \partial V}\int_0^d \int_{-\frac{w}{2}}^{\frac{w}{2}} \frac{\pi\alpha}{EA^2}\left\{P^2 g_{aa}^2(\bar{\alpha}) + 12MP g_{aa}(\bar{\alpha}) g_{bb}(\bar{\alpha}) + 36M^2 g_{bb}^2(\bar{\alpha}) + \kappa^2 V^2 g_{ss}^2(\bar{\alpha})\right\} d\alpha d\beta \tag{2.9d}$$

$$c_{sa} = c_{sa} = \frac{\partial^2}{\partial V \partial P}\int_0^d \int_{-\frac{w}{2}}^{\frac{w}{2}} \frac{\pi\alpha}{EA^2}\left\{P^2 g_{aa}^2(\bar{\alpha}) + 12MP g_{aa}(\bar{\alpha}) g_{bb}(\bar{\alpha}) + 36M^2 g_{bb}^2(\bar{\alpha}) + \kappa^2 V^2 g_{ss}^2(\bar{\alpha})\right\} d\alpha d\beta \tag{2.9e}$$

$$c_{sb} = c_{bs} = \frac{\partial^2}{\partial V \partial M} \int_0^d \int_{-\frac{w}{2}}^{\frac{w}{2}} \frac{\pi\alpha}{EA^2} \{P^2 g_{aa}^2(\bar{\alpha}) + 12MP g_{aa}(\bar{\alpha}) g_{bb}(\bar{\alpha}) + 36M^2 g_{bb}^2(\bar{\alpha}) + \kappa^2 V^2 g_{ss}^2(\bar{\alpha})\} d\alpha d\beta \tag{2.9f}$$

The compliance coefficients corresponding to modes I and II crack can be expressed by rearranging Eq. (2.9).

$$c_{aa} = \frac{2\pi h}{EA} \int_0^{\bar{d}} \bar{\alpha}\, g_{aa}^2 d\bar{\alpha} \tag{2.10a}$$

$$c_{bb} = \frac{6\pi h}{EI} \int_0^{\bar{d}} \bar{\alpha}\, g_{bb}^2 d\bar{\alpha} \tag{2.10b}$$

$$c_{ab} = c_{ba} = \frac{\pi h^2}{EI} \int_0^{\bar{d}} \bar{\alpha}\, g_{aa} g_{bb} d\bar{\alpha} \tag{2.10c}$$

$$c_{ss} = \frac{2\pi\kappa^2 h}{EA} \int_0^{\bar{d}} \bar{\alpha} g_{ss}^2\, d\bar{\alpha} \tag{2.10d}$$

$$c_{sa} = c_{as} = c_{sb} = c_{bs} = 0 \tag{2.10e}$$

where $\bar{d} = \frac{d}{h}$ denotes the maximum crack depth ratio. Eq. (2.10e) represents the compliance coefficient for modal coupling between modes I and II crack, which has a value of zero. This indicates that there is no modal coupling by compliance due to the different crack modes.

The local flexibility corresponding to modes I and II crack is the product of the compliance factor and stiffness parameter, which can be expressed in matrix form as follows:

$$\begin{bmatrix} F_{aa} & F_{ab} & 0 \\ F_{ba} & F_{bb} & 0 \\ 0 & 0 & F_{ss} \end{bmatrix} = \begin{bmatrix} EAc_{aa} & EIc_{ab} & 0 \\ EAc_{ba} & EIc_{bb} & 0 \\ 0 & 0 & -\kappa GAc_{ss} \end{bmatrix} \tag{2.11}$$

where the local flexibility matrix is obtained by deriving the compatibility equation

in Section 2.1.2. Because $c_{sa} = c_{as} = c_{sb} = c_{bs} = 0$, F_{sa}, F_{as}, F_{sb}, and F_{bs} were left out.

Substituting Eq. (2.10) into Eq. (2.11) yields the local flexibilities corresponding to modes I and II crack, as required for Eq. (1.2).

$$F_{aa} = 2\pi h \int_0^{\bar{\alpha}} \bar{\alpha}\, g_{aa}^2 d\bar{\alpha} \tag{2.12a}$$

$$F_{bb} = 6\pi h \int_0^{\bar{\alpha}} \bar{\alpha}\, g_{bb}^2 d\bar{\alpha} \tag{2.12b}$$

$$F_{ab} = \pi h^2 \int_0^{\bar{\alpha}} \bar{\alpha}\, g_{aa} g_{bb} d\bar{\alpha} \tag{2.12c}$$

$$F_{ba} = 12\pi \int_0^{\bar{\alpha}} \bar{\alpha}\, g_{aa} g_{bb} d\bar{\alpha} \tag{2.12d}$$

$$F_{ss} = \frac{\pi \kappa^3 h}{(1+\nu)} \int_0^{\bar{\alpha}} \bar{\alpha} g_{ss}^2\, d\bar{\alpha} \tag{2.12e}$$

2.1.2 Deriving the Compatibility Equation

The compatibility equations in Eq. (1.2) can be obtained by employing the constitutive equation of the crack combined with the linear elasticity theory of the beam.

The constitutive equation of the crack is expressed as follows [Dad03]:

$$P_j = k_{ij} \Delta u_j \tag{2.13}$$

where P_j, k_{ij} and Δu_j denote the internal force, stiffness matrix, and displacement jump, respectively. i and j represent the direction of the forces or displacements, respectively.

The displacement jump in Eq. (2.13) can be rewritten using the compliance coefficients, which are the inverses of the stiffness vector.

$$u_i^R - u_i^L = c_{ij} P_j \tag{2.14}$$

where c_{ij} is the compliance coefficient, representing the inverse of the stiffness matrix (k_{ij}).

Eq. (2.14) can be expanded to include the displacements, compliance coefficients and internal forces that occur at the crack due to modes I and II crack.

$$\begin{Bmatrix} u_R - u_L \\ \theta_R - \theta_L \\ w_R - w_L \end{Bmatrix} = \begin{bmatrix} c_{aa} & c_{ab} & c_{as} \\ c_{ba} & c_{bb} & c_{bs} \\ c_{sa} & c_{sb} & c_{ss} \end{bmatrix} \begin{Bmatrix} P \\ M \\ V \end{Bmatrix} \tag{2.15}$$

where aa, bb, and ss denote the axial, bending, and shear, respectively, while ab(or ba), as(or sa), and bs(or sb) denote the axial-bending, bending-shear, and axial-shear modal couplings (i.e., c_{ab} is the compliance coefficient corresponding to the axial mode influenced by bending, c_{ba} is the compliance coefficient for bending mode influenced by axial). Due to the absence of modal coupling between distinct crack modes, specifically between modes I and II crack, the compliance coefficients c_{as}, c_{sa}, c_{bs}, and c_{sb} are zero, according to Castigliano's theorem, as expressed in Eq. (2.10).

$$\begin{Bmatrix} u_R - u_L \\ \theta_R - \theta_L \\ w_R - w_L \end{Bmatrix} = \begin{bmatrix} c_{aa} & c_{ab} & 0 \\ c_{ba} & c_{bb} & 0 \\ 0 & 0 & c_{ss} \end{bmatrix} \begin{Bmatrix} P \\ M \\ V \end{Bmatrix} \tag{2.16}$$

The internal force is obtained from the linear elasticity theory of the beam.

$$\begin{Bmatrix} P \\ M \\ V \end{Bmatrix} = \begin{Bmatrix} EAu_L' \\ EI\theta_L' \\ -\kappa GA(w_L' - \theta_L) \end{Bmatrix} \tag{2.17}$$

where E, I, G, κ, and A denote the elastic modulus, second moment of inertia, shear modulus, shear coefficient, and cross-section of the beam, respectively.

Substituting Eq. (2.17) into Eq. (2.16) gives:

$$\begin{Bmatrix} u_R - u_L \\ \theta_R - \theta_L \\ w_R - w_L \end{Bmatrix} = \begin{bmatrix} c_{aa} & c_{ab} & 0 \\ c_{ba} & c_{bb} & 0 \\ 0 & 0 & c_{ss} \end{bmatrix} \begin{Bmatrix} EAu_L' \\ EI\theta_L' \\ -\kappa GA(w_L' - \theta_L) \end{Bmatrix} \tag{2.18}$$

By inserting the stiffness parameter in Eq. (2.18) into the compliance coefficient matrix and expressing it in terms of the local flexibility matrix in Eq. (2.11), the compatibility equation can be expressed as follows:

$$\begin{Bmatrix} u_R - u_L \\ \theta_R - \theta_L \\ w_R - w_L \end{Bmatrix} = \begin{bmatrix} F_{aa} & F_{ab} & 0 \\ F_{ba} & F_{bb} & 0 \\ 0 & 0 & F_{ss} \end{bmatrix} \begin{Bmatrix} u_L' \\ \theta_L' \\ w_L' - \theta_L \end{Bmatrix} \tag{2.19}$$

2.1.3 Calculation of F_{ss}

The local flexibility F_{ss} corresponding to the mode II crack includes the corresponding configuration correction factor g_{ss}, which accounts for the shear traction acting on the crack surface. In Tada [Tad73], g_{ss} is based on the assumption that shear stress is either uniformly distributed across the crack surface or concentrated. However, upon applying a vertical load to the free end of the cantilevered beam with a center crack through a finite element analysis program and the crack surface was examined, it was found that the shear traction has a parabolic distribution.

g_{ss} is closely related to the stress intensity factor K_{ss} in Eq. (2.9c). The value of K_{ss} with parabolic shear traction distribution can be calculated using the

commercial finite element package ABAQUS-Standard [Lee18]. A unit vertical load is applied to the free end of a cantilever beam with a central crack and the stress intensity factor K_{ss} is determined for each crack depth ratio using the contour integral method in the finite element analysis program. The crack depth ratio varied from 0.1–0.7, and the size of the beam used for this analysis was b= 198 mm, h= 10 mm. g_{ss} can be calculated by inserting the dimensions of the beam and the load value (V = 1) into Eq. (2.9c).

Table 2.1 shows K_{ss} evaluated from the contour integral method provided in ABAQUS-standard and g_{ss} obtained from Eq. (2.9c).

Table 2.1 K_{ss} evaluated from the contour integral method provided in ABAQUS-standard and g_{ss} obtained from Eq. (2.9c)

Crack depth ratio	K_{ss} $(\mathrm{N}\cdot\mathrm{m}^{-\frac{3}{2}})$	g_{ss}
0.1	209.68	0.44040
0.2	544.63	0.80886
0.3	915.09	1.1097
0.4	1305.7	1.3712
0.5	1695.8	1.5928
0.6	2098.9	1.7997
0.7	2571.3	2.0412

g_{ss} is expressed as a fifth-order polynomial for the crack depth ratio $\bar{\alpha}$ by interpolating the numerical results in Table 2.1:

$$g_{ss} = 2.7432\bar{\alpha}^4 - 0.76215\bar{\alpha}^3 - 3.4008\bar{\alpha}^2 + 4.7267\bar{\alpha} + 0.00063872 \tag{2.20}$$

F_{ss} obtained by substituting Eq. (2.20) into Eq. (2.12e) is calculated using the Gauss quadrature rule.

2.2 Spectral Solution

2.2.1 Axial Motion

Based on the elementary rod theory, the axial wave motion in a beam is described by the following dispersion equation:

$$\frac{\omega}{k} = \sqrt{\frac{E}{\rho}} \tag{2.21}$$

where ρ, ω, and k denote the density of the beam, angular frequency, and axial wave number, respectively.

The spectral solution for the axial displacements along the neutral axis of the beam is structured in two parts at each side of the crack [Doy89].

$$u_L(x_1) = A_1 e^{-ik(a-x_1)} + A_2 e^{-ikx_1} \tag{2.22a}$$

$$u_R(x_2) = B_1 e^{-ikx_2} + B_2 e^{-ik(b-x_2)} \tag{2.22b}$$

where A_1, A_2, B_1, and B_2 represent the propagating bending wave motions.

2.2.2 Bending Motion

Based on the Timoshenko beam theory, the bending wave motion in a beam is described by the following dispersion equation [Fun65].

$$\bar{k}^4 - \omega^2 \left(\frac{1}{c_0^2} + \frac{1}{c_q^2} \right) \bar{k}^2 + \left(\frac{\omega^4}{c_0^2 c_q^2} - \frac{\omega^2}{c_0^2 r^2} \right) = 0 \tag{2.23}$$

where $\bar{k}$ represent the bending wave numbers. c_0, c_q, and r denote the wave speed, shear wave speed, and radius of rotation, respectively.

$$c_0^2 = \frac{E}{\rho},\ c_q^2 = \frac{\kappa G}{\rho},\ r^2 = \frac{I}{A} \tag{2.24}$$

There are two types of k_p and k_e represent the propagating and the evanescent bending wave numbers, respectively. However, it is important to note that the following equation is valid only when the modal frequency is below the cut-off frequency ($\frac{c_q}{r}$).

$$k_p = \sqrt{\frac{X + \sqrt{X^2 - 4Y}}{2}} \tag{2.25a}$$

$$k_e = \sqrt{\frac{-X + \sqrt{X^2 - 4Y}}{2}} \tag{2.25b}$$

where X and Y are parameters representing common values used to simplify the expression of the bending wave number and are composed as follows:

$$X = \omega^2 \left(\frac{1}{c_0^2} + \frac{1}{c_q^2} \right) \tag{2.26a}$$

$$Y = \frac{\omega^4}{c_0^2 c_q^2} - \frac{\omega^2}{c_0^2 r^2} \tag{2.26b}$$

Similar to Eq. (2.22), the spectral solution for transverse displacements and the rotation angle of the beam is divided into two parts corresponding to the left and right sides of the crack [Mei05].

$$w_L(x_1) = A_3 e^{-ik_p(a-x_1)} + A_4 e^{-ik_p x_1} + A_5 e^{-k_e(a-x_1)} + A_6 e^{-k_e x_1} \tag{2.27a}$$

$$w_R(x_2) = B_3 e^{-ik_p x_2} + B_4 e^{-ik_p(b-x_2)} + B_5 e^{-k_e x_2} + B_6 e^{-k_e(b-x_2)} \tag{2.27b}$$

$$\theta_L(x_1) = -iPA_3 e^{-ik_p(a-x_1)} + iPA_4 e^{-ik_p x_1} - NA_5 e^{-k_e(a-x_1)} + NA_6 e^{-x_1} \tag{2.27c}$$

$$\theta_R(x_2) = -iPB_3 e^{-ik_p x_2} + iPB_4 e^{-ik_p(b-x_2)} - NB_5 e^{-k_e x_2} + NB_6 e^{-k_e(b-x_2)} \tag{2.27d}$$

where A_3, A_4, B_3, and B_4 represent the propagating bending wave motions while A_5, A_6, B_5, and B_6 represent the evanescent bending wave motions. P and N are the coefficients relating the rotational angles to the transverse displacement, respectively.

$$P = k_p\left(1 - \frac{\omega^2}{k_p^2 c_q^2}\right) \tag{2.28a}$$

$$N = k_e\left(1 + \frac{\omega^2}{k_e^2 c_q^2}\right) \tag{2.28b}$$

2.2.3 Dynamic Behaviors

Eq. (2.22) contains four unknowns—A_1, A_2, B_1, and B_2—all of which represent propagating axial motions. In contrast, Eq. (2.27) contains eight unknowns : A_3, A_4, A_5, A_6, B_3, B_4, B_5, and B_6. Among these, A_3, A_4, B_3, and B_4 correspond to propagating bending motions, whereas A_5, A_6, B_5, and B_6 are associated with evanescent bending motions. Fig. 2.2. shows unknowns representing axial and bending motions of a cracked beam through a dual coordinate system.

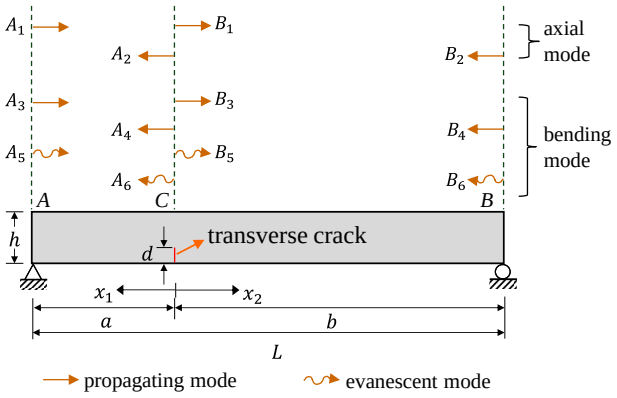


Fig. 2.2 Unknowns representing axial and bending motions of a cracked beam through a dual coordinate system.

2.3 Deriving the Frequency Equation

There are a total of twelve unknowns in Eqs. (2.22) and (2.27). The frequency equation can be derived using twelve equations that satisfy these unknowns, including three compatibility conditions, three equilibrium equations at the crack, and the boundary conditions at each support.

The compatibility equations representing the discontinuities in the axial displacement, transverse displacement, and rotational angle on both sides of the crack are as follows:

(i) Compatibility of axial displacement

$$u_R - u_L = F_{aa}u'_L + F_{ab}\theta'_L$$

$$\begin{aligned}\Rightarrow (1 - ikF_{aa})A_1e^{-ika} + (1 + ikF_{aa})A_2 - F_{ab}(k_pPA_3e^{-ik_pa} \\ + k_pPA_4 - k_eNA_5e^{-k_ea} - k_eNA_6) - B_1 - B_2e^{-ikb} \\ = 0\end{aligned} \tag{2.29}$$

(ii) Compatibility of transverse displacement

$$w_R - w_L = F_{ss}(w'_L - \theta_L)$$

$$\begin{aligned}\Rightarrow \{1 - i(k_p - P)F_{ss}\}A_3e^{-ik_pa} + \{1 + i(k_p - P)F_{ss}\}A_4 \\ + \{1 - (k_e - N)F_{ss}\}A_5e^{-k_ea} + \{1 + (k_e - N)F_{ss}\}A_6 \\ - B_3 - B_4e^{-ik_pb} - B_5 - B_6e^{-k_eb} = 0\end{aligned} \tag{2.30}$$

(iii) Compatibility of rotational angle

$$\theta_R - \theta_L = F_{bb}\theta'_L + F_{ba}u'_L$$

$$\begin{aligned}\Rightarrow ikF_{ba}(A_1e^{-ika} - A_2) + (iP + k_pPF_{bb})A_3e^{-ik_pa} \\ - (iP - k_pPF_{bb})A_4 + (N - k_eNF_{bb})A_5e^{-k_ea} \\ - (N + k_eNF_{bb})A_6 - iPB_3 + iPB_4e^{-ik_pb} - NB_5 \\ + NB_6e^{-k_eb} = 0\end{aligned} \tag{2.31}$$

The equilibrium equations considering the continuities of the axial force, shear force, and moment on both sides of the crack are as follows:

(i) Axial force equilibrium

$$\begin{gathered} EAu_L' = EAu_R' \\ \Rightarrow A_1 e^{-ika} - A_2 - B_1 + B_2 e^{-ikb} = 0 \end{gathered} \tag{2.32}$$

(ii) Shear force equilibrium

$$\begin{gathered} \kappa GA(-w_L' + \theta_L + w_R' - \theta_R) = 0 \\ \Rightarrow -i\big(P - k_p\big)A_3 e^{-ik_p a} + i\big(P - k_p\big)A_4 + (k_e - N)A_5 e^{-k_e a} \\ - (k_e - N)A_6 + i\big(P - k_p\big)B_3 - i\big(P - k_p\big)B_4 e^{-ik_p b} \\ - (k_e - N)B_5 + (k_e - N)B_6 e^{-k_e b} = 0 \end{gathered} \tag{2.33}$$

(iii) Moment equilibrium

$$\begin{gathered} EI\theta_L' = EI\theta_R' \\ \Rightarrow k_p P A_3 e^{-ik_p a} + k_p P A_4 - k_e N A_5 e^{-k_e a} - k_e N A_6 - k_p P B_3 \\ - k_p P B_4 e^{-ik_p b} + k_e N B_5 + k_e N B_6 e^{-k_e b} = 0 \end{gathered} \tag{2.34}$$

The equilibrium and compatibility equations at the crack are identical for a beam with a transverse crack at the beam's edge. However, the boundary conditions differ depending on the configuration of the supports. The boundary conditions for each support condition, except the simply supported condition, are detailed in Appendix (A2). For the simply supported beam discussed in Fig. 2.1, the boundary conditions at Support A and Support B on both sides of the crack are as follows:

(i) Axial displacement boundary condition at *A*

$$\begin{gathered} u_L = 0 \\ \Rightarrow A_1 e^{ika} = -A_2 \end{gathered} \tag{2.35}$$

(ii) Transverse displacement boundary condition at *A*

$$\begin{gathered} w_L = 0 \\ \Rightarrow A_3 + A_4 e^{-ik_p a} + A_5 + A_6 e^{-k_e a} = 0 \end{gathered} \tag{2.36}$$

(iii) Moment boundary condition at *A*

$$\begin{gathered} EI\theta_L' = 0 \\ \Rightarrow -k_p P A_3 - k_p P A_4 e^{-ik_p a} + k_e N A_5 + k_e N A_6 e^{-k_e a} = 0 \end{gathered} \tag{2.37}$$

(iv) Axial force boundary condition at *B*

$$\begin{gathered} EAu_R' = 0 \\ \Rightarrow B_2 = B_1 e^{-ikb} \end{gathered} \tag{2.38}$$

(v) Transverse displacement boundary condition at *B*

$$\begin{gathered} w_R = 0 \\ \Rightarrow B_3 e^{-ik_p b} + B_4 + B_5 e^{-k_e b} + B_6 = 0 \end{gathered} \tag{2.39}$$

(vi) Moment boundary condition at *B*

$$\begin{gathered} EI\theta_R' = 0 \\ \Rightarrow -k_p P B_3 e^{-ik_p b} - k_p P B_4 + k_e N B_5 e^{-k_e b} + k_e N B_6 = 0 \end{gathered} \tag{2.40}$$

2.4 Frequency Equation in Matrix Form

Eqs. (2.29) to (2.40) can be expressed in a matrix equation as follows:

$$\mathbf{Cw} = \mathbf{0} \tag{2.41}$$

where $\mathbf{C}$ and $\mathbf{w}$ represent the characteristic matrix and vector consisting of 12 unknowns (i.e., $A_1 - A_6$ and $B_1 - B_6$), respectively. The non-zero components c_{ij}

in the characteristic matrix $\mathbf{C}$ of a simply supported condition can be represented by the twelve equations from Eqs. (2.29) to (2.40).

$$
\begin{aligned}
&c_{1,1} = (1 - ikF_{aa})e^{-ika},\ c_{1,2} = 1 + ikF_{aa},\ c_{1,3} = -F_{ab}k_pPe^{-ik_pa} \\
&c_{1,4} = -F_{ab}k_pP,\ c_{1,5} = F_{ab}k_eNe^{-k_ea},\ c_{1,6} = F_{ab}k_eN,\ c_{1,7} = -1 \\
&c_{1,8} = -e^{-ikb},\ c_{2,3} = \{1 - i(k_p - P)F_{ss}\}e^{-ik_pa} \\
&c_{2,4} = i(k_p - P)F_{ss} + 1,\ c_{2,5} = \{-(k_e - N)F_{ss} + 1\}e^{-k_ea} \\
&c_{2,6} = (k_e - N)F_{ss} + 1,\ c_{2,9} = -1,\ c_{2,10} = -e^{-ik_pb},\ c_{2,11} = -1 \\
&c_{2,12} = -e^{-k_eb},\ c_{3,1} = ikF_{ba}e^{-ika},\ c_{3,2} = -ikF_{ba} \\
&c_{3,3} = (iP + k_pPF_{bb})e^{-ik_pa},\ c_{3,4} = -iP + k_pPF_{bb} \\
&c_{3,5} = (N - k_eNF_{bb})e^{-k_ea},\ c_{3,6} = -N - k_eNF_{bb},\ c_{3,9} = -iP \\
&c_{3,10} = iPe^{-ik_pb},\ c_{3,11} = -N,\ c_{3,12} = Ne^{-k_eb},\ c_{4,1} = e^{-ika} \\
&c_{4,2} = -1,\ c_{4,7} = -1,\ c_{4,8} = e^{-ikb},\ c_{5,3} = -i(P - k_p)e^{-ik_pa} \\
&c_{5,4} = i(P - k_p),\ c_{5,5} = (k_e - N)e^{-ik_ea},\ c_{5,6} = -(k_e - N) \\
&c_{5,9} = i(P - k_p),\ c_{5,10} = -i(P - k_p)e^{-ik_pb},\ c_{5,11} = -(k_e - N) \\
&c_{5,12} = (k_e - N)e^{-k_eb},\ c_{6,3} = k_pPe^{-ik_pa},\ c_{6,4} = k_pP \\
&c_{6,5} = -k_eNe^{-k_ea},\ c_{6,6} = -k_eN,\ c_{6,9} = -k_pP \\
&c_{6,10} = -k_pPe^{-ik_pb},\ c_{6,11} = k_eN,\ c_{6,12} = k_eNe^{-k_eb},\ c_{7,1} = e^{ika} \\
&c_{7,2} = 1,\ c_{8,3} = 1,\ c_{8,4} = e^{-ik_pa},\ c_{8,5} = 1,\ c_{8,6} = e^{-k_ea} \\
&c_{9,3} = -k_pP,\ c_{9,4} = -k_pPe^{-ik_pa},\ c_{9,5} = k_eN,\ c_{9,6} = k_eNe^{-k_ea} \\
&c_{10,7} = e^{-ikb},\ c_{10,8} = -1,\ c_{11,9} = e^{-ik_pb},\ c_{11,10} = 1 \\
&c_{11,11} = e^{-k_eb},\ c_{11,12} = 1,\ c_{12,9} = -k_pPe^{-ik_pb},\ c_{12,10} = -k_pP \\
&c_{12,11} = k_eNe^{-k_eb},\ c_{12,12} = k_eN
\end{aligned}
\tag{2.42}
$$

Note that the characteristic matrix for the other support conditions can be derived by substituting the last six rows of the characteristic matrix for each support condition, as described in Appendix (A3).

$\mathbf{w}$ is a non-trivial solution in Eq.(2.41), which requires the determinant of $\mathbf{C}$ to be zero for the equation to be valid.

$$\det[\mathbf{C}] = 0 \tag{2.43}$$

The modal frequencies can be determined by finding the values that satisfy Eq.

(2.43). As a result, Eq. (2.43) is the frequency equation considering modes I and II crack. Since Eq. (2.43) is a nonlinear equation with respect to ω, the Newton-Raphson (N-R) method is used to effectively iteratively calculate the modal frequencies that satisfy Eq. (2.43).

2.5 Newton-Raphson Method for Solving the Nonlinear Equation

2.5.1 Newton-Raphson Iteration Process

By defining the $\det[\mathbf{C}]$ in Eq. (2.43) as y, it can be linearized with respect to ω as follows:

$$y_{j+1} \approx y_j + \frac{\partial y_j}{\partial \omega}\Delta\omega = 0 \tag{2.44}$$

where y_j and $\frac{\partial y_j}{\partial \omega}$ represent $y|_{\omega=\omega_j}$ and $\left.\frac{\partial y}{\partial \omega}\right|_{\omega=\omega_j}$, respectively, with j denoting the iteration number in the N-R method. $\Delta\omega$ represents a change in angular frequency, which can be determined by rearranging Eq. (2.44).

$$\Delta\omega = -y_j\left(\frac{\partial y_j}{\partial \omega}\right)^{-1} \tag{2.45}$$

The angular frequency is determined by adding the change in the angular frequency obtained from Eq. (2.45) to the previous angular frequency, as follows:

$$\omega_{j+1} = \omega_j + \Delta\omega \tag{2.46}$$

The N-R iteration is performed until the convergence criterion of 10^{-7} is satisfied, using Eqs. (2.44) to (2.46).

$$\left|\frac{\omega_{j+1}-\omega_j}{\omega_{j+1}}\right| < \varepsilon = 10^{-7} \tag{2.47}$$

2.5.2 Derivatives Used in the Newton-Raphson Method

The derivative $\frac{\partial y}{\partial \omega}$ used in Eq. (2.44) can be expressed by applying the chain rule.

$$\frac{\partial y}{\partial \omega} = \frac{\partial y}{\partial k}\frac{dk}{d\omega} + \frac{\partial y}{\partial k_p}\frac{\partial k_p}{\partial \omega} + \frac{\partial y}{\partial k_e}\frac{\partial k_e}{\partial \omega} + \frac{\partial y}{\partial P}\frac{\partial P}{\partial \omega} + \frac{\partial y}{\partial N}\frac{\partial N}{\partial \omega} \tag{2.48}$$

where k is the wavenumber derived from the axial spectral solution, independent of k_p, k_e, P and N. However, k_p, k_e, P, and N are interrelated factors derived together from the bending spectral solution. Note that when all factors are applied to the chain rule, each factor must be considered as an independent entity in the calculation.

The derivative $\frac{dk}{d\omega}$ in Eq. (2.48) can be determined by differentiating Eq. (2.21) with respect to ω.

$$\frac{\partial k}{\partial \omega} = \sqrt{\frac{\rho}{E}} \tag{2.49}$$

To derive the derivative $\frac{\partial k_p}{\partial \omega}$ in Eq. (2.48), the following steps are undertaken:

Firstly, by squaring k_p in Eq. (2.25a), one of the square roots is removed.

$$2k_p^2 - X = \sqrt{X^2 - 4Y} \tag{2.50}$$

Secondly, squaring Eq. (2.50) allows for rearrangement in terms of k_p.

$$k_p^4 - k_p^2 X = -Y \tag{2.51}$$

Finally, differentiating Eq. (2.51) with respect to ω yields $\frac{\partial k_p}{\partial \omega}$.

$$\frac{\partial k_p}{\partial \omega} = \frac{1}{2Xk_p - 4k_p^3}\left(\frac{dY}{d\omega} - k_p^2\frac{dX}{d\omega}\right) \tag{2.52}$$

The derivatives $\frac{dX}{d\omega}$ and $\frac{dY}{d\omega}$ in Eq. (2.52) were calculated by differentiating Eqs. (2.26a) and (2.26b) with respect to ω.

$$\frac{dX}{d\omega} = 2\omega\left(\frac{1}{c_0^2} + \frac{1}{c_q^2}\right) \tag{2.53a}$$

$$\frac{dY}{d\omega} = \frac{4\omega^3}{c_0^2 c_q^2} - \frac{2\omega}{c_0^2 r^2} \tag{2.53b}$$

The derivative $\frac{\partial k_e}{\partial \omega}$ in Eq. (2.48) can be obtained by applying the same procedure used for determining $\frac{\partial k_p}{\partial \omega}$ to Eq. (2.25b), following the steps outlined in Eq. (2.50) through Eq. (2.52).

$$\frac{\partial k_e}{\partial \omega} = -\frac{1}{2Xk_e + 4k_e^3}\left(\frac{dY}{d\omega} + k_e^2\frac{dX}{d\omega}\right) \tag{2.54}$$

The derivatives $\frac{\partial P}{\partial \omega}$ and $\frac{\partial N}{\partial \omega}$ in Eq. (2.48) are calculated by differentiating Eqs. (2.28a) and (2.28b) with respect to ω:

$$\frac{\partial P}{\partial \omega} = \frac{\partial k_p}{\partial \omega} - \frac{1}{k_p^2 c_q^2}\left(2\omega k_p - \frac{\partial k_p}{\partial \omega}\omega^2\right) \tag{2.55a}$$

$$\frac{\partial N}{\partial \omega} = \frac{\partial k_e}{\partial \omega} + \frac{1}{k_e^2 c_q^2}\left(2\omega k_e - \frac{\partial k_e}{\partial \omega}\omega^2\right) \tag{2.55b}$$

The derivatives of y in Eq. (2.48) with respect to k, k_p, k_e, P, and N can be calculated using Jacobi's formula, respectively [Mag19].

$$\frac{\partial y}{\partial k} = \mathrm{tr}[\mathrm{adj}[\mathbf{C}]\frac{\partial \mathbf{C}}{\partial k}] \tag{2.56a}$$

$$\frac{\partial y}{\partial k_p} = \text{tr}[\text{adj}[\mathbf{C}]\frac{\partial \mathbf{C}}{\partial k_p}] \quad (2.56b)$$

$$\frac{\partial y}{\partial k_e} = \text{tr}[\text{adj}[\mathbf{C}]\frac{\partial \mathbf{C}}{\partial k_e}] \quad (2.56c)$$

$$\frac{\partial y}{\partial P} = \text{tr}[\text{adj}[\mathbf{C}]\frac{\partial \mathbf{C}}{\partial P}] \quad (2.56d)$$

$$\frac{\partial y}{\partial N} = \text{tr}[\text{adj}[\mathbf{C}]\frac{\partial \mathbf{C}}{\partial N}] \quad (2.56e)$$

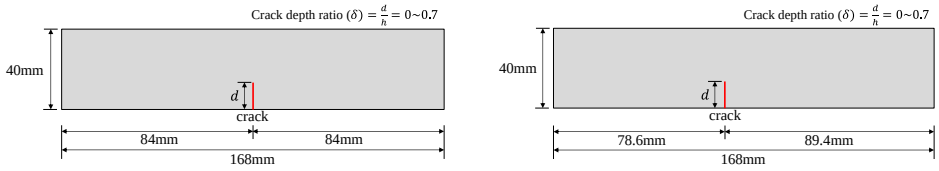
where tr[ ] and adj[ ] denote the trace and the adjugate of the matrix, respectively. The matrix representations of the derivatives $\frac{\partial \mathbf{C}}{\partial k}$, $\frac{\partial \mathbf{C}}{\partial k_p}$, $\frac{\partial \mathbf{C}}{\partial k_e}$, $\frac{\partial \mathbf{C}}{\partial P}$, and $\frac{\partial \mathbf{C}}{\partial N}$ are elaborated in Appendix (A4).

2.6 Validation

2.6.1 Numerical Example

The proposed method is validated through comparing it with finite element analysis and experimental results. Fig. 2.3 shows the geometry of the cracked beam adhering to the standard specification for the single-edge bend specimen in ASTM E1820 [Ast15]. The length, height, and width of the beam are 168 mm, 40 mm, and 10 mm, respectively. The beam is free at both ends, which is easier to implement in experiments than the simply supported or fixed-free support conditions. The beam is made of aluminum with an elastic modulus, Poisson's ratio, and density of 69 GPa, 0.34, and 2700 kg/m^3, respectively. The crack is positioned at the center of the beam and 0.45 *L* from the left side of the beam, as shown in Fig. 2.3(a) and (b), respectively. The crack depth ratio varies in increments of 0.1, ranging from 0 to 0.7. When the

crack is located at the center of a free-free intact beam, its location always aligns with the antinodes of the odd-numbered axial and bending vibration modes, or with the nodes of the even-numbered axial and bending vibration modes. Consequently, the modal behavior of a free-free beam with a center crack is contingent on both the number and type of vibration modes. Table 2.2 presents the contributions of modes I and II crack to the four types of vibration modes, based on the compatibility conditions in Eq. (1.2). At the center of the beam in the odd-numbered axial and bending modes, where $w_L' - \theta_L = 0$, only the mode I crack causing ABMC affects both vibration modes, whereas the mode II crack does not. Conversely, in even-numbered axial and bending modes, where $u_L' = \theta_L' = 0$ at the center of the beam, only the mode II crack causing the sliding crack mode affects both even-numbered bending vibration modes, while the mode I crack does not. Notably, the mode II crack does not affect the even-numbered axial modes when there is no ABMC due to the mode I crack. Considering this, an examination of the modal behaviors of the cracked beam in Fig. 2.3(a) will distinctly reveal the individual contributions of modes I and II crack to the local vibration at the crack.



(a) located at the center of the beam

(b) located $0.45L$ away from the left end of the beam

Fig. 2.3 Numerical example for free-free beams with a transverse crack.

Compared to Fig. 2.3(a), the crack position in Fig. 2.3(b) is deliberately arranged to avoid overlapping with either the antinodes or nodes of the first five bending

modes, which are observed below the cut-off frequency of an intact beam.

Table 2.2 Contribution of modes I and II crack to the four kinds of vibration modes of a free-free deep beam with a center crack based on the compatibility conditions

Vibration mode	Mode I crack				Mode II crack
	$F_{aa}u_L'$	$F_{bb}\theta_L'$	$F_{ab}\theta_L'$	$F_{ba}u_L'$	$F_{ss}(w_L'-\theta_L)$
Odd-numbered axial mode	O	O	O	O	X
Odd-numbered bending mode	O	O	O	O	X
Even-numbered axial mode	X	X	X	X	X*
Even-numbered bending mode	X	X	X	X	O

Note: At the center of a free-free beam, $u_L' = \theta_L' = 0$ in even-numbered axial and bending vibration modes while $w_L' - \theta_L = 0$ in odd-numbered axial and bending vibration modes.

*Although $F_{ss}(w_L' - \theta_L) \neq 0$, Eq. (1.2c) does not affect the even-numbered axial vibration modes in the absence of axial-bending modal coupling owing to mode I crack.

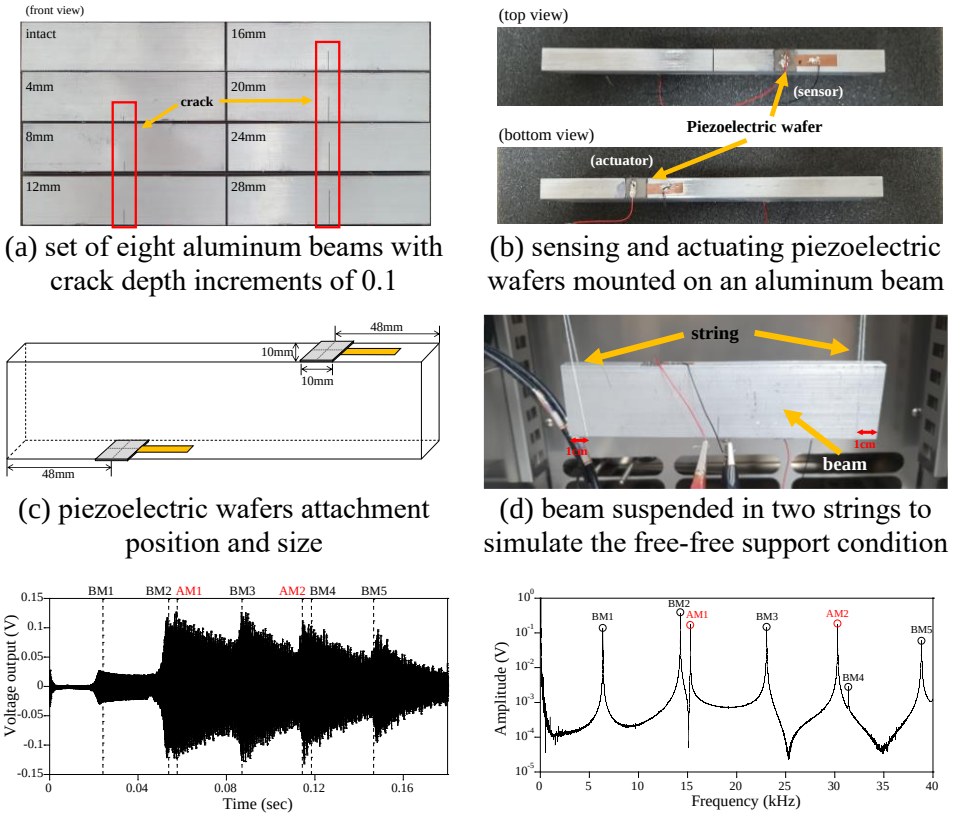
Investigating the modal behaviors of the cracked beam in Fig. 2.3(b) will demonstrate the fully combined effects of modes I and II crack on the local vibration at the crack when the crack aligns with neither the axial and bending antinodes nor the axial and bending nodes of the intact beam.

2.6.2 Experimental Setup

Aluminum beams with crack depth ratios ranging from 0.1 to 0.7 were used in the experiment, as shown in Fig. 2.4(a). Ensuring the reliability of the modal frequency

of an intact beam is crucial for determining the fractional reduction in the modal frequency caused by a crack. Therefore, the mean value of the modal frequencies measured from the four intact beams is used. The crack located at the bottom of the beam was manufactured in the form of a 0.3 mm wide notch aligned with a specific crack depth, as shown in Fig. 2.4(a). The crack depth was incrementally increased by 4 mm up to a maximum depth of 28 mm. As shown in Fig. 2.4(b), piezoelectric wafers (Piezo Systems Inc. PSI-5A4E L10 mm × T0.191 mm × W10 mm) was attached to the top and bottom of each beam to collect the dynamic response of the beam using the pitch-catch method [Psi19]. A sensing piezoelectric wafer were attached at the top of the beam, and an actuating piezoelectric wafer was attached at the bottom. The piezoelectric wafers were attached 48 mm away from each end of the beam, as shown in Fig. 2.4(c). Strategically positioned to minimize overlap with the bending nodes and antinodes of the beam, this arrangement ensures their ability to efficiently drive signals in all axial and bending modes below the cut-off frequency of the beam. To simulate free boundary condition, two strings were suspended 1 cm away from each end of the beam s (Fig. 2.4(d)) [Kas08]. A chirp voltage input signal with a driving frequency range of 1 to 130 kHz was applied to the actuating piezoelectric wafer using a 16-bit arbitrary waveform generator (NI PXI-5422). The duration and amplitude of the chirp-voltage input signal were 1 s and 6 V, respectively. The output voltage signal was obtained from the sensing piezoelectric wafer using a 14-bit high-speed digitizer (NI PXIe-5122). The sampling rate and frequency resolution were 5 MHz and 1 Hz, respectively. The

measurement time for determining the frequency resolution was set to 1 s to provide a sufficient duration for the dynamic response of the beam to decay. The measurement data was obtained by conducting 10 measurements of the output voltage signal using the LabVIEW^{TM} software and then calculating the average of the results. All experiments were conducted using a temperature chamber where 25°C was maintained to minimize unexpected variations in the measured modal frequency due to external temperature changes. Fig. 2.4(e) shows the average output



(a) set of eight aluminum beams with crack depth increments of 0.1

(b) sensing and actuating piezoelectric wafers mounted on an aluminum beam

(c) piezoelectric wafers attachment position and size

(d) beam suspended in two strings to simulate the free-free support condition

(e) example of intact beam average output voltage signal

(f) frequency response spectrum of (e) and modal frequencies

Fig. 2.4 Experimental setup.

voltage signal obtained by conducting 10 consecutive measurements on an intact

beam. The dotted lines indicate the moment when the modal frequencies of the axial and bending modes in the intact beam match the driving frequency of the input chirp-voltage signal. Letters “AM” and “BM” represent the axial and bending modes, respectively (e.g., BM5 denotes the fifth bending mode). The output voltage signal in Fig. 2.4(e) can be represented as a frequency-response spectrum using Fast Fourier Transform (FFT), as shown in Fig. 2.4(f). The corresponding modes for each peak frequency in Fig. 2.4(f) were identified by comparison with the finite element analysis results.

2.6.3 Finite Element Analysis Setup

Finite element analysis was conducted using ABAQUS 2022/Foundation. A mesh layout (672,000 8-node solid element L100 μm × T100 μm) was used for element discretization to accurately calculate the changes in modal frequencies. Double nodes were introduced along the crack surfaces to simulate the mechanical behavior of a transverse open crack. The finite element analysis was conducted by incrementally increasing the crack depth ratio from the intact beam to the beams with a crack depth ratio of 0.7 with an increment of 0.1.

2.6.4 Case 1: Free-Free Beam with a Center Crack

Table 2.3 lists the mean values of the experimental modal frequencies of the four intact beams. There were two axial modes and five bending modes under the cut-off frequency. Table 2.3(b) presents the fractional reduction in the modal frequency of

the cracked beam compared to that of the intact beam.

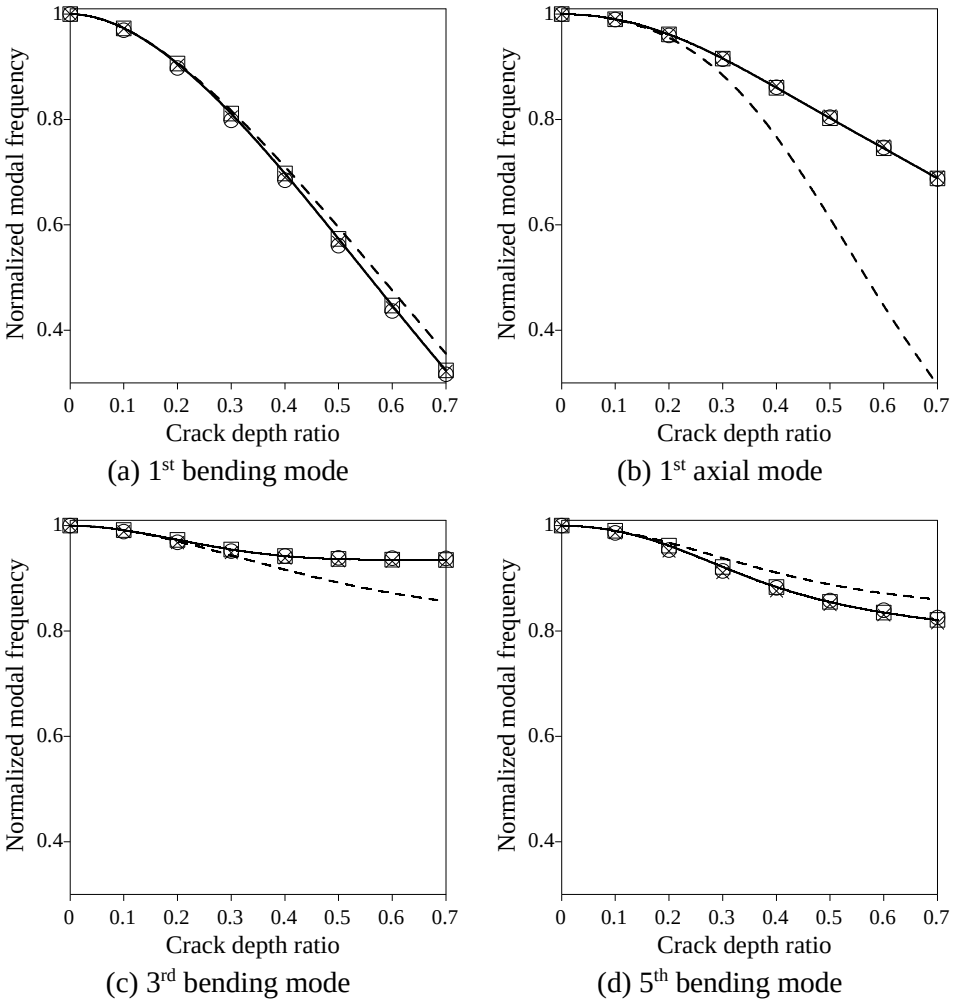
Table 2.3 Experimental results for the cracked beam in Fig. 2.3 (a): (a) The values of experimental modal frequencies of four intact beams (unit: kHz); (b) Fractional reduction in the modal frequency of cracked beams compared to that of the intact beam (unit: %)

Crack depth ratio / Mode No.	Intact[a]	0.1[b]	0.2[b]	0.3[b]	0.4[b]	0.5[b]	0.6[b]	0.7[b]
BM1	6.381	3.044	10.237	20.17	31.53	43.93	56.33	68.36
BM2	14.28	-0.06478	0.1243	0.6706	1.784	3.843	6.99	11.61
AM1	15.29	1.005	4.020	8.532	13.87	19.58	25.30	31.28
BM3	23.07	1.106	3.144	4.838	5.775	6.113	6.178	6.208
AM2	30.29	-0.09408	-0.02806	-0.1106	-0.1172	-0.1997	-0.2063	-0.2096
BM4	31.40	-0.05334	0.06767	0.6313	1.826	4.529	9.319	15.43
BM5	38.87	1.3454	4.636	8.566	11.79	14.22	16.04	17.45

Fig. 2.5 shows a comparison of the normalized modal frequency (NMF) with the crack depth ratio for the odd-numbered modes, which are obtained from the proposed method (Eq. (2.43)), conventional method, method considering ABMC, finite element analysis, and experiment. Here, the NMF is defined as the ratio of the modal frequency of the cracked beam to that of the intact beam. Because only mode I crack caused by pure bending vibration is considered in the conventional method, as listed in Fig. 1.6, the corresponding frequency equation for the bending modes can be easily derived by substituting $F_{aa} = F_{ab} = F_{ba} = F_{ss} = 0$ into the characteristic matrix in Eq. (2.43). Similarly, the conventional frequency equation for the axial modes can be obtained by substituting $F_{bb} = F_{ab} = F_{ba} = F_{ss} = 0$ into the characteristic matrix in Eq. (2.43), such that the mode I crack caused by the pure

axial bending vibration can be considered. The modal frequencies can be calculated using the N-R method, as described in Section 2.5. The black solid and dotted lines represent the NMF of the axial and bending modes calculated by the proposed and conventional methods, respectively, and the symbols "x" and "o" denote the NMF obtained from the finite element analysis and the experiment, respectively. Note that the normalized modal frequency shifts (NMFS) obtained from Eq. (2.43) considering only the mode I crack (i.e., $F_{ss} = 0$) is depicted as "□" in Fig. 2.5. Overall, the results of the proposed method agree well with those of the finite element analysis and experiment. Both the conventional and proposed methods demonstrate a consistent trend in modal frequency reduction for crack depths less than 0.2. However, the differences in the reduction trends between the two methods become more pronounced as the crack depth ratio exceeds 0.2. The discrepancy between the proposed and conventional methods occurs due to the ABMC caused by mode I crack, which is not accounted for in the conventional method. A comparison between the NMF of the first axial mode in Fig. 2.5(b) and that of the third bending mode in Fig. 2.5(c) reveals that the axial mode displays a more substantial deviation from the conventional method than the adjacent bending mode. Thus, the axial mode within the frequency range of interest is considerably affected by the ABMC, underscoring the importance of accounting for its impact, just as with the bending mode. Note that the first axial mode is situated between the first and third bending modes, leading to the influence of the ABMC on both bending modes. Because the significance of ABMC increases with increasing mode number, its effect is more pronounced in the

third bending mode than in the first.



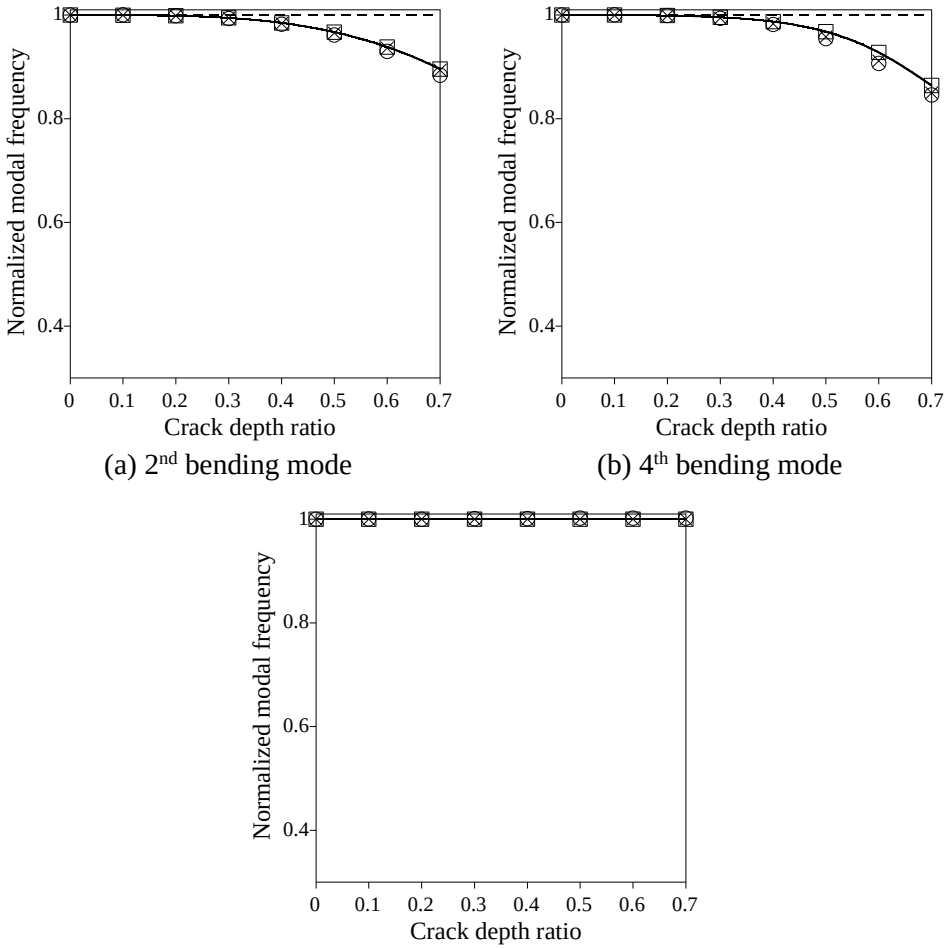
(a) 1st bending mode (b) 1st axial mode

(c) 3rd bending mode (d) 5th bending mode

Fig. 2.5 Comparison of NMF of odd-numbered modes with respect to crack depth ratio (▬: proposed method [Eq. (2.43)], ▬ ▬: conventional method, □: Eq. (2.43) with $F_{ss} = 0$, x: finite element analysis, o: experiment).

Similar to Fig. 2.5, Fig. 2.6 shows the NMF with the crack depth ratio for the even-numbered modes. The symbols used in Fig. 2.6 are identical to those used in Fig. 2.5. The NMFS obtained using Eq. (2.43) considering only the mode II crack (i.e., $F_{aa} = F_{bb} = F_{ab} = F_{ba} = 0$) is depicted as "□" in Fig. 2.6. In the conventional method,

only the mode I crack caused by bending vibration is considered, as described in Fig. 1.6. Therefore, when a crack is located at a bending node of the beam (i.e., $\theta_L' = 0$), the modal frequency for all crack depth ratios remains identical to that of an intact



(a) 2nd bending mode

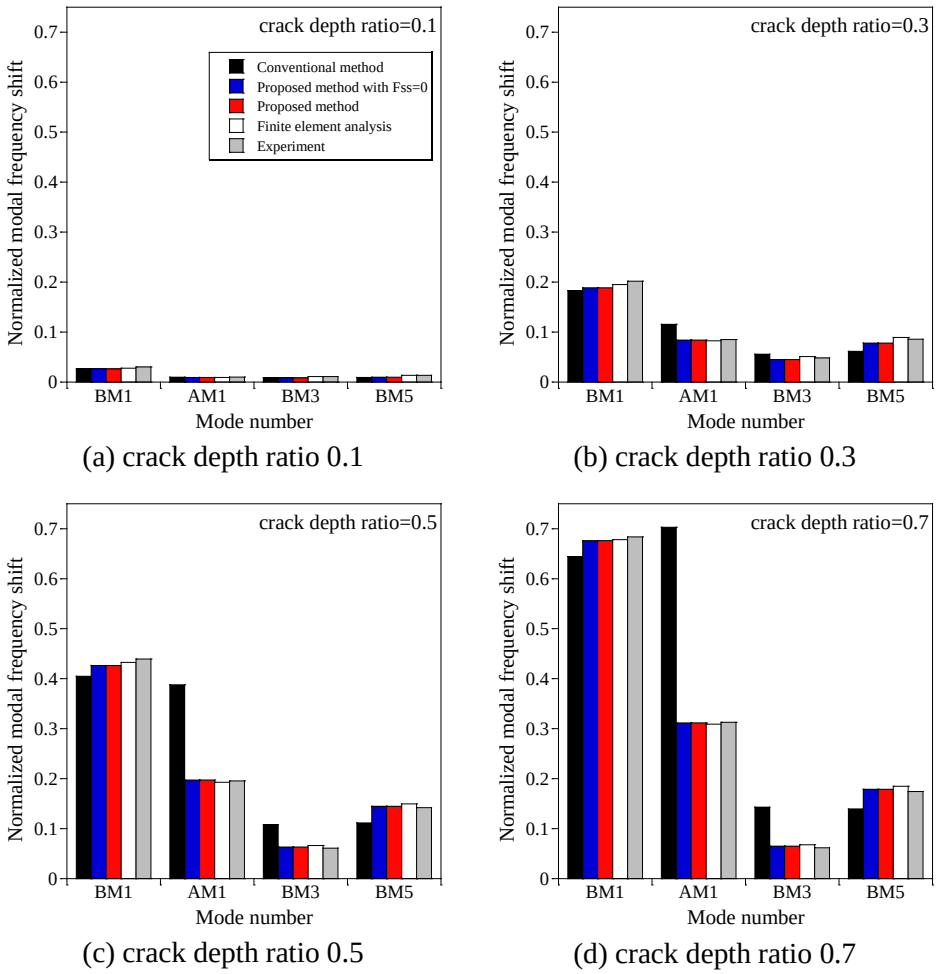
(b) 4th bending mode

(c) 2nd axial mode

Fig. 2.6 Comparison of NMF of even-numbered modes with respect to crack depth ratio (——: proposed method [Eq. (2.43)], – –: conventional method, □: Eq. (2.43) with $F_{aa} = F_{bb} = F_{ab} = F_{ba} = 0$, x: finite element analysis, o: experiment).

beam owing to $F_{bb}\theta_L' = 0$, as described in Table 2.2. In contrast to the conventional method, the fractional reduction of the modal frequencies due to the mode II crack

is observed in Figs. 2.6(a) and (b). The NMF for the fourth bending mode in Fig. 2.6(b) decreases faster with the crack depth ratio than that for the second bending mode in Fig. 2.6(a). This implies that the effect of the mode II crack intensifies as the mode number increases. No NMF changes occur in the second axial mode because neither mode I nor mode II crack affected the even-numbered axial modes, as presented in Table 2.2



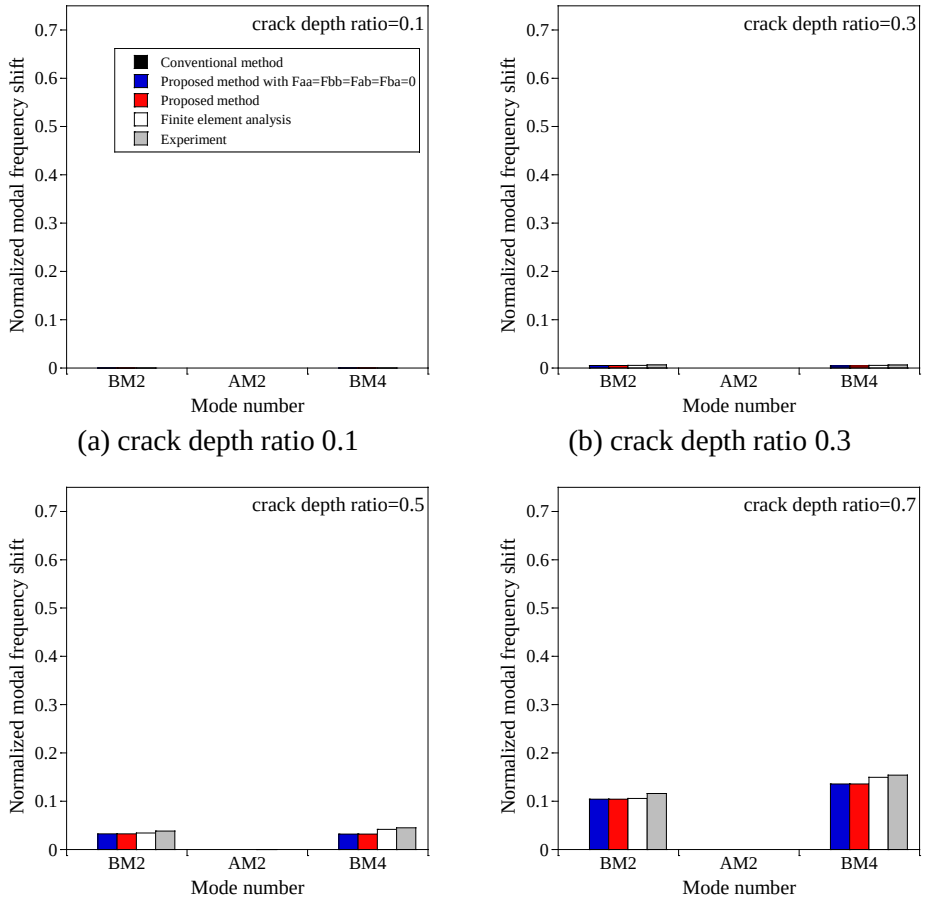
(a) crack depth ratio 0.1 (b) crack depth ratio 0.3

(c) crack depth ratio 0.5 (d) crack depth ratio 0.7

Fig. 2.7 Comparison of NMFS with odd-numbered modes for varying crack depth ratios.

Fig. 2.7 shows the normalized modal frequencies shifts for odd-numbered axial and bending modes, with crack depth ratios ranging from 0.1 to 0.7 in increments of 0.2 up to 0.7. Note that NMFS represents the fractional reduction in modal frequencies caused by a crack and is calculated as 1 minus NMF. Fig. 2.7 shows the NMFS amount as a bar graph. Black, blue, red, white, and gray represent the conventional method, cracked beam with ABMC, proposed method, finite element analysis, and experiment, respectively. The mode numbers along the horizontal axis are sorted according to the modal frequencies of the intact beam. When the crack depth ratio is 0.1, the influence of the ABMC is negligible; thus, the proposed method yields practically identical results to the conventional method (Fig. 2.7 (a)). The effect of ABMC begins to appear when the crack depth ratio reaches 0.3 (Fig. 2.7 (b)). As the crack depth ratio increases, the influence of the ABMC becomes more pronounced, as shown in Fig. 2.7. The NMFS obtained using the proposed method perfectly aligns with the values obtained from Eq. (2.43) considering only the mode I crack in Fig. 2.7. This alignment reveals the exclusive impact of the mode I crack on the NMFS when the crack is centered on the odd-numbered axial and bending vibration modes, as listed in Table 2.2.

Fig. 2.8 shows the NMFS for even-numbered bending and axial modes, with crack depth ratios ranging from 0.1–0.7 in increments of 0.2. The bars used in Fig. 2.8 are identical to those used in Fig. 2.7. While ABMC in the odd-numbered bending modes begins to appear from a crack depth ratio of 0.3 in Fig. 2.7, the effect of the mode II crack on the even-numbered bending modes is barely noticeable up to the



(a) crack depth ratio 0.1 (b) crack depth ratio 0.3

(c) crack depth ratio 0.5 (d) crack depth ratio 0.7

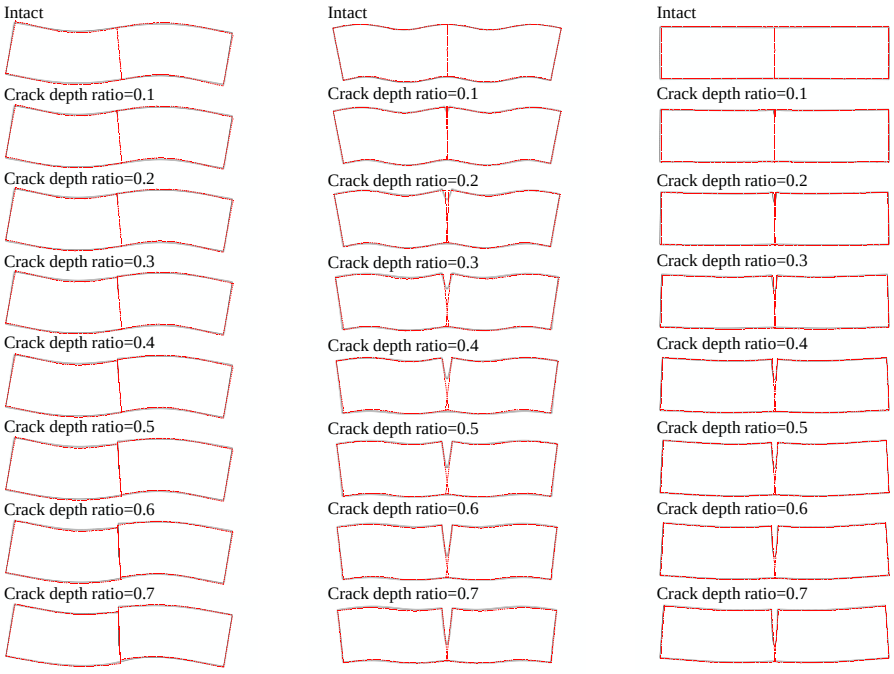
Fig. 2.8 Comparison of NMFS with even-numbered modes for varying crack depth ratios.

same crack depth ratio in Fig. 2.8 (b). Note that as the crack depth ratio and mode number increase, the effect of the mode II crack on the NMFS of the bending modes becomes more sensitive (Fig. 2.8 (d)). In contrast, the NMFS of the second axial mode is zero for all crack depth ratios. This implies that the NMFS is not affected at all by the mode II crack when the crack is aligned with the center of the even-numbered axial and bending modes, as described in Table 2.2. Fig. 2.8 demonstrates that the NMFS values obtained from the proposed method perfectly agree with those

from Eq. (2.43) considering only the mode II crack. This agreement reveals the exclusive impact of the mode II crack on the NMFS when the crack is centered on the even-numbered axial and bending vibration modes, as detailed in Table 2.2.

Fig. 2.9 shows a comparison of the evolution of mode shapes with the crack depth ratio for the second and fifth bending modes and the first axial mode between the proposed method and finite element analysis. The black solid and red dashed lines denote the mode shapes obtained from the finite element analysis and the proposed method, respectively. The neutral axis of the mode-shape vector was computed using the modal frequencies and spectral solutions for both sides of the crack. The feature edges of the mode shape vector are determined based on the Timoshenko beam and elementary rod theories. The mode shape vector is multiplied by an appropriate scaling factor to visually highlight the ABMC caused by the mode I crack and the sliding (or shear) mode caused by the mode II crack. The scaling factor for each mode was determined based on the correspondence between the mode shape of the proposed method and the finite element analysis of an intact beam. The proposed method accurately predicted the evolution of mode shapes in comparison with the results of finite element analysis. The evolution of modes I and II crack near the center crack of a free-free beam is mutually exclusive depending on the type of vibration mode, as indicated in Table 2.2. For example, in Fig. 2.9(a), the evolution of the sliding mode is clearly observed near the crack, without any sign of ABMC development in the second bending mode. This is due to the exclusive effect of the mode II crack on the even-numbered bending modes. Conversely, in Figs. 2.9(b) and

(c), the evolution of the ABMC due to the mode I crack is clear near the crack without any appearance of the sliding mode in the fifth bending and first axial modes, respectively. This is because the mode I crack solely affects the odd-numbered axial



(a) 2nd bending mode (b) 5th bending mode (c) 1st axial mode

Fig. 2.9 Mutually exclusive evolution of modes I and II crack in the vicinity of a center crack in a free-free in Fig. 2.3(a) (..... : proposed method [Eq. (2.43)], ——: finite element analysis).

and bending modes. These mode shape evolutions in Fig. 2.9 show the mutually exclusive contributions of modes I and II crack to each vibration mode, as described in Table 2.2. Note that the left and right shapes overlap in the modal shapes below the neutral axis of the crack location. This phenomenon occurs because the neutral axes, which are split on either side of the crack, are calculated separately and feature edges are drawn.

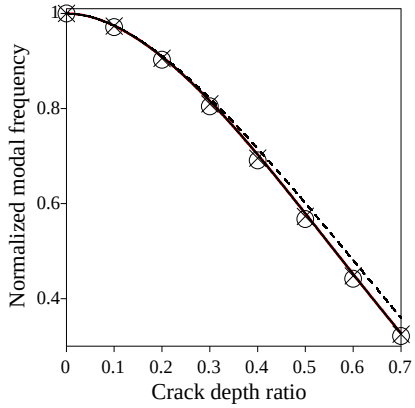
2.6.5 Case 2: Free-Free Beam with a Crack at 0.45L Away from the Left End of the Beam

Table 2.4(a) lists the mean values of the experimental modal frequencies of the four intact beams. Similar to Table 2.3(a), there are two axial modes and five bending modes under the cut-off frequency. Table 2.4(b) presents the fractional reduction in the modal frequency of the cracked beam compared to that of the intact beam.

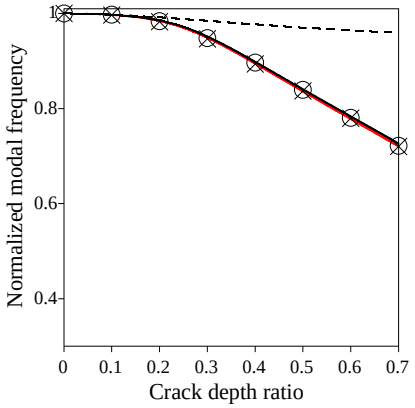
Table 2.4 Experimental results for a cracked beam in Fig. 2.3(b): (a) The values of experimental modal frequencies of four intact beams (unit: kHz); (b) The mean values of the fractional reduction in the modal frequency of cracked beams compared to that of the intact beam (unit: %)

Crack depth ratio / Mode No.	Intact[a]	0.1[b]	0.2[b]	0.3[b]	0.4[b]	0.5[b]	0.6[b]	0.7[b]
BM1	6.381	2.840	9.720	19.51	30.89	43.22	55.79	67.86
BM2	14.28	0.2364	1.602	5.167	10.33	16.07	21.93	27.82
AM1	15.29	0.8485	2.993	4.995	6.440	8.51	11.50	15.74
BM3	23.07	0.7033	2.194	3.607	4.726	5.775	6.893	8.505
AM2	30.29	-0.02806	0.3119	1.315	2.642	4.349	6.534	9.690
BM4	31.40	0.3129	1.039	1.638	2.099	2.861	4.421	6.395
BM5	38.87	1.3454	4.636	8.566	11.79	14.22	16.04	17.45

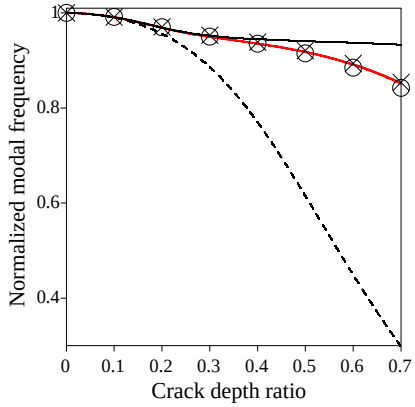
Fig. 2.10 shows the comparison results of the NMF for the crack depth among the proposed method, conventional method, finite element analysis, and experiment. The symbols of the conventional method, "x" and "o" are identical to those in Fig. 2.5. The red and black solid lines represent the NMF of the axial and bending modes calculated by the proposed method and by Eq. (2.43) considering only the mode I



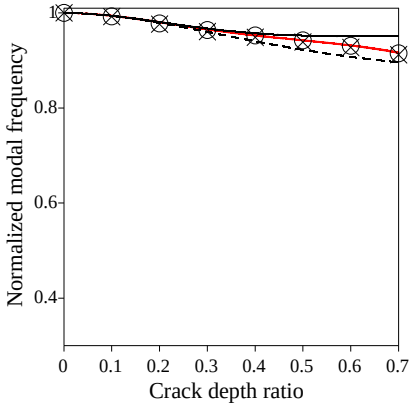
(a) 1st bending mode



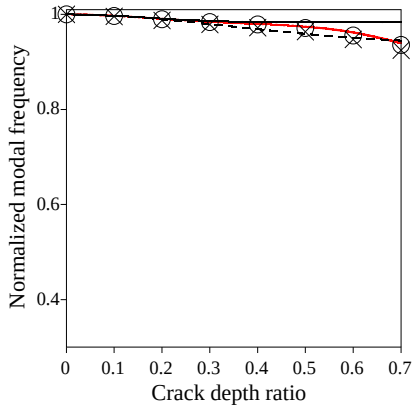
(b) 2nd bending mode



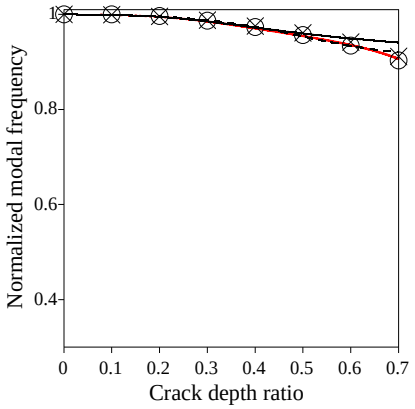
(c) 1st axial mode



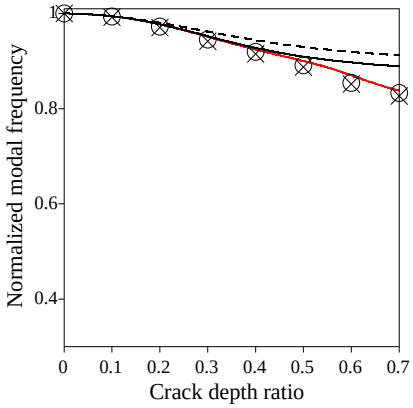
(d) 3rd bending mode



(e) 4th bending mode



(f) 2nd axial mode

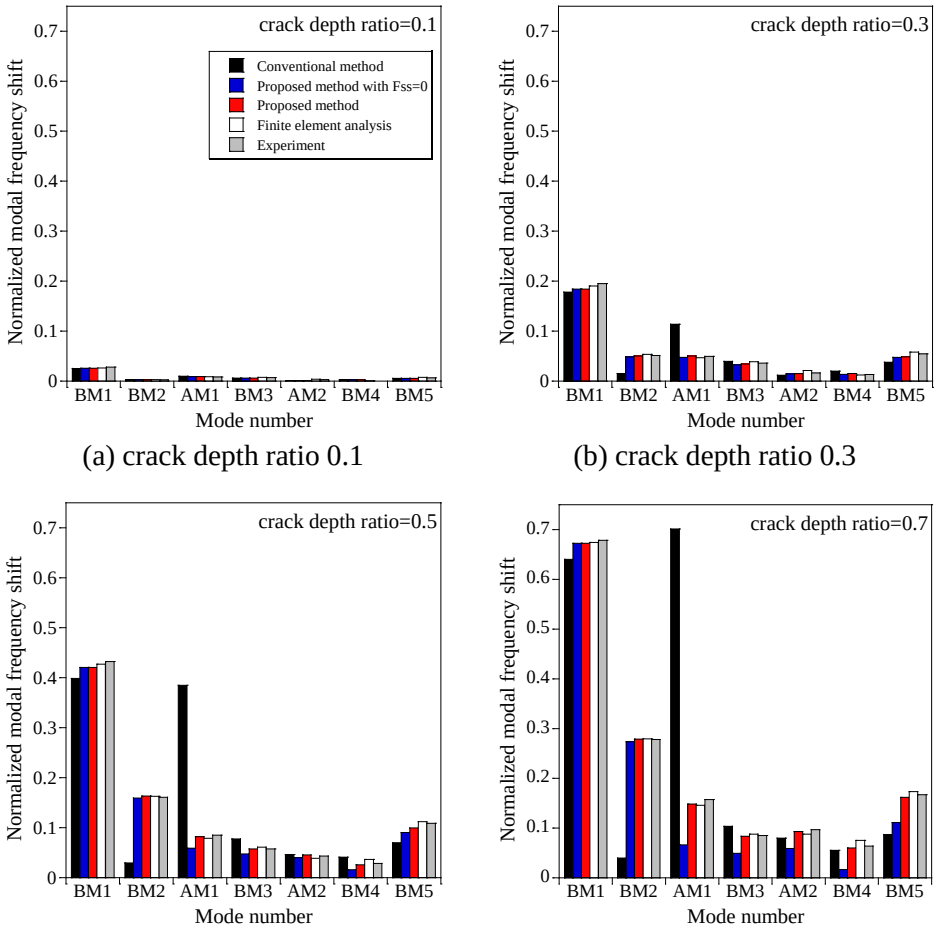


(g) 5th bending mode

Fig. 2.10 Comparison of NMF with respect to crack depth ratio (——: proposed method [Eq. (2.43)], – –: conventional method, —— : Eq. (2.43) with $F_{ss} = 0$, x: finite element analysis, o: experiment).

crack. Notably, the discrepancy between the red and black solid lines represents the contribution of the mode II crack, whereas that between the black dotted and solid lines represents the contribution of the ABMC by the mode I crack. Investigating these discrepancies can provide physical insights into how modes I and II crack affect the modal behaviors of a cracked beam. Compared with the finite element method and experiment, the proposed method produces satisfactory results, outperforming the conventional method. In the first bending mode in Fig. 2.10(a), there exists a slight ABMC caused by the mode I crack, whereas the sliding mode caused by the mode II crack is rarely observed. A significant ABMC occurs with a small sliding mode in the second bending mode, as shown in Fig. 2.10(b). However, the results accounting for only ABMC deviate from those predicted by the proposed method due to the significant contribution of mode II crack in the higher axial and bending modes when the crack depth ratio exceeds 0.3 (Figs. 2.10(c)-(g)). Unlike in

Fig. 2.6(c), the combined effects of modes I and II crack are clearly demonstrated for the second axial mode in Fig. 2.10(e) when the crack does not align with either the antinode or node of the second axial mode. The contribution of the mode II crack becomes evident as the mode number and crack depth ratio increase.



(a) crack depth ratio 0.1 (b) crack depth ratio 0.3

(c) crack depth ratio 0.5 (d) crack depth ratio 0.7

Fig. 2.11 NMFS with respect to mode number for varying crack depth ratios.

Fig. 2.11 shows the NMFS for axial and bending modes in relation to crack depth ratios from 0.1 to 0.7 in increments of 0.2. The bars used in Fig. 2.11 are identical to those used in Fig. 2.7. When the crack depth ratio is 0.1, both the ABMC by mode I

crack and the sliding mode by mode II crack are rarely observed, as shown in Fig. 2.11(a). The influence of the ABMC begins to appear when the crack depth ratio exceeds 0.3 (Fig. 2.11(b)). As the crack depth ratio increases, the ABMC becomes more pronounced particularly in the first axial mode.



Fig. 2.12 Combined evolution of modes I and II crack in the vicinity of a crack in a free-free beam in Fig. 2.3(b) (..... : proposed method [Eq. (2.43)], ——: finite element analysis).

Fig. 2.12 shows a comparison of the evolution of mode shapes with the crack depth ratio for the fifth bending and second axial modes, respectively, between the

proposed method and finite element analysis. All mode shapes are produced using the same procedures shown in Fig. 2.9. Compared with the finite element analysis results, the proposed method precisely captures the sliding mode due to the mode II crack, as well as the ABMC due to the mode I crack as the crack depth ratio increases. For the fifth bending mode in Fig. 2.12(a), the crack opening gradually appears due to the ABMC when the crack depth ratio exceeds 0.3. The sliding mode at the crack becomes pronounced due to the mode II crack from a crack depth ratio > 0.5. When the crack depth ratio is 0.2, the second axial mode begins to subtly reveal the crack opening due to the ABMC, while the sliding mode appears from the crack depth ratio > 0.4, as shown in Fig. 2.12(b). At a crack depth ratio of 0.7, the combined evolution of modes I and II crack is apparent for both the fifth bending and second axial modes, indicating the ABSMC of a free-free cracked beam. The proposed method accurately predicts the combined evolution of modes I and II crack in cracked beams.

2.6.6 Case 3: Cantilever Beam with a Crack at Varying Locations

The validity of the proposed method is demonstrated through a comparison with the finite element analysis of a cantilever beam with a transverse crack at various locations, as shown in Fig. 2.13. The geometry and material properties of the cracked beam are identical to those of the beam shown in Fig. 2.3. Owing to space limitations, only the NMFS values calculated by the proposed method are compared with those obtained from the finite element analysis for various crack depth ratios and crack locations; the results are shown in Fig. 2.14. All symbols are identical to those used

in Fig. 2.11. The discrepancy between the red and black solid lines represents the contribution of the mode II crack, whereas that between the black dotted and solid lines represents the contribution of the ABMC by the mode I crack.

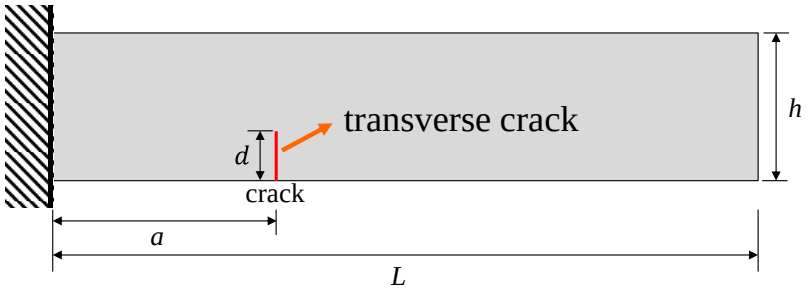
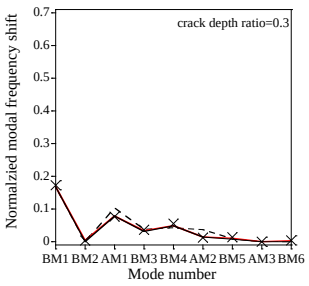


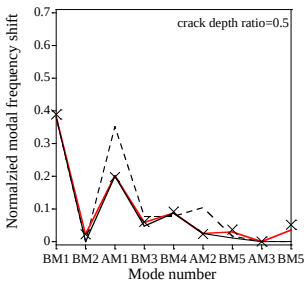
Fig. 2.13 Cantilever beam with a transverse crack at varying locations (L = 168 mm, h = 40 mm).

Crack depth ratios of 0.3, 0.5, and 0.7 denoting incipient, intermediate, and deep cracks, respectively, are considered with relative crack locations (a/L) from the left end of the beam of 0.2, 0.4, 0.6, and 0.8. Overall, the NMFS predictions considering ABSMC using Eq. (2.43) are satisfactory compared to those from the finite element analysis, as shown in Fig. 2.14. The effects of ABSMC on the modal frequencies increase significantly for the crack depth ratio, regardless of the relative crack locations. Similar to Fig. 2.11, the ABMC caused by the mode I crack increases significantly with the crack depth ratio, particularly for the axial modes. When the crack depth ratio is 0.3, the sliding mode by mode II crack is rarely observed for all crack locations. However, the contribution of the mode II crack becomes more evident for higher modal frequencies when the crack depth ratio exceeds 0.5. While using a bar graph as shown in Fig. 2.7 might be appropriate, the cantilever beam is verified solely using NMFS. Therefore, to clearly illustrate that the proposed method

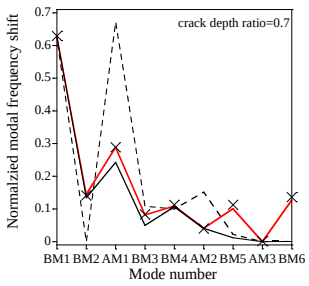
predicts the results of finite element analysis more accurately than the conventional method, the same symbols are used as in Figure 2.5, including solid and dashed lines.



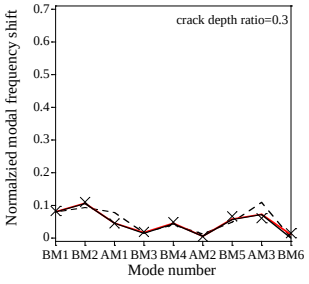
(a) crack depth ratio 0.3 for a/L=0.2



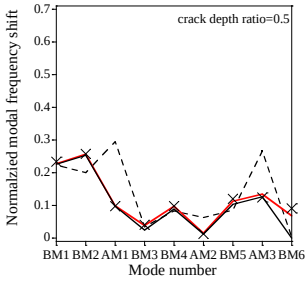
(b) crack depth ratio 0.5 for a/L=0.2



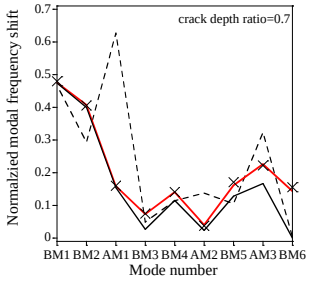
(c) crack depth ratio 0.7 for a/L=0.2



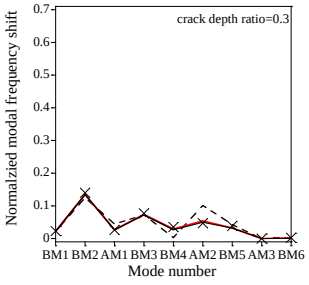
(d) crack depth ratio 0.3 for a/L=0.4



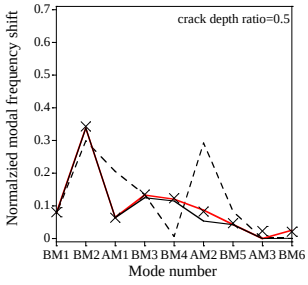
(e) crack depth ratio 0.5 for a/L=0.4



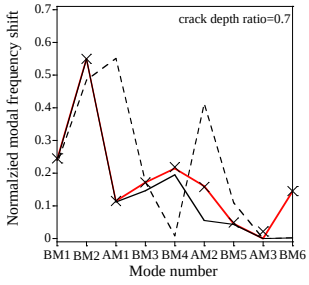
(f) crack depth ratio 0.7 for a/L=0.4



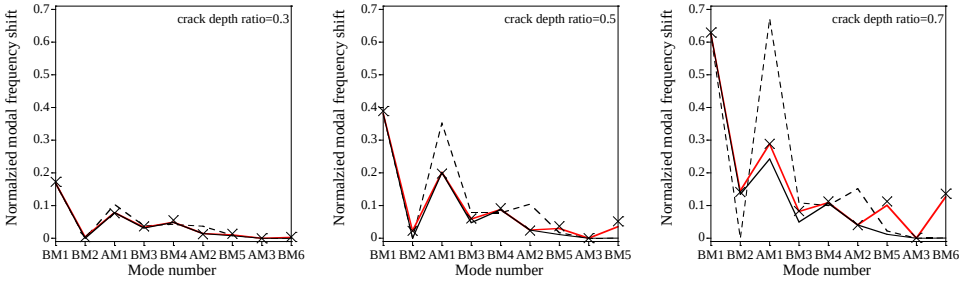
(g) crack depth ratio 0.3 for a/L=0.6



(h) crack depth ratio 0.5 for a/L=0.6



(i) crack depth ratio 0.7 for a/L=0.6



(j) crack depth ratio 0.3 for a/L=0.8

(k) crack depth ratio 0.5 for a/L=0.8

(l) crack depth ratio 0.7 for a/L=0.8

Fig. 2.14 NMFS with respect to mode number for varying crack depth ratios and relative crack locations of the cantilever beam (▬: proposed method [Eq. (2.43)], ▬ ▬: conventional method, ▬ : Eq. (2.43) with $F_{ss} = 0$, x: finite element analysis, o: experiment).

Chapter 3
Beam with a Crack in the Bending Antinodes

In Chapter 2, an analytical model was developed that accurately predicts the behavior of beams with transverse cracks regardless of the crack location. In Section 2.6.4, it was verified that when a crack is located at the bending antinodes, it is only affected by the mode I crack, as demonstrated in conjunction with Table 2.2. A key point here is the influence of ABMC on frequency changes when the axial and bending modes are adjacent. However, due to the characteristic matrix form of the equation presented in Chapter 2, it is impossible to deduce the phenomena of modal coupling between the axial and bending modes by examining the equation alone. Consequently, Chapter 3 aims to conduct an in-depth analysis of specific cases in which the crack is located at the bending antinodes. This is achieved by deriving a closed-form frequency equation that considers only the mode I crack using the analytical model presented in Chapter 2.

3.1 Cracked Beam Modeling

3.1.1 Compatibility Equation of the Crack

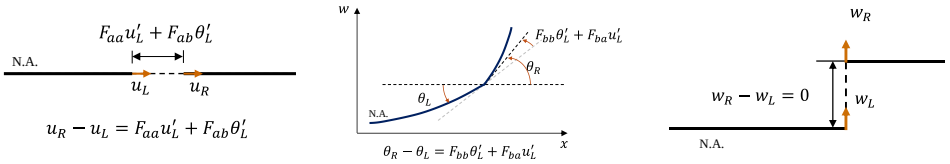
When considering only the effects of ABMC and assuming the lack of influence from the mode II crack, the behavior of the crack can be simulated by setting F_{ss} to zero in the compatibility equation of Eq. (1.2), as validated in Section 2.6.4.

The three compatibility equations should be satisfied, as shown in Fig. 3.1 [Lev72].

$$u_R - u_L = F_{aa}u'_L + F_{ab}\theta'_L \tag{3.1a}$$

$$\theta_R - \theta_L = F_{bb}\theta'_L + F_{ba}u'_L \tag{3.1b}$$

$$w_R - w_L = 0 \tag{3.1c}$$



(a) axial displacement (b) rotational angle (c) transverse displacement

Fig. 3.1 Compatibility equations at the crack in case considering mode I crack.

3.1.2 Spectral Solution

This chapter applies the analytical model from Chapter 2 under the condition that the crack is located at the bending antinodes. As the only variation under these conditions lies in the compatibility equations, the spectral solution employs Eqs. (2.22) and (2.27) equally, as derived in Section 2.2.

The spectral solution for the axial displacements is provided as two parts on both sides of the crack [Doy89].

$$u_L(x_1) = A_1 e^{-ik(a-x_1)} + A_2 e^{-ikx_1} \tag{3.2a}$$

$$u_R(x_2) = B_1 e^{-ikx_2} + B_2 e^{-ik(b-x_2)} \tag{3.2b}$$

The spectral solution for the transverse displacements and the rotational angles are represented on both sides of the crack [Mei05].

$$w_L(x_1) = A_3 e^{-ik_p(a-x_1)} + A_4 e^{-ik_p x_1} + A_5 e^{-k_e(a-x_1)} + A_6 e^{-k_e x_1} \tag{3.3a}$$

$$w_R(x_2) = B_3 e^{-ik_p x_2} + B_4 e^{-ik_p(b-x_2)} + B_5 e^{-k_e x_2} + B_6 e^{-k_e(b-x_2)} \tag{3.3b}$$

$$\theta_L(x_1) = -iPA_3 e^{-ik_p(a-x_1)} + iPA_4 e^{-ik_p x_1} - NA_5 e^{-k_e(a-x_1)} + NA_6 e^{-x_1} \tag{3.3c}$$

$$\theta_R(x_2) = -iPB_3e^{-ik_px_2} + iPB_4e^{-ik_p(b-x_2)} - NB_5e^{-k_ex_2} + NB_6e^{-k_e(b-x_2)} \quad (3.3d)$$

3.1.3 Dynamic Behaviors

Eq. (3.3) contains twelve unknowns, four from the axial mode and eight from the bending mode, as shown in Fig. 3.2. Detailed information on the unknowns is provided in Section 2.2.3. Fig. 3.2 shows how the dynamic behavior of a cracked beam is approximated to develop a frequency equation. When the frequency is sufficiently high, an evanescent wave mode generated at a certain position will quickly decay as soon as it is created. For example, as soon as an evanescent bending mode (A_5) is created at beam support *A*, it will decay exponentially with distance from *A*. Arriving at the left side of the crack as an incident evanescent wave mode ($A_5e^{-k_ea}$), its contribution will be negligible because $A_5e^{-k_ea}$ is practically zero. The same applies to the other evanescent bending wave modes A_6, B_5, and B_6, and their respective counterparts $A_6e^{-k_ea}$, $B_5e^{-k_eb}$, and $B_6e^{-k_eb}$. As a result, all evanescent wave modes incident on the crack and beam supports are negligible and do not contribute to the standing wave modes of the beam. Therefore, four incident evanescent wave modes can be neglected in the approximation of the dynamic behavior of a cracked beam, i.e., $A_6e^{-k_ea}$ at *A*, $A_5e^{-k_ea}$ at the left side of *C*, $B_6e^{-k_eb}$ at the right side of *C*, and $B_5e^{-k_eb}$ at *B*, as shown in Fig. 3.2 [Par17, Par18].

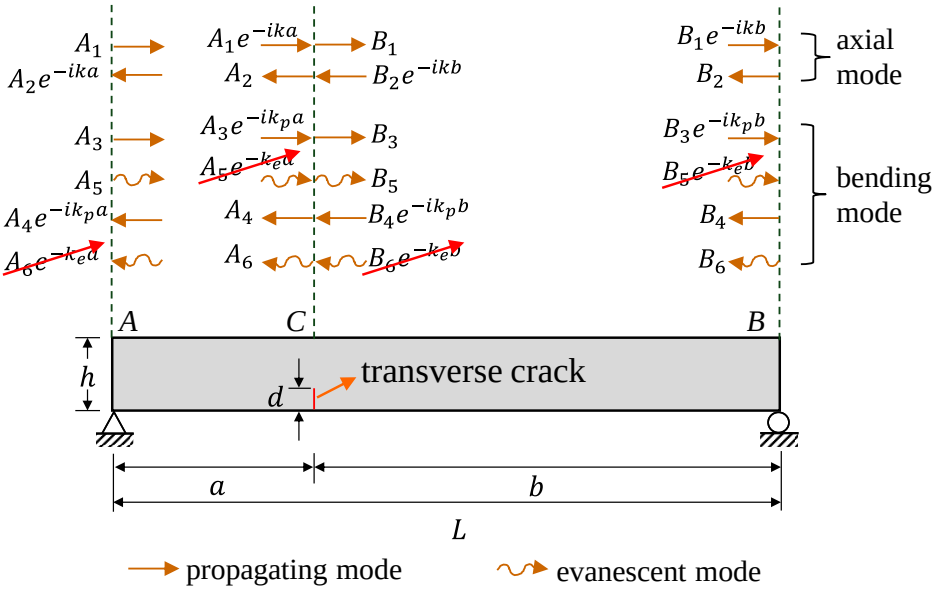


Fig. 3.2 Dynamic behaviors of a cracked beam by neglecting all incident evanescent wave modes associated with bending motions.

3.2 Derivation of the Closed Form Frequency Equation

3.2.1 Twelve Equations for Twelve Unknowns

The twelve equations essential for deriving the frequency equation are established by disregarding the incident evanescent wave modes, as explained in Section 3.1.3. The boundary condition at the supports is assumed to be that of a simply supported beam, which is commonly employed for simplicity of modeling, as shown in Fig. 2.1.

(i) Compatibility of axial displacement at *C*

$$u_R - u_L = F_{aa}u'_L + F_{ab}\theta'_L$$

$$\Rightarrow (1 - ikF_{aa})A_1e^{-ika} + (1 + ikF_{aa})A_2 - F_{ab}(k_pPA_3e^{-ik_pa} + k_pPA_4 - k_eNA_6) - B_1 - B_2e^{-ikb} = 0 \tag{3.4}$$

(ii) Compatibility of transverse displacement at *C*

$$\begin{gathered} w_R - w_L = 0 \\ \Rightarrow A_3 e^{-ik_p a} + A_4 + A_6 - B_3 - B_4 e^{-ik_p b} - B_5 = 0 \end{gathered} \tag{3.5}$$

(iii) Compatibility of rotational angle at *C*

$$\begin{aligned} \theta_R - \theta_L = F_{bb}\theta_L' + F_{ba}u_L' \\ \Rightarrow ikF_{ba}\left(A_1 e^{-ika} - A_2\right) + \left(iP + k_p P F_{bb}\right)A_3 e^{-ik_p a} \\ - \left(iP - k_p P F_{bb}\right)A_4 - (N + k_e N F_{bb})A_6 - iPB_3 \\ + iPB_4 e^{-ik_p b} - NB_5 = 0 \end{aligned} \tag{3.6}$$

(iv) Axial force equilibrium at *C*

$$\begin{gathered} EAu_L' = EAu_R' \\ \Rightarrow A_1 e^{-ika} - A_2 - B_1 + B_2 e^{-ikb} = 0 \end{gathered} \tag{3.7}$$

(v) Shear force equilibrium at *C*

$$\begin{aligned} \kappa GA(-w_L' + \theta_L + w_R' - \theta_R) = 0 \\ \Rightarrow -i\left(P - k_p\right)A_3 e^{-ik_p a} + i\left(P - k_p\right)A_4 - (k_e - N)A_6 \\ + i\left(P - k_p\right)B_3 - i\left(P - k_p\right)B_4 e^{-ik_p b} - (k_e - N)B_5 \\ = 0 \end{aligned} \tag{3.8}$$

(vi) Moment equilibrium at *C*

$$\begin{aligned} EI\theta_L' = EI\theta_R' \\ \Rightarrow k_p P A_3 e^{-ik_p a} + k_p P A_4 - k_e N A_6 - k_p P B_3 - k_p P B_4 e^{-ik_p b} \\ + k_e N B_5 = 0 \end{aligned} \tag{3.9}$$

(vii) Axial displacement boundary condition at *A*

$$\begin{gathered} u_L = 0 \\ \Rightarrow A_1 e^{ika} = -A_2 \end{gathered} \tag{3.10}$$

(viii) Transverse displacement boundary condition at *A*

$$w_L = 0$$
$$\Rightarrow A_3 + A_4 e^{-ik_p a} + A_5 = 0 \tag{3.11}$$

(ix) Moment boundary condition at *A*

$$EI\theta_L' = 0$$
$$\Rightarrow -k_p P A_3 - k_p P A_4 e^{-ik_p a} + k_e N A_5 = 0 \tag{3.12}$$

(x) Axial force boundary condition at *B*

$$EAu_R' = 0$$
$$\Rightarrow B_2 = B_1 e^{-ikb} \tag{3.13}$$

(xi) Transverse displacement boundary condition at *B*

$$w_R = 0$$
$$\Rightarrow B_3 e^{-ik_p b} + B_4 + B_6 = 0 \tag{3.14}$$

(xii) Moment boundary condition at *B*

$$EI\theta_R' = 0$$
$$\Rightarrow -k_p P B_3 e^{-ik_p b} - k_p P B_4 + k_e N B_6 = 0 \tag{3.15}$$

3.2.2 Process of Eliminating Unknowns

Adding $k_p P \times$ Eq. (3.11) to Eq. (3.12) yields:

$$A_5 = 0 \tag{3.16}$$

Adding $k_p P \times$ Eq. (3.14) to Eq. (3.15) yields:

$$B_6 = 0 \tag{3.17}$$

In the case of a simply supported beam, Eqs. (3.16) and (3.17) imply that if the incident evanescent waves are disregarded, no evanescent bending motions are generated at supports *A* and *B*. In cases where the support is either free or fixed, evanescent bending motions must be generated at the support to satisfy the boundary conditions related to force, rotational angle, and moment.

Substituting Eq. (3.16) into Eq. (3.11) results in :

$$A_4 = -A_3 e^{ik_p a} \tag{3.18}$$

Substituting Eq. (3.17) into Eq. (3.14) gives :

$$B_4 = -B_3 e^{-ik_p b} \tag{3.19}$$

Adding $-Pk_p \times$ Eq. (3.5) to Eq. (3.9) results in :

$$B_5 = A_6 \tag{3.20}$$

Substituting Eqs. (3.18)-(3.20) into Eq. (3.8) yields :

$$A_6 = -\frac{i}{2}\gamma_e\left(1 + e^{2ik_p a}\right)A_3 e^{-ik_p a} + \frac{i}{2}\gamma_e\left(1 + e^{-2ik_p b}\right)B_3 \tag{3.21}$$

where $\gamma_e = \frac{k_e}{k_p}$.

Substituting Eqs. (3.10), (3.13), (3.18), and (3.21) into Eq. (3.4) yields the following equation.

$$\begin{aligned}\left\{(1 - ikF_{aa})e^{-ika} - (1 + ikF_{aa})e^{ika}\right\}A_1 \\ -\left\{\left(1 - e^{2ik_p a}\right)k_p P \right. \\ \left. + \frac{i}{2}\gamma_e\left(1 + e^{2ik_p a}\right)k_e N\right\}F_{ab}A_3 e^{-ik_p a} \\ -\left(1 + e^{-2ikb}\right)B_1 + \gamma_e\left(1 + e^{-2ik_p b}\right)k_e N F_{ab}B_3 = 0\end{aligned} \tag{3.22}$$

Substituting Eqs. (3.10), (3.18) through (3.21) into Eq. (3.6) results in :

$$\begin{aligned} & i\left(1+e^{2ika}\right)kF_{ba}A_1e^{-ika} \\ & \quad + \Big[\left(1-e^{2ik_pa}\right)k_pPF_{bb} \\ & \quad + \left\{iP+\frac{i}{2}\gamma_e(2+k_eF_{bb})N\right\}\left(1+e^{2ik_pa}\right)\Big]A_3e^{-ik_pa} \\ & \quad - \left\{iP+\frac{i}{2}\gamma_e(2+k_eF_{bb})N\right\}\left(1+e^{-2ik_pb}\right)B_3=0 \end{aligned} \tag{3.23}$$

Substituting Eqs. (3.10) and (3.13) into Eq. (3.7) yields :

$$\left(1+e^{2ika}\right)A_1e^{-ika}-\left(1-e^{-2ikb}\right)B_1=0 \tag{3.24}$$

Substituting Eqs. (3.18) to (3.20) into Eq. (3.5) results in :

$$\left(1-e^{2ik_pa}\right)A_3e^{-ik_pa}-\left(1-e^{-2ik_pb}\right)B_3=0 \tag{3.25}$$

Substituting Eq. (3.25) into Eq. (3.22) results in :

$$\begin{aligned} & \left\{(1-ikF_{aa})-(1+ikF_{aa})e^{2ika}\right\}\left(1-e^{2ik_pa}\right)A_1e^{-ika} \\ & \quad - \left(1+e^{-2ikb}\right)\left(1-e^{2ik_pa}\right)B_1 \\ & \quad - \Big[\left\{\left(1-e^{2ik_pa}\right)k_pP+\frac{i}{2}\gamma_e\left(1+e^{2ik_pa}\right)k_eN\right\}(1 \\ & \quad - e^{-2ik_pb}) \\ & \quad - \frac{i}{2}\gamma_e\left(1+e^{-2ik_pb}\right)\left(1-e^{2ik_pa}\right)k_eN\Big]F_{ab}B_3=0 \end{aligned} \tag{3.26}$$

Substituting Eq. (3.25) into Eq. (3.23) results in

$$\begin{aligned} & i\left(1+e^{2ika}\right)\left(1-e^{2ik_pa}\right)kF_{ba}A_1e^{-ika} \\ & \quad + \Big[2\left\{iP+\frac{i}{2}\gamma_e(2+k_eF_{bb})N\right\}\left(e^{2ik_pa}-e^{-2ik_pb}\right) \\ & \quad + \left(1-e^{-2ik_pb}\right)\left(1-e^{2ik_pa}\right)k_pPF_{bb}\Big]B_3=0 \end{aligned} \tag{3.27}$$

Substituting Eq. (3.26) into Eq. (3.27) yields the following equation between A_1 and B_1:

$$
\begin{aligned}
&\Big[\big[\big(1-e^{2ik_pa}\big)\big(1-e^{-2ik_pb}\big)k_pP+i\gamma_e\big(e^{2ik_pa}-e^{-2ik_pb}\big)k_eN\big]\big(1\\
&\quad+e^{2ika}\big)kF_{ab}F_{ba}\\
&\quad+\Big[2\Big\{iP+\frac{i}{2}\gamma_e(2+k_eF_{bb})N\Big\}\big(e^{2ik_pa}-e^{-2ik_pb}\big)\\
&\quad+\big(1-e^{-2ik_pb}\big)\big(1-e^{2ik_pa}\big)k_pPF_{bb}\Big]\{(1-ikF_{aa})\\
&\quad-(1+ikF_{aa})e^{2ika}\}\Big]\big(1-e^{2ik_pa}\big)A_1e^{-ika}\\
&\quad-\Big[\Big\{iP+\frac{i}{2}\gamma_e(2+k_eF_{bb})N\Big\}\big(e^{2ik_pa}-e^{-2ik_pb}\big)\\
&\quad+\big(1-e^{-2ik_pb}\big)\big(1-e^{2ik_pa}\big)k_pPF_{bb}\Big]\big(1+e^{-2ikb}\big)\big(1\\
&\quad-e^{2ik_pa}\big)B_1=0
\end{aligned}
\tag{3.28}
$$

Finally, substituting Eq. (3.24) into Eq. (3.28) yields:

$$
\begin{aligned}
&\{-2i(t_L-t_R)-(1-t_L)(1-t_R)kF_{aa}\}\big[2(1+\gamma_e^2)(\bar{t}_L-\bar{t}_R)\\
&\quad+\big\{\big(\gamma_e^3+\gamma_e\gamma_q^2\big)(\bar{t}_L-\bar{t}_R)\\
&\quad+i\big(1-\gamma_q^2\big)(1+\bar{t}_L)(1+\bar{t}_R)\big\}k_pF_{bb}\big]\\
&\quad+(1-t_L)(1-t_R)kF_{aa}\big\{\big(\gamma_e^3+\gamma_e\gamma_q^2\big)(\bar{t}_L-\bar{t}_R)\\
&\quad+i\big(1-\gamma_q^2\big)(1+\bar{t}_L)(1+\bar{t}_R)\big\}k_p\left(\frac{F_{ab}F_{ba}}{F_{aa}}\right)=0
\end{aligned}
\tag{3.29}
$$

where γ_q is defined as $\frac{k_q}{k_p}$, with $k_q=\frac{\omega}{c_Q}$. The parameters t_L, t_R, $\bar{t}_L$ and $\bar{t}_R$ are associated with values related to phase shift, defined respectively as $t_L=-e^{2ika}$, $t_R=e^{-2ikb}$, $\bar{t}_L=-e^{2ik_pa}$ and $\bar{t}_R=-e^{-2ik_pb}$.

By rearranging the terms according to the local flexibility, Eq. (3.29) can be transformed into a closed-form frequency equation with a complicated expression.

$$\Psi_0+\Psi_{aa}F_{aa}+\Psi_{bb}F_{bb}+\Psi_{ba}F_{ab}F_{ba}+\Psi_{aabb}F_{aa}F_{bb}=0 \tag{3.30a}$$

$$\Psi_0=-4i(1+\gamma_e^2)(t_L-t_R)(\bar{t}_L-\bar{t}_R) \tag{3.30b}$$

$$\Psi_{aa}=-2(1+\gamma_e^2)(1-t_L)(1-t_R)(\bar{t}_L-\bar{t}_R)k \tag{3.30c}$$

$$\Psi_{bb} = -2i(t_L - t_R)\{(\gamma_e^3 + \gamma_e\gamma_q^2)(\bar{t}_L - \bar{t}_R) + i(1 - \gamma_q^2)(1 + \bar{t}_R)\}k_p \quad (3.30d)$$

$$\Psi_{ba} = (1 - t_L)(1 - t_R)\{(1 - \gamma_q^2)(1 + \bar{t}_L)(1 + \bar{t}_R) - i(\gamma_e^3 + \gamma_e\gamma_q^2)(\bar{t}_L - \bar{t}_R)\}kk_p \quad (3.30e)$$

$$\Psi_{aabb} = i(1 - t_L)(1 - t_R)\{(1 - \gamma_q^2)(1 + \bar{t}_L)(1 + \bar{t}_R) - i(\gamma_e^3 + \gamma_e\gamma_q^2)(\bar{t}_L - \bar{t}_R)\}kk_p \quad (3.30f)$$

3.2.3 Process of Simplifying Equations

Dividing Eq. (3.29) by $-2(1 + \gamma_e^2)\{2i(t_L - t_R) + (1 - t_L)(1 - t_R)kF_{aa}\}$ results in:

$$\begin{aligned}
&(\bar{t}_L - \bar{t}_R) \\
&+ \frac{1}{2(1 + \gamma_e^2)}\{(\gamma_e^3 + \gamma_e\gamma_q^2)(\bar{t}_L - \bar{t}_R) \\
&+ i(1 - \gamma_q^2)(1 + \bar{t}_L)(1 + \bar{t}_R)\}k_pF_{bb} \\
&- \frac{-\frac{i}{2}(1 - t_L)(1 - t_R)kF_{aa}}{(t_L - t_R) - \frac{i}{2}(1 - t_L)(1 - t_R)kF_{aa}}\left\{\frac{1}{2(1 + \gamma_e^2)}\right\}\{(\gamma_e^3 + \gamma_e\gamma_q^2)(\bar{t}_L \\
&- \bar{t}_R) + i(1 - \gamma_q^2)(1 + \bar{t}_L)(1 + \bar{t}_R)\}k_pF_{bb}\left(\frac{F_{ab}F_{ba}}{F_{aa}F_{bb}}\right) = 0
\end{aligned} \quad (3.31)$$

In Eq. (3.31), partial similarities in form were observed with the frequency equations of intact and uncoupled cracked beams for the axial and bending modes.

The frequency equations of the intact and uncoupled cracked beams for the axial and bending modes are as follows:

$$\Theta_{ao} = t_L - t_R \quad (3.32a)$$

$$\Theta_a = \Theta_{ao} - \frac{i}{2}(1 - t_L)(1 - t_R)kF_{aa} \quad (3.32b)$$

$$\Theta_{bo} = \bar{t}_L - \bar{t}_R \quad (3.32c)$$

$$\Theta_b = \Theta_{bo} + \frac{1}{2(1 + \gamma_e^2)}\{(\gamma_e^3 + \gamma_e\gamma_q^2)(\bar{t}_L - \bar{t}_R) + i(1 - \gamma_q^2)(1 + \bar{t}_L)(1 + \bar{t}_R)\}k_pF_{bb} \quad (3.32d)$$

Eq. (3.31) can be rewritten using the frequency equations for the intact and uncoupled cracked beams in Eq. (3.32).

$$\Theta_b - \frac{\Theta_a - \Theta_{ao}}{\Theta_a}(\Theta_b - \Theta_{bo})\left(\frac{F_{ab}F_{ba}}{F_{aa}F_{bb}}\right) \tag{3.33}$$

The combination of local flexibility, represented as $\left(\frac{F_{ab}F_{ba}}{F_{aa}F_{bb}}\right)$ becomes ABMC factor χ. Thus, multiplying Eq. (3.33) by Θ_a results in the creation of an equation with the mechanical significance of a simplified form.

$$\Theta_a\Theta_b - \chi(\Theta_a - \Theta_{ao})(\Theta_b - \Theta_{bo}) = 0 \tag{3.34}$$

3.3 Implication of the Frequency Equation

In Eq. (3.34), Θ_{ao} and Θ_a represent the uncoupled frequency equations of intact and cracked beams for pure axial modes, respectively, while Θ_{bo} and Θ_b denote those of pure bending modes [Par18], respectively, as long as they are equal to zero. For example, the wave number corresponding to the modal frequency of the pure axial mode is computed through $\Theta_{ao} = 0$ (i.e., $t_L = t_R$) if there is no crack in the beam. Similarly, the wave number associated with the modal frequency of the pure bending mode of an intact beam can be obtained through $\Theta_{bo} = 0$. In the case of a cracked beam, the modal frequencies for the pure axial and pure bending modes are calculated through $\Theta_a = 0$ and $\Theta_b = 0$, respectively. The modal frequencies of a cracked beam for both modes will deviate from those of an intact beam depending on the local flexibility coefficients F_{aa} and F_{bb}. Similar to local flexibilities, the ABMC factor χ in Eq. (3.34) determines the amount of axial–bending coupling

effects on the modal frequencies of a cracked beam compared with the modal frequencies corresponding to pure axial and bending modes. For example, when $\chi = 0$, Eq. (3.34) becomes $\Theta_a\Theta_b = 0$ (i.e., $\Theta_a = 0$ or $\Theta_b = 0$), implying that no modal coupling exists between the axial and bending modes regardless of the crack depth ratio. As χ increases, the modal frequencies computed from Eq. (3.34) are very likely to deviate significantly from those calculated using the uncoupled frequency equation (i.e., Eq. (3.34) with $\chi = 0$) for a given crack depth ratio. In addition, the importance of χ manifests itself in the form of Eq. (3.34). Introducing χ, Eq. (3.34) is decomposed into the variable $\Theta_a\Theta_b$ accounting for the pure axial and bending modes and the variable $-\chi(\Theta_a - \Theta_{ao})(\Theta_b - \Theta_{bo})$ accounting for the contribution of ABMC. The significance of χ also lies in its physical meaning from the viewpoint of fracture mechanics. χ is expressed as the product of two flexibility coefficients (F_{ab} and F_{ba}) divided by that of two flexibility coefficients (F_{aa} and F_{bb}). In the presence of a crack, F_{ab} and F_{ba} represent the local compliance between the axial displacement and the bending moment and between the rotational angle and the axial force, respectively. F_{aa} and F_{bb} denote the local compliance between the axial displacement and the axial force and that between the rotational angle and the bending moment, respectively. Therefore, χ represents the ratio of the product of local compliances affecting axial–bending coupling to that affecting the pure axial and bending modes.

Fig. 3.3 illustrates the approximate magnitude of an ABMC factor of 1.0 for the crack depth ratio throughout a crack depth ratio range of 0–0.7. The maximum error

deviating from 1.0 is only 2% when the crack depth ratio is approximately 0.6. Eq. (3.34) can be expressed approximately by substituting $\chi = 1$ for simplicity of the description of its characteristics as follows:

$$\Theta_a \Theta_b = (\Theta_a - \Theta_{ao})(\Theta_b - \Theta_{bo}) \tag{3.35}$$

If the crack depth ratio is very small, the right-hand side of Eq. (3.35) disappears because F_{aa} in Eq. (3.32b) and F_{bb} in Eq. (3.32d) almost become zero, and thus Θ_a and Θ_b approach Θ_{ao} and Θ_{bo}, respectively. In this case, Eq. (3.34) becomes $\Theta_a \Theta_b \approx 0$, from which either the modal frequencies for pure axial or pure bending modes are obtained. As the crack depth ratio increases, the right-hand side of Eq. (3.35) deviates from zero, and more axial–bending coupling effects on the modal frequency are anticipated. The axial-bending coupling effects in Eq. (3.35) become significant when the modal frequency of a certain pure axial mode is in the vicinity of that of a certain pure bending mode or vice versa. Under these circumstances, either Θ_a or Θ_b approaches zero. After dividing Eq. (3.35) by either $\Theta_a \approx 0$ or $\Theta_b \approx 0$, Eq. (3.35) can be rewritten as follows:

$$|\Theta_b| = \left|\frac{(\Theta_a - \Theta_{ao})(\Theta_b - \Theta_{bo})}{\Theta_a}\right| \gg 0 \text{ or } |\Theta_a| = \left|\frac{(\Theta_a - \Theta_{ao})(\Theta_b - \Theta_{bo})}{\Theta_b}\right| \gg 0 \tag{3.36}$$

Eq. (3.36) implies that the modal frequency satisfying Eq. (3.35) should deviate significantly from that associated with the pure axial or pure bending mode because the right-hand side of Eq. (3.35) will depart considerably from zero. This aspect of the ABMC is well presented in the numerical and experimental validation of Section 3.4.

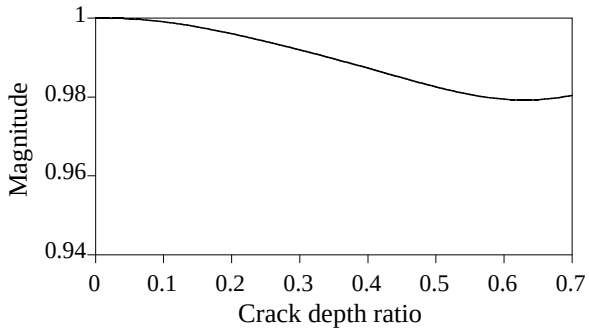


Fig. 3.3 ABMC factor for crack depth ratio in Eq. (3.34).

3.4 Extending the Frequency Equation to Other Support Conditions

By replacing Eqs. (3.10)-(3.15) with boundary conditions for different support conditions and conducting the same procedure in Section 3.1 for all support conditions, only the coefficients β_L, β_R, $\bar{\beta}_L$, and $\bar{\beta}_R$ in t_L, t_R, $\bar{t}_L$, and $\bar{t}_R$, as shown in Table 1, depending on the support condition, and can be expressed by the same frequency equation as Eq. (3.34) [Par17]:

$$t_L = \beta_L e^{2ika} \tag{3.37a}$$

$$t_R = \beta_R e^{-2ikb} \tag{3.37b}$$

$$\bar{t}_L = \bar{\beta}_L e^{2ik_p a} \tag{3.37c}$$

$$\bar{t}_R = \bar{\beta}_R e^{-2ik_p b} \tag{3.37d}$$

The principles of β_L, β_R, $\bar{\beta}_L$, and $\bar{\beta}_R$ can be explained following the procedure used by Park [Par17] to determine phase differences.

Table 3.1 Phase shift at the left and right end of a beam according to support conditions

Support condition / Support position	Hinge roller (simply supported)	Fixed–free (cantilever)	Fixed roller (propped cantilever)
Left end*	$\beta_L = -1$ $\phi_L = -\pi$ $\bar{\beta}_L = -1$ $\bar{\phi}_L = -\pi$	$\beta_L = -1$ $\phi_L = -\pi$ $\bar{\beta}_L = \bar{\beta}_{fix}$ *** $\bar{\phi}_L = \arg[\bar{\beta}_{fix}]$	$\beta_L = -1$ $\phi_L = -\pi$ $\bar{\beta}_L = \bar{\beta}_{fix}$ $\bar{\phi}_L = \arg[\bar{\beta}_{fix}]$
Right end**	$\beta_R = 1$ $\phi_R = 0$ $\bar{\beta}_R = -1$ $\bar{\phi}_R = \pi$	$\beta_R = 1$ $\phi_R = 0$ $\bar{\beta}_R = \bar{\beta}_{free}$ *** $\bar{\phi}_R = \arg[\bar{\beta}_{free}]$	$\beta_R = 1$ $\phi_R = 0$ $\bar{\beta}_R = -1$ $\bar{\phi}_R = \pi$
Support condition / Support position	Fixed–fixed (both fixed)	Hinge free	Free–free
Left end*	$\beta_L = -1$ $\phi_L = -\pi$ $\bar{\beta}_L = \bar{\beta}_{fix}$ $\bar{\phi}_L = \arg[\bar{\beta}_{fix}]$	$\beta_L = -1$ $\phi_L = -\pi$ $\bar{\beta}_L = -1$ $\bar{\phi}_L = -\pi$	$\beta_L = 1$ $\phi_L = 0$ $\bar{\beta}_L = \frac{1}{\bar{\beta}_{free}}$ $\bar{\phi}_L = \arg[\frac{1}{\bar{\beta}_{free}}]$
Right end**	$\beta_R = -1$ $\phi_R = \pi$ $\bar{\beta}_R = \frac{1}{\bar{\beta}_{fix}}$ $\bar{\phi}_R = \arg[\frac{1}{\bar{\beta}_{fix}}]$	$\beta_R = 1$ $\phi_R = 0$ $\bar{\beta}_R = \bar{\beta}_{free}$ $\bar{\phi}_R = \arg[\bar{\beta}_{free}]$	$\beta_R = 1$ $\phi_R = 0$ $\bar{\beta}_R = \bar{\beta}_{free}$ $\bar{\phi}_R = \arg[\bar{\beta}_{free}]$

* $\beta_L = e^{i\phi_L}$, $\bar{\beta}_L = e^{i\bar{\phi}_L}$ ** $\beta_R = e^{i\phi_R}$, $\bar{\beta}_R = e^{i\bar{\phi}_R}$

*** $\bar{\beta}_{fix} = \frac{P+iN}{P-iN}$, $\bar{\beta}_{free} = -\frac{P+i\gamma_e^2 N}{P-i\gamma_e^2 N}$

Fig. 3.4 shows the physical implications of t_L and t_R from an axial wave perspective. On the left side of the crack, the difference in the phase shift between A_2 departing from *C* and $A_1 e^{-ika}$ approaching *C* is due to the round-trip wave traveling in the reverse direction and the wave reflection at *A*. ka and ϕ_L denote the phase shifts caused by the one-way wave traveling in the reverse direction and the wave reflection at A, respectively. The total phase shifts of the wave traveling from the crack, passing through support *A*, and returning to the crack can be expressed by the relationship between A_1 and A_2:

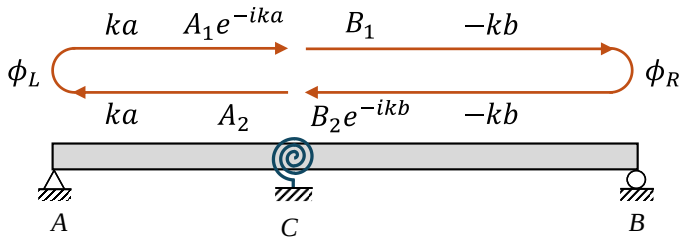
$$A_2 = t_L A_1 e^{-ika} \tag{3.38}$$

where $t_L = e^{i(ka+\phi_L+ka)} = e^{i\phi_L} e^{2ika}$ which is identical to Eq. (3.37a).

Similarly, the difference in the phase shift between and B_1 departing from *C* and $B_2 e^{-ikb}$ approaching *C* is due to the round-trip wave traveling in the forward direction and the wave reflection at *B*. $-kb$ and ϕ_R denote the phase shifts caused by the one-way wave traveling in the forward direction and the wave reflection at *B*, respectively. The total phase shifts of the wave traveling from the crack, passing through support *B*, and returning to the crack can be expressed by the relationship between B_1 and B_2:

$$B_2 e^{-ikb} = t_R B_1 \tag{3.39}$$

where $t_R = e^{i(-kb+\phi_R-kb)} = e^{i\phi_R} e^{-2ikb}$ which is identical to Eq. (3.37b).



$$A_2 = t_L A_1 e^{-ika} \qquad B_2 e^{-ikb} = t_R B_1$$

$$t_L = e^{i(ka+\phi_L+ka)} = \underbrace{e^{i\phi_L}}_{\beta_L} e^{2ika} \qquad t_R = e^{i(-kb+\phi_R-kb)} = \underbrace{e^{i\phi_R}}_{\beta_R} e^{-2ikb}$$

Fig. 3.4 The physical implications of t_L and t_R from an axial wave perspective.

Fig. 3.5 shows the physical implications of $\bar{t}_L$ and $\bar{t}_R$ from a bending wave perspective. On the left side of the crack, the difference in the phase shift between A_4 departing from *C* and A_3e^{-ika} approaching *C* is due to the round-trip wave traveling in the reverse direction and the wave reflection at *A*. k_pa and $\bar{\phi}_L$ denote the phase shifts caused by the one-way wave traveling in the reverse direction and the wave reflection at *A*, respectively. The total phase shifts of the wave traveling from the crack, passing through support *A*, and returning to the crack can be expressed by the relationship between A_3 and A_4:

$$A_4 = \bar{t}_L A_3 e^{-ik_pa} \tag{3.40}$$

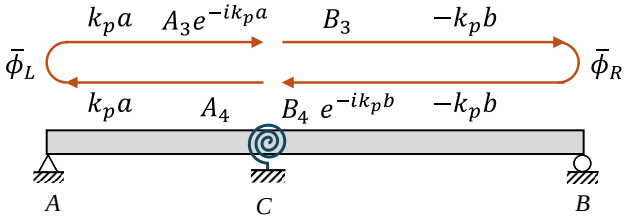
where $\bar{t}_L = e^{i(k_pa+\bar{\phi}_L+k_pa)} = e^{i\bar{\phi}_L}e^{2ika}$ which is identical to Eq. (3.37c).

Similarly, the difference in the phase shift between and B_1 departing from *C* and $B_2e^{-ik_pb}$ approaching *C* is due to the round-trip wave traveling in the forward direction and wave reflection at *B*. $-k_pb$ and $\bar{\phi}_R$ denote the phase shifts caused by the one-way wave traveling in the forward direction and wave reflection at *B*. The

total phase shifts of the wave traveling from the crack, passing through support *B*, and returning to the crack can be expressed by the relationship between B_3 and B_4:

$$B_4 e^{-ik_p b} = \bar{t}_R B_3 \tag{3.41}$$

where $\bar{t}_R = e^{i(-k_p b + \bar{\phi}_R - k_p b)} = e^{i\bar{\phi}_R} e^{-2ik_p b}$ which is identical to Eq. (3.37d).



$$A_4 = \bar{t}_L A_3\ e^{-ik_p a} \qquad B_4 e^{-ik_p b} = \bar{t}_R B_3$$

$$\bar{t}_L = e^{i(k_p a + \bar{\phi}_L + k_p a)} = \underbrace{e^{i\bar{\phi}_L}}_{\bar{\beta}_L}\ e^{2ik_p a} \qquad \bar{t}_R = e^{i(-k_p b + \bar{\phi}_R - k_p b)} = \underbrace{e^{i\bar{\phi}_R}}_{\bar{\beta}_R}\ e^{-2ik_p b}$$

Fig. 3.5 The physical implications of $\bar{t}_L$ and $\bar{t}_R$ from a bending wave perspective.

The detailed process of β_L, β_L, $\bar{\beta}_L$, $\bar{\beta}_L$ for each support in Table 3.1 obtained from the phase change difference is detailed in Appendix (A5).

3.5 Newton-Raphson Method for a Solving Nonlinear Equation

Since Eq. (3.34) is a nonlinear equation with respect to ω, the modal frequencies are calculated using the same Newton-Raphson (N-R) method described in Section 2.5.1. The basic methodology remains unchanged; however, the procedure initially diverges by focusing on linearizing the closed-form frequency equation rather than linearizing the determinants of the matrices as previously applied. Eq. (3.34) is defined as y, which is shown in the following equation:

$$y = \Theta_a \Theta_b - \chi(\Theta_a - \Theta_{ao})(\Theta_b - \Theta_{bo}) \tag{3.42}$$

The iteration process of Eqs. (2.44)-(2.46) is conducted until convergence to 10^{-7} is obtained according to the criterion given in Eq. (2.47). The derivative $\frac{\partial y}{\partial \omega}$ used in Eq. (2.44) can be expressed by applying the chain rule.

$$\frac{\partial y}{\partial \omega} = \frac{\partial y}{\partial k}\frac{\partial k}{\partial \omega} + \frac{\partial y}{\partial k_p}\frac{\partial k_p}{\partial \omega} \tag{3.43}$$

where k_p, k_e, P, and N were set as independent variables to use the chain rule in Section 2.5.2, as all coefficients are used in the chain rule. However, in this chapter, only k_p is used in the chain rule, so note that k_p, k_e, P, and N are correlated with each other by ω.

The derivatives $\frac{\partial y}{\partial k}$ and $\frac{\partial y}{\partial k_p}$ used in Eq. (3.43) is obtained by differentiating Eq. (3.42) with respect to k and k_p, respectively.

$$\frac{\partial y}{\partial k} = \frac{\partial \Theta_a}{\partial k}\Theta_b - \chi\left(\frac{\partial \Theta_a}{\partial k} - \frac{\partial \Theta_{ao}}{\partial k}\right)(\Theta_b - \Theta_{bo}) = 0 \tag{3.44a}$$

$$\frac{\partial y}{\partial k_p} = \Theta_a \frac{\partial \Theta_b}{\partial k_p} - \chi(\Theta_a - \Theta_{ao})\left(\frac{\partial \Theta_b}{\partial k_p} - \frac{\partial \Theta_{bo}}{\partial k_p}\right) = 0 \tag{3.44b}$$

The derivatives $\frac{\partial \Theta_{ao}}{\partial k}$ and $\frac{\partial \Theta_a}{\partial k}$ in Eq. (3.44a) are obtained by differentiating the frequency equations corresponding to the axial mode of both the intact and cracked beams with respect to k.

$$\frac{\partial \Theta_{ao}}{\partial k} = \frac{\partial t_L}{\partial k} - \frac{\partial t_R}{\partial k} \tag{3.45a}$$

$$\frac{\partial \Theta_a}{\partial k} = \frac{\partial \Theta_{ao}}{\partial k} - \frac{i}{2}(-\frac{\partial t_L}{\partial k})(1 - t_R)kF_{aa} - \frac{i}{2}(1 - t_L)(-\frac{\partial t_R}{\partial k})kF_{aa} - \frac{i}{2}(1 - t_L)(1 - t_R)F_{aa} \tag{3.45b}$$

The derivatives $\frac{\partial \Theta_{bo}}{\partial k_p}$ and $\frac{\partial \Theta_b}{\partial k_p}$ in Eq. (3.44b) are obtained by differentiating the frequency equations corresponding to the bending mode of both intact and cracked beams with respect to k_p.

$$\frac{\partial \Theta_{bo}}{\partial k_p} = \frac{\partial \bar{t}_L}{\partial k_p} - \frac{\partial \bar{t}_R}{\partial k_p} \tag{3.46a}$$

$$\begin{aligned}\frac{\partial \Theta_b}{\partial k_p} = {} & 2\left(2\gamma_e \frac{\partial \gamma_e}{\partial k_p}\right)\Theta_{bo} + 2(1+\gamma_e^2)\frac{\partial \Theta_{bo}}{\partial k_p} \\ & + \left\{\left(3\gamma_e^2 \frac{\partial \gamma_e}{\partial k_p} + \frac{\partial \gamma_e}{\partial k_p}\gamma_q^2 + 2\gamma_e\gamma_q \frac{\partial \gamma_q}{\partial k_p}\right)(\bar{t}_L - \bar{t}_R)\right. \\ & + \left(\gamma_e^3 + \gamma_e\gamma_q^2\right)\left(\frac{\partial \bar{t}_L}{\partial k_p} - \frac{\partial \bar{t}_R}{\partial k_p}\right) \\ & + i\left(-2\gamma_q \frac{\partial \gamma_q}{\partial k_p}\right)(1+\bar{t}_L)(1+\bar{t}_R) \\ & + i\left(1-\gamma_q^2\right)\frac{\partial \bar{t}_L}{\partial k_p}(1+\bar{t}_R) \\ & \left. + i\left(1-\gamma_q^2\right)(1+\bar{t}_L)\frac{\partial \bar{t}_R}{\partial k_p}\right\} k_p F_{bb} \\ & + \left\{\left(\gamma_e^3 + \gamma_e\gamma_q^2\right)(\bar{t}_L - \bar{t}_R)\right. \\ & \left. + i\left(1-\gamma_q^2\right)(1+\bar{t}_L)(1+\bar{t}_R)\right\} F_{bb}\end{aligned} \tag{3.46b}$$

The derivatives $\frac{\partial t_L}{\partial k}$ and $\frac{\partial t_R}{\partial k}$ used in Eq. (3.45) and $\frac{\partial \bar{t}_L}{\partial k_p}$ and $\frac{\partial \bar{t}_R}{\partial k_p}$ in Eq. (3.46) are Eq. (3.37) with respect to k and k_p, respectively.

$$\frac{\partial t_L}{\partial k} = 2ia\beta_L e^{2ika} \tag{3.47a}$$

$$\frac{\partial t_R}{\partial k} = -2ib\beta_R e^{-2ikb} \tag{3.47b}$$

$$\frac{\partial \bar{t}_L}{\partial k_p} = \frac{\partial \bar{\beta}_L}{\partial k_p} e^{2ik_p a} + 2ia\bar{\beta}_L e^{2ik_p a} \tag{3.47c}$$

$$\frac{\partial \bar{t}_R}{\partial k_p} = \frac{\partial \bar{\beta}_R}{\partial k_p} e^{-2ik_p b} - 2ib\bar{\beta}_R e^{-2ik_p b} \tag{3.47d}$$

where k_p, k_e, P, and N are related, all coefficients associated with them must be

derived by differentiating with respect to k_p.

$\frac{\partial \gamma_e}{\partial k_p}$ and $\frac{\partial \gamma_q}{\partial k_p}$ in Eq. (4.46b) are the derivatives of γ_e and γ_q with respect to k_p, which can be described as follows:

$$\frac{\partial \gamma_e}{\partial k_p} = \frac{\frac{\partial k_e}{\partial k_p} - \gamma_e}{k_p} \tag{3.48a}$$

$$\frac{\partial \gamma_q}{\partial k_p} = \frac{\frac{\partial k_q}{\partial k_p} - \gamma_q}{k_p} \tag{3.48b}$$

$\frac{\partial k_e}{\partial k_p}$ in Eq. (3.48a) can be obtained from Eqs. (2.25) and (2.26). By substituting $X = \bar{k}_p^2 - \bar{k}_e^2$ which is derived from Eqs. (2.25a) and (2.25b) into Eq. (2.26a) produces:

$$k_p^2 - k_e^2 = \omega^2 \left(\frac{1}{c_0^2} + \frac{1}{c_q^2} \right) \tag{3.49}$$

Differentiating Eq. (3.49) with respect to k_p yields $\frac{\partial k_e}{\partial k_p}$.

$$\frac{\partial k_e}{\partial k_p} = \frac{k_p}{k_e} - \frac{\omega}{k_e} \frac{\partial \omega}{\partial k_p} \left(\frac{1}{c_0^2} + \frac{1}{c_q^2} \right) \tag{3.50}$$

$\frac{\partial k_q}{\partial k_p}$ in Eq. (3.48b) is defined by:

$$\frac{\partial k_q}{\partial k_p} = \frac{\frac{\partial \omega}{\partial k_p}}{c_q} \tag{3.51}$$

where $\frac{\partial \omega}{\partial k_p}$ in Eqs. (3.50) and (3.51) used as the same expression as in Eq. (2.52).

Table 3.2 shows $\frac{\partial \bar{\beta}_L}{\partial k_p}$ and $\frac{\partial \bar{\beta}_R}{\partial k_p}$ in Eqs. (3.47c) and (3.47d) are the derivatives of Table 3.1 with respect to k_p.

Table 3.2 Phase shift at the left and right end of a beam according to support conditions, differentiated with respect to k_p

Support position \ Support condition	Hinge roller (simply supported)	Fixed–free (cantilever)	Fixed roller (propped cantilever)
Left end*	$\frac{\partial \bar{\beta}_L}{\partial k_p} = 0$	$\frac{\partial \bar{\beta}_L}{\partial k_p} = \bar{\bar{\beta}}_{fix}$ *	$\frac{\partial \bar{\beta}_L}{\partial k_p} = \bar{\bar{\beta}}_{fix}$
Right end**	$\frac{\partial \bar{\beta}_R}{\partial k_p} = 0$	$\frac{\partial \bar{\beta}_R}{\partial k_p} = \bar{\bar{\beta}}_{free}$ **	$\frac{\partial \bar{\beta}_R}{\partial k_p} = 0$
Support position \ Support condition	Fixed–fixed (both fixed)	Hinge free	Free–free
Left end*	$\frac{\partial \bar{\beta}_L}{\partial k_p} = \bar{\bar{\beta}}_{fix}$	$\frac{\partial \bar{\beta}_L}{\partial k_p} = 0$	$\frac{\partial \bar{\beta}_L}{\partial k_p} = \frac{1}{\bar{\bar{\beta}}_{free}}$
Right end**	$\frac{\partial \bar{\beta}_R}{\partial k_p} = \frac{1}{\bar{\bar{\beta}}_{fix}}$	$\frac{\partial \bar{\beta}_R}{\partial k_p} = \bar{\bar{\beta}}_{free}$	$\frac{\partial \bar{\beta}_R}{\partial k_p} = \bar{\bar{\beta}}_{free}$

* $\bar{\bar{\beta}}_{fix} = \frac{2i\left(\frac{\partial N}{\partial k_p}P - N\frac{\partial P}{\partial k_p}\right)}{(P-iN)^2}$

** $\bar{\bar{\beta}}_{free} = -\frac{2i\left(2\gamma_e\frac{\partial \gamma_e}{\partial k_p}NP + \gamma_e^2\frac{\partial N}{\partial k_p}P - \gamma_e^2 N\frac{\partial P}{\partial k_p}\right)}{(P-i\gamma_e^2 N)^2}$

The derivatives $\frac{\partial P}{\partial k_p}$ and $\frac{\partial N}{\partial k_p}$ in Table 3.2 can be calculated by differentiating Eq. (2.28) with respect to k_p.

$$\frac{\partial P}{\partial k_p} = \left(1 - \frac{\omega^2}{k_p^2 c_q^2}\right) - \left(\frac{2\omega k_p \frac{\partial \omega}{\partial k_p} - 2\omega^2}{k_p^2 c_q^2}\right) \tag{3.52a}$$

$$\frac{\partial N}{\partial k_p} = \frac{\partial k_e}{\partial k_p}\left(1 + \frac{\omega^2}{k_e^2 c_q^2}\right) + \left(\frac{2\omega k_e \frac{\partial \omega}{\partial k_p} - 2\frac{\partial k_e}{\partial k_p}\omega^2}{k_e^2 c_q^2}\right) \tag{3.52b}$$

3.6 Validation

3.6.1 Numerical Example

The proposed frequency equations for beams with cracks located at the bending antinodes were validated by finite element analysis and experimental results. Fig. 3.6 shows a Free-free beam with a transverse crack at the center of a beam with an aspect ratio of 19.8. The crack is located at the center of the beam, and the crack depth ratio varies from 0 to 0.7. The Young's modulus, Poisson ratio, and density of the beam material are 69 GPa, 0.34, and 2700 kg/m^3, respectively. The antinodes of the axial and bending vibration modes of an intact beam are located at the crack location when the mode number is odd because of the symmetry of the free–free beam. In this case, the maximum modal frequency shift due to the crack location for each odd-numbered mode is guaranteed [Par18].

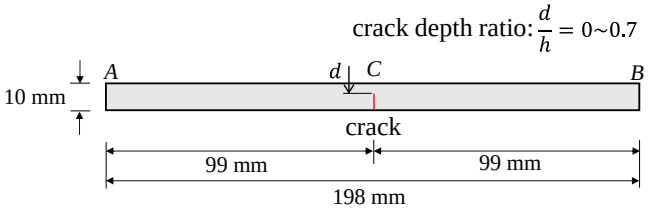


Fig. 3.6 Free-free beam with a transverse crack at the center of a beam with an aspect ratio of 19.8 (width: 10 mm).

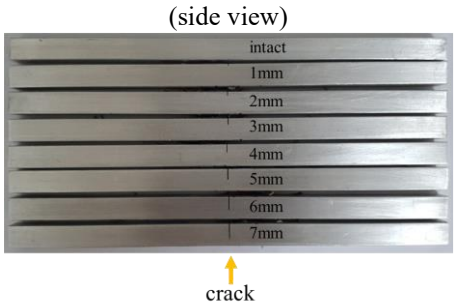
A critical aspect to highlight is the use of shallow beams with an aspect ratio of 19.8. Section 2.6.4 discusses the deep beams with an aspect ratio of 4.2, where the first axial mode is conveniently observable as it is adjacent to the primary observation range of the first to third bending modes. However, for shallow beams

with an aspect ratio above 10, the first axial mode is adjacent to bending modes of the fifth order or higher; thus, the influence of axial-bending modal coupling (ABMC) falls outside the primary observation range. The shallow beams are important for evanescent waves, although they are outside the observation range of interest. The proposed method ignores incident evanescent waves, which leads to inaccuracies in the lower modes, specifically below the third mode [Mea94]. The use of shallow beams is appropriate to demonstrate the proposed method because the effects of axial bending modal coupling occur in modes above the third order, where the effects of evanescent waves are almost negligible.

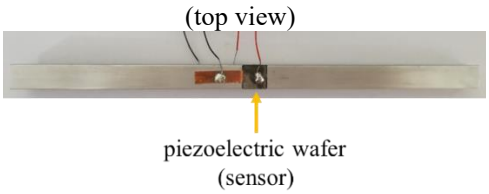
3.6.2 Experimental Setup

Fig. 3.7 shows the experimental setup for validating the proposed method. Four groups of aluminum beams with varying crack depth ratios were manufactured according to the geometry shown in Fig. 3.6. One group consists of eight beams, including an intact beam and beams with seven different crack depth ratios ranging from 0.1 to 0.7 (Fig. 3.7(a)). The crack at the center of the beam is simulated by a 0.3-mm-wide notch with a certain desired depth. Two piezoelectric wafers (Piezo Systems Inc. PSI-5A4E L10 mm × T0.191 mm × W10 mm) [Psi19] were mounted on each beam to capture the dynamic response of each beam via a pitch-catch method. A sensing piezoelectric wafer is mounted at the top center of the beam (Fig. 3.7(b)), while an actuating piezoelectric wafer is bonded 8 mm away from the crack at the bottom center of the beam (Fig. 3.7(c)). The free-free support condition

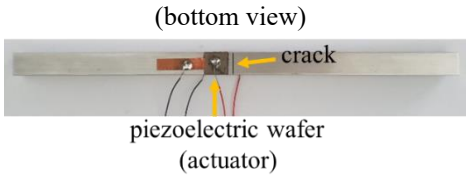
is simulated by suspending the intact and cracked beams by two strings attached 10 mm away from each end of a beam because the effect of string locations on the modal frequencies of beams is negligible compared to experimental uncertainties caused by manufacturing errors, temperature variations, and measurement noise (Fig. 3.7(d)). A chirp voltage input signal with a driving frequency range of 1–130 kHz is exerted on the actuating piezoelectric wafer using a 16-bit arbitrary waveform generator (NI PXI-5422). The duration and amplitude of the chirp voltage input signal are 1 s and 5 V, respectively. The corresponding output voltage signal is measured using a 14-bit high-speed digitizer (NI PXIe-5122). The sampling rate and frequency resolution are 5 MHz and 1 Hz, respectively. The measurement time corresponding to the frequency resolution is 1 s to allow sufficient time for the dynamic motion of the beam to decay out. The experiment is repeated 10 times automatically using LabVIEW^{TM} to obtain an average measured output voltage signal. An example of the average output voltage signal of an intact beam is presented in Fig. 3.7(e). The dotted line indicates the time instant at which the driving frequency of the input chirp signal became identical to each odd modal frequency of the intact beam. The resonance phenomenon associated with each odd modal frequency from 1 kHz to 130 kHz is clearly shown in Fig. 3.7(e). The frequency response spectrum of each beam is computed by Fast Fourier Transform using the input and output voltage signals. The peak frequencies are extracted from the frequency response spectrum, and the associated modes are identified by comparison with the modal frequencies computed from the finite element analysis [Fig. 3.7(f)].



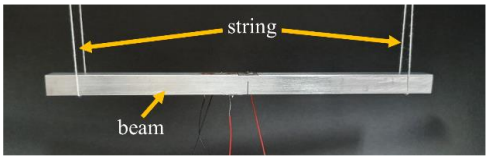
(a) group of eight aluminum beams with increasing crack depths



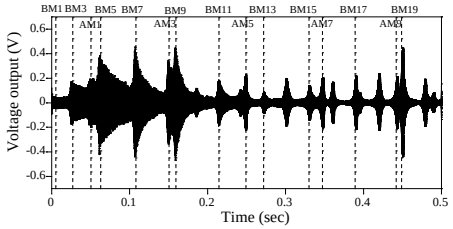
(b) sensing piezoelectric wafers mounted on the top of an aluminum beam



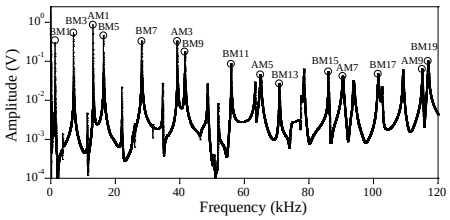
(c) actuating piezoelectric wafers mounted on the bottom of an aluminum beam



(d) beam suspended by two strings in a free–free support condition



(e) example of intact beam average output voltage signal



(f) frequency response spectrum of (e) and modal frequencies

Fig. 3.7 Experimental setup.

3.6.3 Finite Element Analysis Setup

Finite element analysis was conducted using ABAQUS 6.14/standard in SINBARAM at the KISTI Supercomputing Center. The actual thickness and length of all four groups of aluminum beams were measured using a caliper with a 1/100 mm resolution. The average thickness and length values used to obtain the numerical

results from the proposed method and the finite element analysis are 10.25 mm and 197.94 mm, respectively. A sufficiently refined mesh layout (811,800 eight-node quadratic solid elements of size L50 μm × T50 μm) is employed for element discretization to accurately compute the modal frequency changes. The mechanical behavior of a crack is simulated by generating double nodes at the traction-free crack surface during finite element discretization [Par18]. The modal frequencies are computed for comparison with the finite element analysis in which the finite elements associated with a notch region are removed because the mass reduction effects owing to a notch may produce significant changes in the modal frequencies of a cracked beam [Cal16]. The mass reduction effects owing to notches on the computed modal frequencies are negligible compared with the experimental uncertainty in an overall sense. The increment of the varying crack depth ratio was set to 0.05 for the finite element analysis.

3.6.4 Free-Free Beam with a Crack at the Bending Antinode for an Aspect Ratio of 19.8

Table 3.3(a) provides the mean values of the experimental modal frequencies of the intact beams of the four groups. There are 5 axial modes and 10 bending modes with odd mode numbers up to the nineteenth bending mode. No even-numbered axial and bending modes are considered because the center crack is located on the node of the associated vibration mode, where frequency shifts rarely occur. The consistency of the experimental modal frequencies was confirmed through the ratio of the

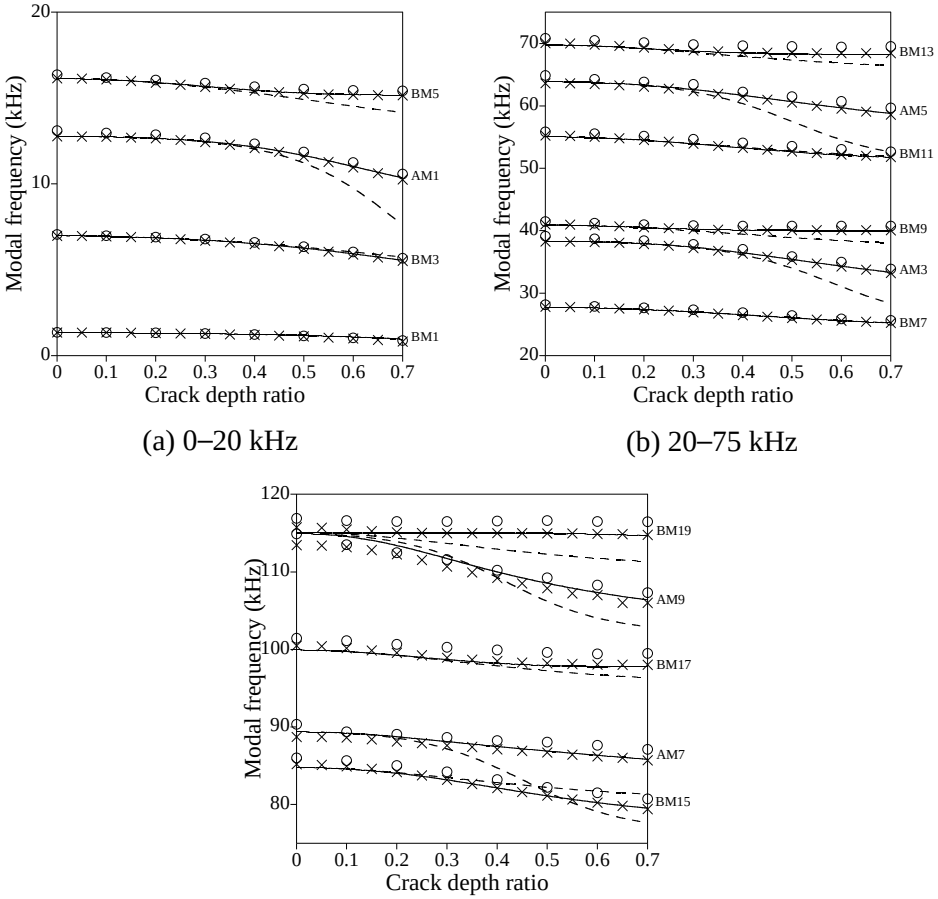
standard deviation of the experimental modal frequencies to their mean values of which the maximum is less than 0.42%. Table 3.3(b) presents the mean fractional reduction values in the modal frequency of a cracked beam compared to that of an intact beam.

Table 3.3 Experimental results: (a) mean experimental modal frequencies of intact beams (unit: kHz); (b) mean fractional reduction values in the modal frequency of a cracked beam compared to that of an intact beam (unit: %)

Crack depth ratio / Mode no.	Intact[(a)]	0.1[(b)]	0.2[(b)]	0.3[(b)]	0.4[(b)]	0.5[(b)]	0.6[(b)]	0.7[(b)]
BM1[*]	1.365	1.282	2.858	5.331	9.526	15.74	24.20	35.65
BM3	7.060	1.087	2.188	3.870	6.501	10.09	14.60	19.66
AM1	13.10	1.101	1.771	3.200	5.849	9.490	14.10	19.32
BM5	16.35	0.9631	1.864	2.967	4.210	5.103	5.528	5.714
BM7	28.14	0.8956	1.735	2.905	4.455	6.145	7.972	8.889
AM3	39.14	1.120	1.841	3.355	5.460	8.316	10.64	13.40
BM9	41.49	0.6815	1.224	1.580	1.815	1.764	1.735	1.799
BM11	55.83	0.5378	1.252	2.107	3.149	4.110	4.998	5.693
AM5	64.89	0.9817	1.633	2.230	4.111	5.256	6.449	7.989
BM13	70.83	0.5075	1.015	1.391	1.672	1.876	1.987	1.848
BM15	86.01	0.4104	1.136	2.077	3.244	4.401	5.210	6.145
AM7	90.35	1.089	1.443	1.891	2.337	2.567	2.998	3.579
BM17	101.4	0.2879	0.7567	1.134	1.480	1.788	1.953	1.901
AM9	114.9	1.222	2.131	2.903	4.100	4.937	5.752	6.610
BM19	116.9	0.2385	0.3555	0.3446	0.2949	0.2453	0.3433	0.3711

[*] "BM" and "AM" denote the bending and axial mode, respectively, and the number represents the mode.

Fig. 3.8 presents the comparison results of the modal frequencies for the crack depth ratio of the proposed frequency equation with those of the finite element analysis and experiments. The frequency range of interest is 0–120 kHz and includes the first five odd-numbered axial modes and the first ten odd-numbered bending modes. Solid and dotted lines denote the modal frequencies with and without ABMC computed using Eq. (3.34), respectively, and "x" and "o" denote the modal frequencies obtained from the finite element analysis and the experiment, respectively. The modal frequencies without ABMC are simply computed by setting



(a) 0–20 kHz

(b) 20–75 kHz

(c) 75–120 kHz

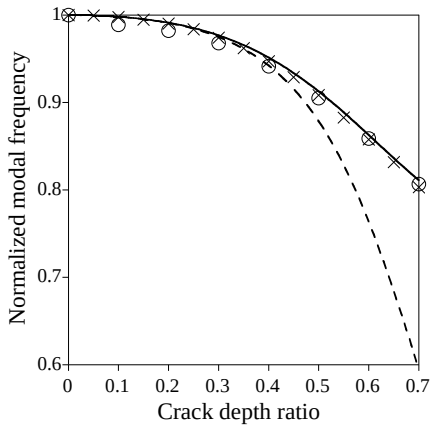
Fig. 3.8 Comparison of modal frequencies proposed by frequency equation to those of finite element analysis and experiments with respect to crack depth ratio (——: proposed method, - - -: conventional method, x: finite element analysis, o: experiment). Letters "BM" and "AM" stand for bending and axial modes, respectively.

the ABMC factor χ to 0. The N-R method is employed to solve Eq. (3.34) because it is a nonlinear equation for the angular frequency ω. The increment for varying the crack depth ratio is set to 0.005. The initial guess is the modal frequency of an intact beam for the first crack depth ratio ($\bar{\delta} = 0.005$) of which the solution is obtained iteratively through the N-R method. Then, the solution for the current crack depth

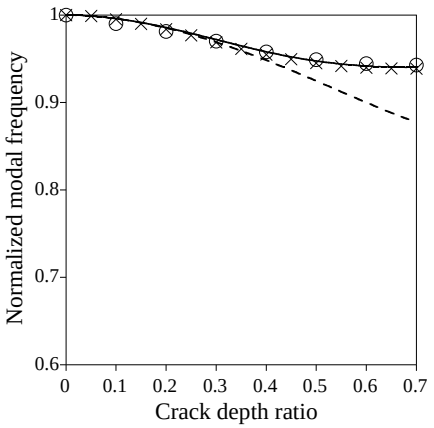
ratio ($\bar{\delta} = 0.005$) becomes the initial guess for the next crack depth ratio ($\bar{\delta} = 0.01$). In this way, the convergence of the N-R method is guaranteed to predict the modal frequencies for the crack depth ratio. Overall, the modal frequencies with ABMC agree well with those of the finite element analysis and the experiment. The effect of ABMC on both the axial and bending modal frequencies is significant for the crack depth ratio when the two modes are adjacent to each other.

Fig. 3.9 presents the comparison results of normalized modal frequencies for five axial and six bending modes in Fig. 3.8, in which the effects of ABMC are noticeable as the crack depth ratio increases. Here, the normalized modal frequency (NMF) denotes the modal frequency for the crack depth ratio divided by that of an intact beam. The symbols in Fig. 3.9 have meanings identical to those in Fig. 3.8. An excellent agreement is observed for all axial and bending modes when ABMC is considered. This means that the banding antinodes are not affected by the mode II crack, as mentioned in Section 2.6, so accurate predictions can be made by considering only the mode I crack. The effects of ABMC on the NMF begin to appear when the crack depth ratio is approximately 0.3 and become progressively more significant as the crack becomes deeper. All the normalized modal frequencies without ABMC presented in Fig. 3.9 agree with those of the finite element analysis up to a crack depth ratio of 0.3, although a slight difference exists in the axial and bending modes within a 1.2% relative error. Furthermore, the modal frequencies corresponding to the axial and bending modes deviate from those calculated by the finite element analysis as the crack depth ratio becomes larger than 0.4. The

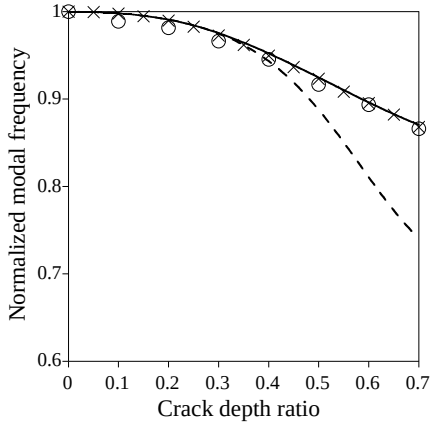
maximum relative errors become 26% and 6.5% for the axial and bending modes, respectively, when the crack depth ratio is 0.7. The modal frequencies with ABMC agree well with those of the finite element analysis for all modes. The maximum relative errors for the axial and bending modes significantly decrease to 1% and 0.64%, respectively, with a crack depth ratio of 0.7. This implies that the effects of ABMC on the modal frequencies appear for the crack depth ratio when the intact modal frequency of the bending mode is in the vicinity of that of the axial mode, as described in Section 3.3.



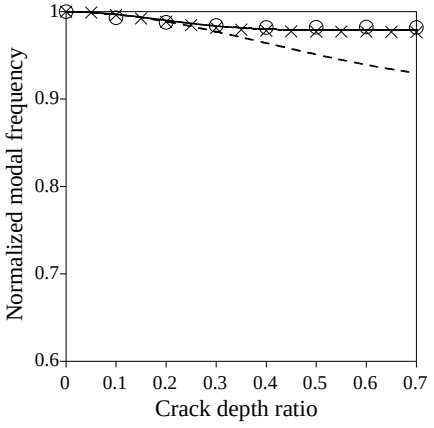
(a) 1st axial mode



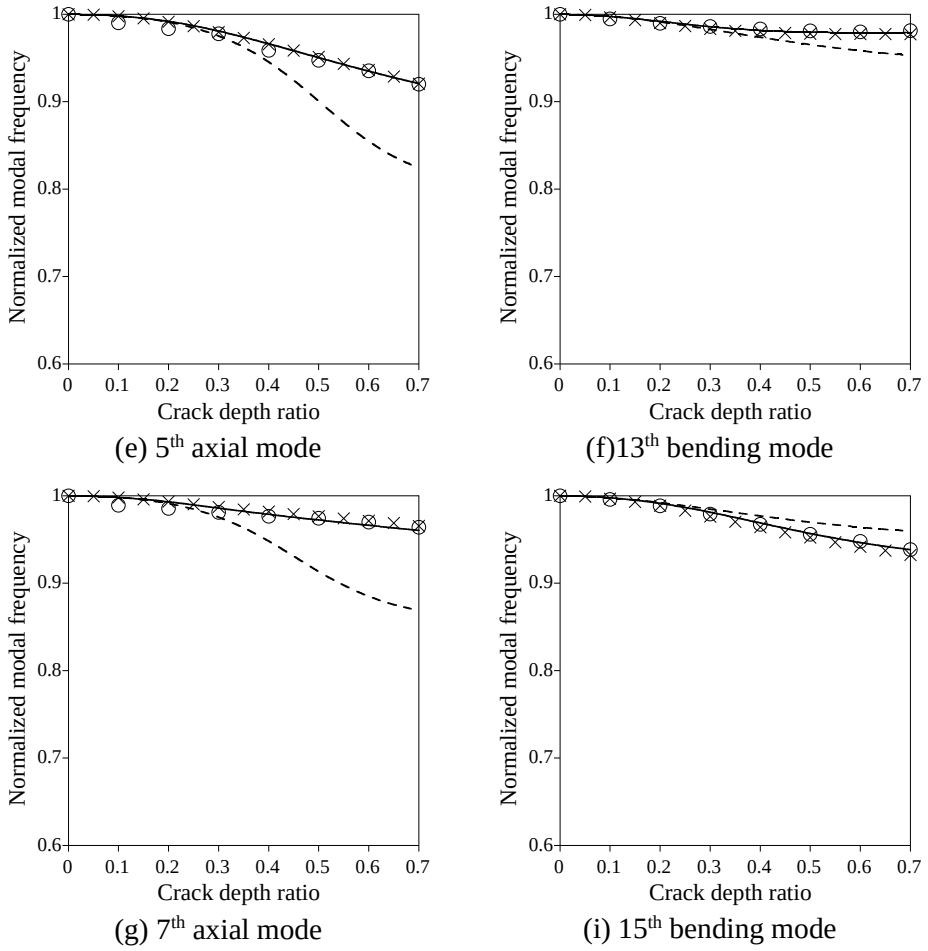
(b) 5th bending mode



(c) 3rd axial mode



(d) 9th bending mode



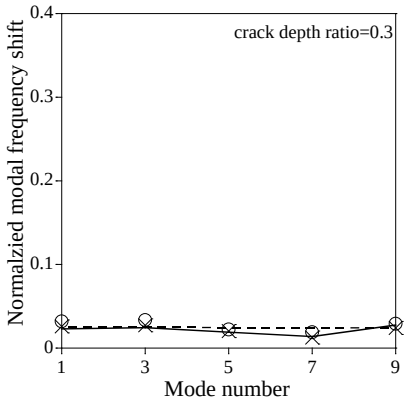
(e) 5th axial mode (f)13th bending mode

(g) 7th axial mode (i) 15th bending mode

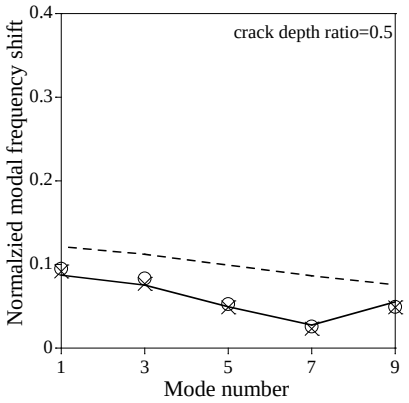
Fig. 3.9 Normalized modal frequencies with respect to crack depth ratios (——: proposed method, - - -: conventional method, x: finite element analysis, o: experiment).

Fig. 3.10 shows the normalized modal frequency shifts (NMFS) by mode number for crack depth ratios of 0.3, 0.5, and 0.7 representing incipient, intermediate, and deep cracks, respectively. Here, the NMFS represents the fractional reduction in the modal frequency due to a crack and is computed as 1 minus the NMF associated with a certain crack depth ratio. The symbol meanings in Fig. 3.10 are identical to those in Fig. 3.8, except for the case of ABMC denoted by a square box symbol.

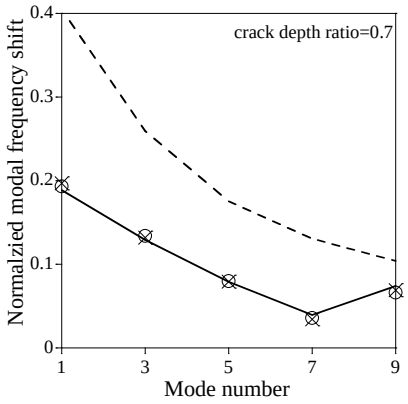
The use of a bar graph, as shown in Figure 2.7, is more appropriate because it does not require interpolation between mode numbers. However, to emphasize the change in the pattern of modal frequency reduction due to ABMC compared to the conventional method, it is represented by a line. Four important implications can be drawn from Fig. 3.10. First, the normalized modal frequency shifts with ABMC are almost identical to those of the finite element analysis and the experiment for all axial and bending modes except for the first bending mode. As shown in Fig. 3.2, the discrepancy in the first bending mode is attributed to the violation of the assumption that the incident evanescent wave motions are negligible. This can be solved using the conventional method because ABMC does not occur up to the first to third order modes. Second, the overall effects of ABMC on the axial modal frequencies become more significant than those of the bending modal frequencies for deeper cracks. Third, as shown in Fig. 3.10(f), the effects of ABMC on the modal frequencies of the first and third bending modes are very small even for a deep crack, because the first axial mode can hardly interact with these two bending modes. This phenomenon explains why few previous studies dealing with the lowest bending frequencies have considered ABMC. Finally, an overall declining trend of NMFS occurs for the mode number for both the axial and bending modes regardless of the magnitude of the crack depth ratio. This phenomenon indicates that the fractional reduction in modal frequencies becomes insensitive to cracks as the mode number increases, which is contradictory to the well-known premise of vibration-based structural health monitoring [Par18]. In particular, the sensitivity of



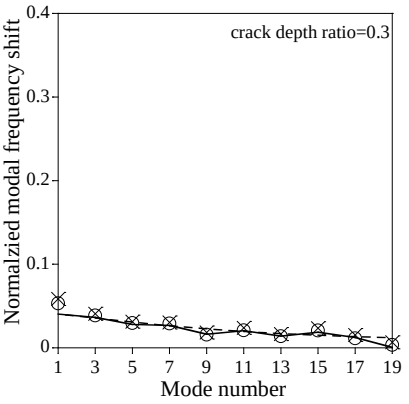
(a) crack depth ratio 0.3 for axial



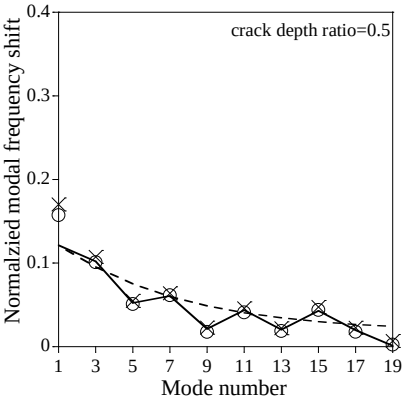
(b) crack depth ratio 0.5 for axial



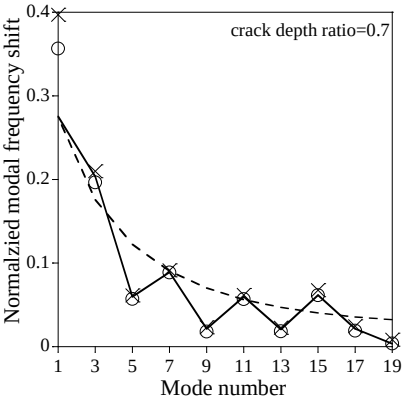
(c) crack depth ratio 0.7 for axial



(d) crack depth ratio 0.3 for bending



(e) crack depth ratio 0.5 for bending



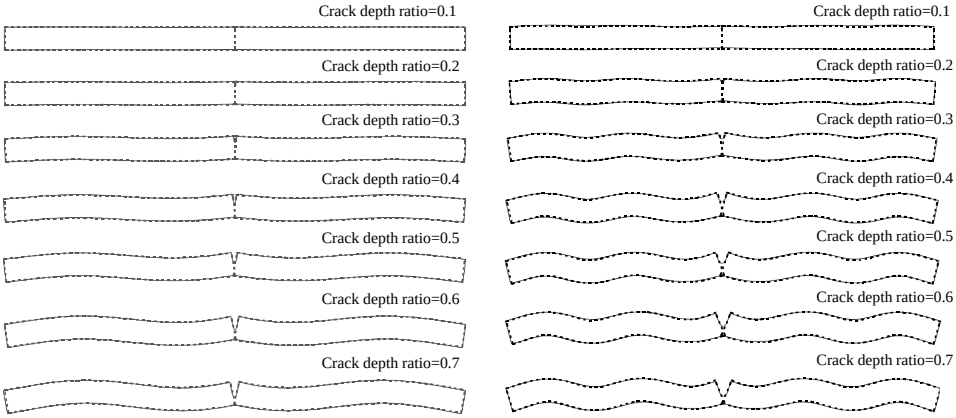
(f) crack depth ratio 0.7 for bending

Fig. 3.10 Normalized modal frequency shifts with respect to mode number for various crack depth ratios (——: proposed method, - - - -: conventional method, x: finite element analysis, o: experiment).

the fractional reduction in the axial modal frequencies to cracks has not yet been reported to the best of the authors' knowledge.

Fig. 3.11 shows a comparison of the mode shape of odd-numbered axial modes from the first to the seventh axial mode for the crack depth ratio between the proposed method and the finite element analysis. Solid and dotted lines represent the mode shapes of the finite element analysis and the proposed method, respectively. Once the modal frequencies have been computed using Eq. (3.34), the two-dimensional mode shape vectors on the neutral axis of the beam are obtained at the left and right sides of the crack from Eq. (3.3). The two-dimensional mode-shape vectors are then calculated at the feature edge of the beam by combining the kinematics of the Timoshenko beam theory and the elementary rod theory. The mode shape vectors are multiplied by an appropriate scaling factor to improve the readability of the mode shape. Finally, the scaled mode-shape vectors are superimposed on the original beam shape, as shown in Fig. 3.11. The proposed method accurately predicts the evolution of mode shapes for the crack depth ratio in comparison with the results of finite element analysis. When the crack depth ratio is smaller than 0.1, axial motion is dominant in the mode shape. When the crack depth ratio is 0.2, bending motion begins to occur in the mode shape at a very low level. With a crack depth ratio greater than 0.4, dominant bending motion appears in all axial mode shapes. The effects of ABMC are clear in the evolution of the bending motion in all axial modes for the crack depth ratio. In addition, as mentioned in Section 2.6, the effect of ABMC increases with increasing crack depth ratio, but the

effect of the mode II crack does not appear at all with increasing crack depth. It is obvious that the frequency equation without ABMC cannot describe the coupled axial-bending mode shape shown in Fig. 3.11.



(a) 1st axial mode (b) 3rd axial mode

(c) 5th axial mode (d) 7th axial mode

Fig. 3.11 Evolution of ABMC in odd-numbered axial mode shapes with respect to crack depth ratio (- - - : proposed method, ——: conventional method).

Chapter 4
Beam with a Crack in the Bending Node

It is commonly assumed that the presence of transverse cracks at the bending nodes of a beam does not reduce the bending modal frequency [Wan12, Tsa96, Mon90, Mas98, Dah17]. Das and Yilmaz [Das18] performed an experimental modal analysis of a curved composite beam and attributed the lack of frequency reduction to the proximity of the nodal points. Viola et al. [Vio07] and Satpute et al. [Sat17] imply that if the bending node is located in the center of the crack, the frequency of the cracked beam should be identical to that of the intact beam. A case against this assumption is presented in Section 2.6.4. The proposed analytical model demonstrated the frequency reduction due to mode II crack when the crack is located at the bending node, and this was visually confirmed by mode shape analysis. In Chapter 4, we aim to delve deeper into this phenomenon by deriving a closed frequency equation that considers the mode II crack, using the analytical model presented in Chapter 2 to provide a more comprehensive analysis.

4.1 Cracked Beam Modeling Considering Mode II Crack

4.1.1 Compatibility Equation of the Crack

When considering only the effects of the mode II crack and assuming the absence of influence from the mode I crack, the behavior of the crack can be simulated by setting F_{aa}, F_{bb}, F_{ab} and F_{ba} to zero in the compatibility equation of Eq. (1.2),

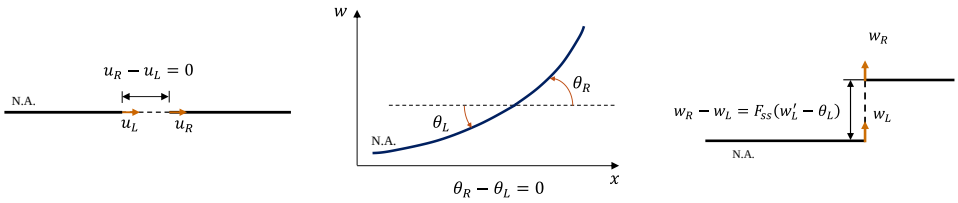
as validated in Section 2.6.4.

The three compatibility equations should be satisfied, as shown in Fig. 4.1.

$$u_R - u_L = 0 \tag{4.1a}$$

$$\theta_R - \theta_L = 0 \tag{4.1b}$$

$$w_R - w_L = F_{ss}(w_L' - \theta_L) \tag{4.1c}$$



(a) axial displacement (b) rotational angle (c) transverse displacement

Fig. 4.1 Compatibility equations at the crack in case considering mode II crack.

4.1.2 Spectral Solution

This chapter applies the analytical model from Chapter 2 under the condition that the crack is located at the bending node. In Section 4.1.1, because mode I crack is not considered, the axial and bending modes act independently. Therefore, by employing only the spectral solution for the bending mode, it is possible to simulate the crack behavior caused by the mode II crack.

Based on the Timoshenko beam theory, the spectral solution for the transverse displacement and rotation angle of the beam is divided into two parts corresponding to the left and right sides of the crack [Mei05].

$$w_L(x_1) = A_1 e^{-ik_p(a-x_1)} + A_2 e^{-ik_p x_1} + A_3 e^{-k_e(a-x_1)} + A_4 e^{-k_e x_1} \tag{4.2a}$$

$$w_R(x_2) = B_1 e^{-ik_p x_2} + B_2 e^{-ik_p(b-x_2)} + B_3 e^{-k_e x_2} + B_4 e^{-k_e(b-x_2)} \tag{4.2b}$$

$$\theta_L(x_1) = -iPA_1e^{-ik_p(a-x_1)} + iPA_2e^{-ik_px_1} - NA_3e^{-k_e(a-x_1)} + NA_4e^{-x_1} \quad (4.2c)$$

$$\theta_R(x_2) = -iPB_1e^{-ik_px_2} + iPB_2e^{-ik_p(b-x_2)} - NB_3e^{-k_ex_2} + NB_4e^{-k_e(b-x_2)} \quad (4.2d)$$

4.1.3 Dynamic Behaviors

Eq. (4.2) contains eight unknowns from the bending mode, as shown in Fig. 4.2. Fig. 4.2 shows the dynamic behavior of a cracked beam used to develop a frequency equation. Similar to the dynamic behavior observed in Section 3.1.3, all incident evanescent bending wave motions to either the crack or the support of the beam are assumed to be negligible. For example, as soon as an evanescent bending motion (A_3) is created at support A, it decays exponentially as it departs from A and vanishes at the left side of the crack (i.e., $A_3e^{-k_ea} \approx 0$). The same applies to the other evanescent bending wave motions A_4, B_3, and B_4, and their respective

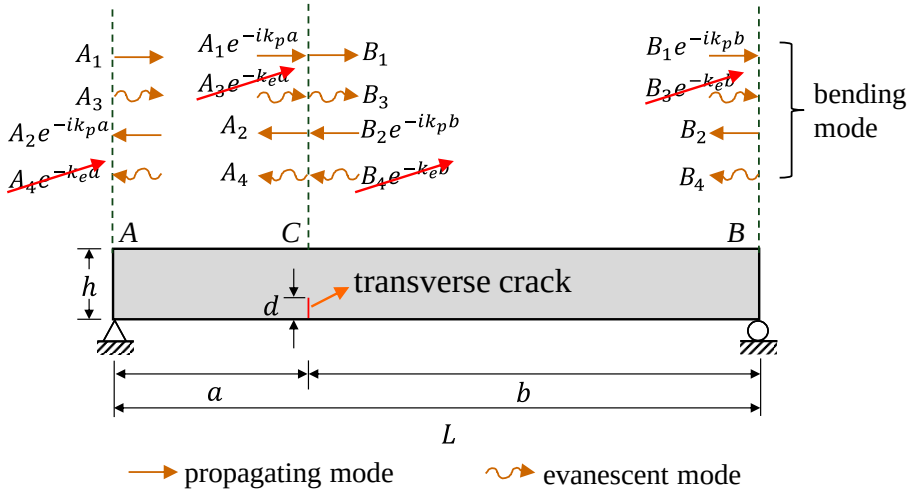


Fig. 4.2 The dynamic behaviors of a cracked beam by omitting all incident evanescent wave motions that are assumed to be negligible.

counterparts $A_4e^{-k_ea}$, $B_3e^{-k_eb}$, and $B_4e^{-k_eb}$. Therefore, the four evanescent bending wave motions corresponding to $A_4e^{-k_ea}$ at support A, $A_3e^{-k_ea}$ at the left side of the crack, $B_4e^{-k_eb}$ at the right side of the crack, and $B_3e^{-k_eb}$ at support B are not considered in formulating the frequency equation described below in the next section.

4.2 Derivation of the Closed Form Frequency Equation

The frequency equation can be determined using eight equations corresponding to the eight unknowns. The eight equations can be derived from two compatibility conditions at the crack, as given in Eqs. (4.1b) and (4.1c), two equilibrium equations, and boundary conditions at each support. The boundary condition at the supports is assumed to be that of a simply supported beam, which is commonly employed for simplicity of modeling, as shown in Fig. 2.1.

4.2.1 Eight Equations for Eight Unknowns

(i) Compatibility of transverse displacement at C

$$w_R - w_L = F_{ss}(w_L' - \theta_L)$$
$$\Rightarrow \{1 - i(k_p - P)F_{ss}\}A_1e^{-ik_pa} + \{1 + i(k_p - P)F_{ss}\}A_2 + \{1 + (k_e - N)F_{ss}\}A_4 - B_1 - B_2e^{-ik_pb} - B_3 = 0 \quad (4.3)$$

(ii) Compatibility of rotational angle at C

$$\theta_R - \theta_L = 0$$
$$\Rightarrow iPA_1e^{-ik_pa} - iPA_2 - NA_4 - iPB_1 + iPB_2e^{-ik_pb} - NB_3 = 0 \quad (4.4)$$

(iii) Shear force equilibrium at *C*

$$\kappa GA(-w_L' + \theta_L + w_R' - \theta_R) = 0$$

$$\begin{aligned} \Rightarrow -i\big(P - k_p\big)A_1 e^{-ik_p a} + i\big(P - k_p\big)A_2 - (k_e - N)A_3 \\ + i\big(P - k_p\big)B_1 - i\big(P - k_p\big)B_2 e^{-ik_p b} - (k_e - N)B_3 \\ = 0 \end{aligned} \tag{4.5}$$

(iv) Moment equilibrium at *C*

$$EI\theta_L' = EI\theta_R'$$

$$\begin{aligned} \Rightarrow k_p P A_1 e^{-ik_p a} + k_p P A_2 - k_e N A_4 - k_p P B_1 - k_p P B_2 e^{-ik_p b} \\ + k_e N B_3 = 0 \end{aligned} \tag{4.6}$$

(v) Transverse displacement boundary condition at *A*

$$\begin{aligned} w_L = 0 \\ \Rightarrow A_1 + A_2 e^{-ik_p a} + A_3 = 0 \end{aligned} \tag{4.7}$$

(vi) Moment boundary condition at *A*

$$\begin{aligned} EI\theta_L' = 0 \\ \Rightarrow -k_p P A_1 - k_p P A_2 e^{-ik_p a} + k_e N A_3 = 0 \end{aligned} \tag{4.8}$$

(vii) Transverse displacement boundary condition at *B*

$$\begin{aligned} w_R = 0 \\ \Rightarrow B_1 e^{-ik_p b} + B_2 + B_4 = 0 \end{aligned} \tag{4.9}$$

(viii) Moment boundary condition at *B*

$$\begin{aligned} EI\theta_R' = 0 \\ \Rightarrow -k_p P B_1 e^{-ik_p b} - k_p P B_2 + k_e N B_4 = 0 \end{aligned} \tag{4.10}$$

4.2.2 Process of Eliminating Unknowns

Adding $k_pP\times$ Eq. (4.7) to Eq. (4.8) results in:

$$A_3 = 0 \tag{4.11}$$

Adding $k_pP\times$ Eq. (4.9) to Eq. (4.10) produces:

$$B_4 = 0 \tag{4.12}$$

Substituting Eq. (4.11) into Eq. (4.7) yields:

$$A_2 = -A_1 e^{ik_p a} \tag{4.13}$$

Substituting Eq. (4.12) into Eq. (4.9) gives:

$$B_2 = -B_1 e^{-ik_p b} \tag{4.14}$$

Adding $-k_pP\times$ Eq. (4.3) and Eq. (4.13) to Eq. (4.6) produces:

$$\begin{aligned} B_3 = -i\frac{\gamma_q^2\left(1-\gamma_q^2\right)}{\left(1+\gamma_e^2\right)}k_pF_{ss}\left(1+e^{2ik_pa}\right)A_1e^{-ik_pa} \\ +\left\{1-\frac{\left(1-\gamma_q^2\right)\gamma_q^2}{\left(1+\gamma_e^2\right)\gamma_e}k_pF_{ss}\right\}A_4 \end{aligned} \tag{4.15}$$

Substituting Eqs. (4.13) to (4.15) into Eq. (4.5) results in:

$$\begin{aligned} A_4 = -i\frac{\left\{\left(1+\gamma_e^2\right)\gamma_e-\gamma_q^2\left(1-\gamma_q^2\right)k_pF_{ss}\right\}\gamma_e}{\left\{2\left(1+\gamma_e^2\right)\gamma_e-\left(1-\gamma_q^2\right)\gamma_q^2k_pF_{ss}\right\}}\left(1-\bar{t}_L\right)A_1e^{-ik_pa} \\ +i\frac{\left(1+\gamma_e^2\right)\gamma_e^2}{\left\{2\left(1+\gamma_e^2\right)\gamma_e-\left(1-\gamma_q^2\right)\gamma_q^2k_pF_{ss}\right\}}\left(1-\bar{t}_R\right)B_1 \end{aligned} \tag{4.16}$$

where $\bar{t}_L = -e^{2ik_pa}$, $\bar{t}_R = -e^{-2ik_pb}$

Substituting Eqs. (4.13) through (4.16) into Eq. (4.4) gives:

$$\left(1-\bar{t}_L\right)A_1e^{-ik_pa} = \left(1-\bar{t}_R\right)B_1 \tag{4.17}$$

Substituting Eqs. (4.13)–(4.16) into Eq. (4.3) yields:

$$\begin{aligned}&\left[2(1+\gamma_e^2)\gamma_e(1+\bar{t}_L)\right.\\&\qquad-\left\{\left(1-\gamma_q^2\right)(1+\bar{t}_L)\right.\\&\qquad\left.+i\gamma_e\left(\gamma_e^2+\gamma_q^2\right)(1-\bar{t}_L)\right\}k_p\gamma_q^2F_{ss}\left]A_1e^{-ik_pa}\right.\\&\qquad=\left[2(1+\gamma_e^2)\gamma_e(1+\bar{t}_R)\right.\\&\qquad-\left\{\left(1-\gamma_q^2\right)(1+\bar{t}_R)\right.\\&\qquad\left.-i\gamma_e\left(\gamma_e^2+\gamma_q^2\right)(1-\bar{t}_R)\right\}k_p\gamma_q^2F_{ss}\left]B_1\right.\end{aligned} \tag{4.18}$$

Substituting Eq. (4.17) into Eq. (4.18) produces a closed form frequency equation.

$$\begin{aligned}&(\bar{t}_L-\bar{t}_R)\\&-\frac{\left\{2\left(1-\gamma_q^2\right)(\bar{t}_L-\bar{t}_R)+2i\gamma_e\left(\gamma_e^2+\gamma_q^2\right)(1-\bar{t}_L)(1-\bar{t}_R)\right\}\gamma_q^2k_pF_{ss}}{4(1+\gamma_e^2)\gamma_e}\\&=0\end{aligned} \tag{4.19}$$

4.3 Extending the Frequency Equation to Other Support Conditions

As discussed in Section 3.4, Eq. (4.19) can be used as a frequency equation that can be applied to any arbitrary support condition. These conditions are parameterized by $\bar{t}_L$ and $\bar{t}_R$ for wave numbers and phase shifts at the support, accounting for wave reflection occurring at the beam support [Par17].

$$\bar{t}_L=\bar{\beta}_Le^{2ik_pa} \tag{4.20a}$$

$$\bar{t}_R=\bar{\beta}_Re^{-2ik_pb} \tag{4.20b}$$

where $\bar{\beta}_L$ and $\bar{\beta}_R$ depend on the type of support condition as described in Table 4.1 are the same as $\bar{\beta}_L$ and $\bar{\beta}_R$ in Table 3.1.

Table 4.1 Phase shift at the left and the right end of a beam according to support conditions

Support position \ Support conditions	hinge-roller (simply supported)	fixed-free (cantilever)	fixed-roller (propped cantilever)
Left end*	$\bar{\beta}_L = -1$ $\bar{\phi}_L = -\pi$	$\bar{\beta}_L = \bar{\beta}_{fix}$ *** $\bar{\phi}_L = \arg[\bar{\beta}_{fix}]$	$\bar{\beta}_L = \bar{\beta}_{fix}$ $\bar{\phi}_L = \arg[\bar{\beta}_{fix}]$
Right end**	$\bar{\beta}_R = -1$ $\bar{\phi}_R = \pi$	$\bar{\beta}_R = \bar{\beta}_{free}$ *** $\bar{\phi}_R = \arg[\bar{\beta}_{free}]$	$\bar{\beta}_R = -1$ $\bar{\phi}_R = \pi$
Support position \ Support conditions	fixed-fixed (both fixed)	hinge-free	free–free
Left end*	$\bar{\beta}_L = \bar{\beta}_{fix}$ $\bar{\phi}_L = \arg[\bar{\beta}_{fix}]$	$\bar{\beta}_L = -1$ $\bar{\phi}_L = -\pi$	$\bar{\beta}_L = \frac{1}{\bar{\beta}_{free}}$ $\bar{\phi}_L = \arg[\frac{1}{\bar{\beta}_{free}}]$
Right end**	$\bar{\beta}_R = \frac{1}{\bar{\beta}_{fix}}$ $\bar{\phi}_R = \arg[\frac{1}{\bar{\beta}_{fix}}]$	$\bar{\beta}_R = \bar{\beta}_{free}$ $\bar{\phi}_R = \arg[\bar{\beta}_{free}]$	$\bar{\beta}_R = \bar{\beta}_{free}$ $\bar{\phi}_R = \arg[\bar{\beta}_{free}]$

* $\bar{\beta}_L = e^{i\bar{\phi}_L}$

** $\bar{\beta}_R = e^{i\bar{\phi}_R}$

*** $\bar{\beta}_{fix} = \frac{P+iN}{P-iN}$, $\bar{\beta}_{free} = -\frac{P+i\gamma_e^2 N}{P-i\gamma_e^2 N}$

4.4 Approximate Solution

4.4.1 Derivation Process of the Approximate Solution

The *n*th modal frequency ω_{II} satisfying Eq. (4.19) is expressed by using the Taylor expansion for the local flexibility F_{ss} associated with mode II crack:

$$\omega_{II} = \widehat{\omega} + \Delta\omega_{II} = \widehat{\omega} + \left.\frac{d\omega}{dF_{ss}}\right|_{\omega=\hat{k}_p, F_{ss}=0} F_{ss} + \text{H. 0. T.} \tag{4.21}$$

where $\widehat{\omega}$ denotes the *n*th modal frequency of an intact beam satisfying Eq. (4.19) with $F_{ss} = 0$. The higher-order terms in Eq. (4.21) are negligible when F_{ss} is sufficiently small. Eq. (4.21) is approximated as follows by applying the chain rule between ω and k_p:

$$\omega_{II} \approx \widehat{\omega} + \left.\frac{d\omega}{dk_p}\frac{dk_p}{dF_{ss}}\right|_{k_p=\hat{k}_p, F_{ss}=0} F_{ss} \tag{4.22}$$

where $\widehat{\ }$ denotes a variable in which $\omega = \widehat{\omega}$ hereinafter.

$\left.\frac{dk_p}{dF_{ss}}\right|_{k_p=\hat{k}_p, F_{ss}=0}$ in Eq. (4.22) is obtained by differentiating Eq. (4.19) with respect to F_{ss}. The process of differentiating Eq. (4.19) with respect to F_{ss} is detailed in Appendix (A6).

$$\left.\frac{dk_p}{dF_{ss}}\right|_{k_p=\hat{k}_p, F_{ss}=0} = \frac{\hat{\gamma}_q^2\left[\left(1-\hat{\gamma}_q^2\right)(\hat{t}_L-\hat{t}_R) + i\hat{\gamma}_e\left(\hat{\gamma}_e^2+\hat{\gamma}_q^2\right)(1-\hat{t}_L-\hat{t}_R+\hat{t}_R\hat{t}_L)\right]}{4i(1+\hat{\gamma}_e^2)(1+\hat{\zeta})\hat{t}_L\hat{\gamma}_e}\frac{\hat{k}_p}{L} \tag{4.23}$$

where $\hat{\zeta} = \frac{1}{2iL}\left(\frac{\partial\beta_L}{\beta_L\partial k_p} - \frac{\partial\beta_R}{\beta_R\partial k_p}\right)\Big|_{k_p=\hat{k}_p}$.

Because $\hat{t}_L = \hat{t}_R$ to satisfy Eq. (4.19) with $F_{ss} = 0$, Eq. (4.23) can be simply expressed as:

$$\left.\frac{dk_p}{dF_{ss}}\right|_{k_p=\hat{k}_p, F_{ss}=0} = -\frac{\hat{\gamma}_q^2\left(\hat{\gamma}_e^2+\hat{\gamma}_q^2\right)}{4(1+\hat{\gamma}_e^2)(1+\hat{\zeta})}\left(2-\frac{1}{\hat{t}_L}-\hat{t}_R\right)\frac{\hat{k}_p}{L} \tag{4.24}$$

Substituting $\beta_L = e^{i\phi_L}$ from Eq. (4.20) into Eq. (4.24) produces:

$$\left.\frac{dk_p}{dF_{ss}}\right|_{k_p=\hat{k}_p, F_{ss}=0} = -\frac{\hat{\gamma}_q^2\left(\hat{\gamma}_e^2+\hat{\gamma}_q^2\right)}{(1+\hat{\gamma}_e^2)(1+\hat{\zeta})}\left\{1-\cos^2\left(\hat{k}_p a+\frac{\hat{\phi}_L}{2}\right)\right\}\frac{\hat{k}_p}{L} \tag{4.25}$$

Note that $(2-\frac{1}{\hat{t}_L}-\hat{t}_R)$ in Eq. (4.24) becomes $4\left\{1-\cos^2\left(\hat{k}_p a+\frac{\hat{\phi}_L}{2}\right)\right\}$ because $\frac{1}{\hat{t}_L} = \cos\left(2\hat{k}_p a+\hat{\phi}_L\right) - i\sin\left(2\hat{k}_p a+\hat{\phi}_L\right)$ and $\hat{t}_R = \cos\left(2\hat{k}_p b-\bar{\phi}_R\right) - i\sin\left(2\hat{k}_p b-\bar{\phi}_R\right) = \cos\left(2\hat{k}_p a+\hat{\phi}_L\right) + i\sin\left(2\hat{k}_p a+\hat{\phi}_L\right)$ for $\hat{t}_L = \hat{t}_R$.

Substituting Eq. (4.25) into Eq. (4.22) results in:

$$\omega_{II} = \hat{\omega} - \left.\frac{d\omega}{dk_p}\right|_{k_p=\hat{k}_p}\frac{\hat{\gamma}_q^2\left(\hat{\gamma}_e^2+\hat{\gamma}_q^2\right)}{(1+\hat{\gamma}_e^2)(1+\hat{\zeta})}\left\{1-\cos^2\left(\hat{k}_p a+\frac{\hat{\phi}_L}{2}\right)\right\}\hat{k}_p\frac{F_{ss}}{L} \tag{4.26}$$

Finally, Eq. (4.26) is converted in terms of the normalized modal frequency shifts (NMFS) $\hat{\xi}_{II}$ which denotes the fractional reduction of modal frequency due to the effect of mode II crack:

$$\hat{\xi}_{II} = \frac{\hat{\omega}-\omega_{II}}{\hat{\omega}} = \frac{\hat{\gamma}_q^2\left(\hat{\gamma}_e^2+\hat{\gamma}_q^2\right)}{(1+\hat{\gamma}_e^2)(1+\hat{\zeta})}\frac{\hat{\varphi}}{\hat{v}}\left\{1-\cos^2\left(\hat{k}_p a+\frac{\hat{\phi}_L}{2}\right)\right\}\frac{F_{ss}}{L} \tag{4.27}$$

where $\hat{v} = \frac{\omega}{\hat{k}_p}$ and $\hat{\varphi} = \frac{d\hat{\omega}}{d\hat{k}_p}$ representing the phase and group velocity of an intact beam, respectively.

4.4.2 Approximate Solution Considering Mode II crack

Because Eq. (4.19) is a nonlinear frequency equation for the angular frequency ω, the approximate solution to Eq. (4.19) is derived and expressed as the NMFS $\hat{\xi}_{II}$ to investigate the effect of the mode II crack on the fractional reduction of the modal frequency of the *n*th bending mode.

Eq. (4.27) can be rewritten in the following expression:

$$\hat{\xi}_{II} = \hat{\psi}_{II}\left\{1 - \cos^2\left(\hat{k}_p a + \frac{\hat{\phi}_L}{2}\right)\right\}\frac{F_{ss}}{L} \tag{4.28}$$

where $\hat{\psi}_{II} = \frac{\hat{\gamma}_q^2(\hat{\gamma}_e^2+\hat{\gamma}_q^2)}{(1+\hat{\gamma}_e^2)(1+\tilde{\zeta})}\frac{\hat{\varphi}}{\hat{v}}$ will hereinafter be referred to as an NMFS-factor for the mode II crack. Eq. (4.28) implies that the effect of the mode II crack on the fractional reduction of the *n*th modal frequency is determined by $\hat{\psi}_{II}$ and $\cos^2(\hat{k}_p a + \frac{\hat{\phi}_L}{2})$, which corresponds to the square of the modal curvature of the intact beam at the crack location [Par17]. When a crack is located on the node of the *n*th bending mode, the corresponding modal curvature of the intact beam at the crack location is zero. In this case, Eq. (4.28) can be simply expressed as follows:

$$\hat{\xi}_{II} = \hat{\psi}_{II}\frac{F_{ss}}{L} \tag{4.29}$$

When a crack is located on the antinode of the *n*th bending mode, the NMFS $\bar{\xi}_{II}$ in Eq. (4.28) becomes zero because $\cos^2\left(\hat{k}_p a + \frac{\hat{\phi}_L}{2}\right) = 1$ for the bending antinode at which the modal curvature reaches a maximum. The NMFS in Eq. (4.28) clearly shows that the effect of a mode II crack occurs at the bending node, as shown in Eq. (2.2). Conversely, if the crack is located at the bending antinode, the effect of the

mode II crack is not observed.

Fig. 4.3 shows $\hat{\psi}_{II}$ as a function of the frequency normalized by the cut-off frequency for different support conditions. The different support conditions produce approximately identical results for $\hat{\psi}_{II}$. It should be noted that $\hat{\psi}_{II}$ is independent of the thickness and material properties of the beam. Because $\frac{1}{(1+\hat{\gamma}_e^2)(1+\hat{\zeta})}\frac{\hat{\varphi}}{\hat{\upsilon}}$ in $\hat{\psi}_{II}$ is approximately 1 within the range of frequencies of interest, $\bar{\psi}_{II}$ is simply approximated by $\tilde{\psi}_{II} = \gamma_q^2(\gamma_e^2 + \gamma_q^2)$ as shown in Fig. 4.3. The NMFS-factor increases with frequency, meaning that the NMFS associated with mode II crack increases as the corresponding modal frequency increases.

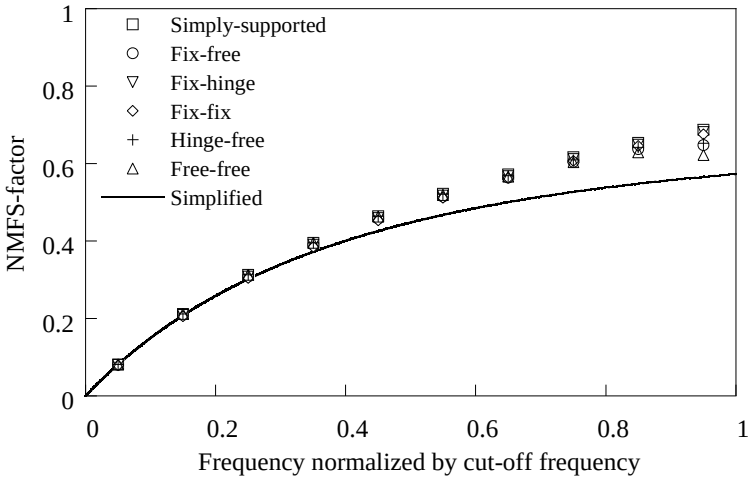


Fig. 4.3. NMFS-factor for different support conditions and the simplified NMFS-factor.

4.4.3 Comparison with Approximated Solution Considering Mode I Crack

For comparative purposes, the NMFS $\hat{\xi}_I$ for a frequency equation that considers the effect of the mode I crack on a cracked Timoshenko beam is introduced as

follows [Par18]:

$$\hat{\xi}_I = \hat{\psi}_I \cos^2(\hat{k}_p a + \frac{\hat{\phi}_L}{2}) \frac{F_{bb}}{L} \tag{4.30}$$

where $\hat{\psi}_I = \frac{(1-\hat{\gamma}_q^2)}{(1+\hat{\gamma}_e^2)(1+\hat{\zeta})} \frac{\hat{\varphi}}{\hat{v}}$ will hereinafter be referred to as an NMFS-factor for the mode I crack, while F_{bb} is the local flexibility coefficient associated with the mode I crack.

Similar to Eq. (4.28), Eq. (4.30) implies that the effect of the mode I crack on the fractional reduction of the *n*th modal frequency is determined by $\hat{\psi}_I$ and $\cos^2(\hat{k}_p a + \frac{\hat{\phi}_L}{2})$. However, when a crack is located on the nodal point of the *n*th bending mode, $\hat{\xi}_I$ becomes zero because the associated modal curvature is zero. An approximate solution can again explain why the bending antinodes in Table 2.2 are only affected by the mode I crack. When a crack is on the antinode of the *n*th bending mode, Eq. (4.29) can be simply expressed as follows because $\cos^2\left(\hat{k}_p a + \frac{\hat{\phi}_L}{2}\right) = 1$:

$$\hat{\xi}_I = \hat{\psi}_I \frac{F_{bb}}{L} \tag{4.31}$$

Furthermore, the NFMS-factor for mode I crack $\hat{\psi}_I$ can be simply approximated by $\tilde{\psi}_I = 1 - \gamma_q^2$ similar to $\hat{\psi}_{II}$, because $\frac{1}{(1+\hat{\gamma}_e^2)(1+\hat{\zeta})} \frac{\hat{\varphi}}{\hat{v}}$ in $\hat{\psi}_I$ is approximately 1 within the range of frequencies of interest regardless of the types of support conditions of a beam [Par18].

Fig. 4.4 shows a comparison of the simplified NMFS-factors for the mode II crack ($\tilde{\psi}_{II}$) and the mode I crack ($\tilde{\psi}_I$) as a function of frequency normalized by the cut-off

frequency. The first important implication that can be drawn from Fig. 4.4 is that the NMFS-factor for mode II crack $\tilde{\psi}_{II}$ is increasing with the frequency. This means that the associated NMFS also increases while the NMFS-factor for the mode I crack $\tilde{\psi}_{I}$ is decreasing as a function of frequency; thus, the associated NMFS decreases as well. The declining trend of $\tilde{\psi}_{I}$ as a function of frequency has been reported by Park and Lim [Par18], which is contradictory to the premise of structural health monitoring (SHM) for the fractional reduction of bending modal frequency. However, the increasing trend of $\tilde{\psi}_{II}$ as a function of frequency is fully consistent with the premise of SHM, in contrast to the declining trend of $\tilde{\psi}_{I}$. To the authors' knowledge, this has not been reported before. The second implication that can be drawn from Eqs. (4.28) and (4.30) is that for a real structure in which a crack is arbitrarily located on a beam, Eqs. (4.28) and (4.30) provide the upper limits of the NMFS. This means that the equations provide the maximum sensitivity of the NMFS to the crack expressed by Eqs. (4.29) and (4.31), which can account for the contributions of modes II and I crack, respectively. The intriguing point is that the NMFS due to the mode II crack approaches the upper limit in Eq. (4.29), whereas the NMFS due to the mode I crack approaches zero as the location crack approaches the bending node of an intact beam. In contrast, the NMFS due to the mode II crack approaches zero, whereas while the NMFS due to the mode I crack approaches the upper limit in Eq. (4.31) as the location of the crack approaches the bending antinode of an intact beam.

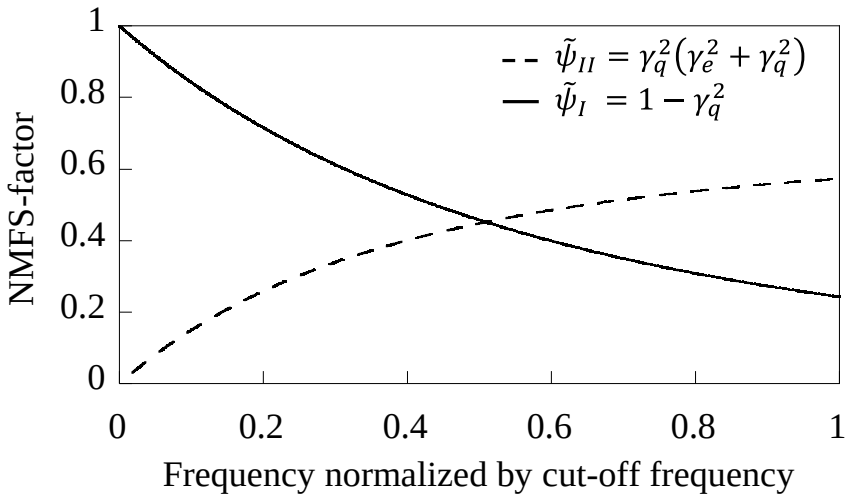


Fig. 4.4 Comparison of simplified NMFS-factors for mode II crack ($\tilde{\psi}_{II}$) and mode I crack ($\tilde{\psi}_I$) as a function of frequency normalized by the cut-off frequency.

4.5 Newton-Raphson Method for Solving a Nonlinear Equation

Since the closed-form frequency equation in Eq. (4.19) is nonlinear, the modal frequencies can be obtained using the Newton-Raphson (N-R) method, following the same procedure as in Section 3.5. Eq. (4.19) is defined as y, which is represented by:

$$y = (\bar{t}_L - \bar{t}_R) - \frac{\{2(1-\gamma_q^2)(\bar{t}_L - \bar{t}_R) + 2i\gamma_e(\gamma_e^2 + \gamma_q^2)(1-\bar{t}_L)(1-\bar{t}_R)\}\gamma_q^2 k_p F_{ss}}{4(1+\gamma_e^2)\gamma_e} \tag{4.32}$$

The iteration of Eqs. (2.44)-(2.46) is then conducted until convergence to 10^{-7} is obtained according to the criterion given in Eq. (2.47). The derivative $\frac{\partial y}{\partial \omega}$ used in Eq. (2.44) can be expressed by applying the chain rule.

$$\frac{\partial y}{\partial \omega} = \frac{\partial y}{\partial k_p}\frac{\partial k_p}{\partial \omega} \tag{4.33}$$

Since only k_p is used in the chain rule in the same way as in Section 3.5, k_p, k_e, P, N should all operate as correlated variables with respect to ω.

The derivative $\frac{\partial y}{\partial k_p}$ used in Eq. (4.33) is obtained by differentiating Eq. (4.32) with respect to k_p.

$$\begin{aligned}
\frac{\partial y}{\partial k_p} = {} & -4\gamma_e^2 \frac{\partial \gamma_e}{\partial k_p}(\bar{t}_L - \bar{t}_R) - 2(1+\gamma_e^2)\left(\frac{\partial \bar{t}_L}{\partial k_p} - \frac{\partial \bar{t}_R}{\partial k_p}\right)\gamma_e \\
& - 2(1+\gamma_e^2)(\bar{t}_L - \bar{t}_R)\frac{\partial \gamma_e}{\partial k_p} \\
& + \left[2\gamma_q \frac{\partial \gamma_q}{\partial k_p}\{(1-\gamma_q^2)(\bar{t}_L - \bar{t}_R)\right. \\
& + i\gamma_e(\gamma_e^2 + \gamma_q^2)(1-\bar{t}_L)(1-\bar{t}_R)\} \\
& + \gamma_q^2\left\{2\gamma_q \frac{\partial \gamma_q}{\partial k_p}(\bar{t}_L - \bar{t}_R) + (1-\gamma_q^2)\left(\frac{\partial \bar{t}_L}{\partial k_p} - \frac{\partial \bar{t}_R}{\partial k_p}\right)\right. \\
& + i\frac{\partial \gamma_e}{\partial k_p}(\gamma_e^2 + \gamma_q^2)(1-\bar{t}_L)(1-\bar{t}_R) \\
& + i\gamma_e\left(2\gamma_e \frac{\partial \gamma_e}{\partial k_p} + 2\gamma_q \frac{\partial \gamma_q}{\partial k_p}\right)(1-\bar{t}_L)(1-\bar{t}_R) \\
& - i\gamma_e(\gamma_e^2 + \gamma_q^2)\frac{\partial \bar{t}_L}{\partial k_p}(1-\bar{t}_R) \\
& \left.\left. - i\gamma_e(\gamma_e^2 + \gamma_q^2)(1-\bar{t}_L)\frac{\partial \bar{t}_R}{\partial k_p}\right\}\right] k_p F_{ss} \\
& + \gamma_q^2\left[(1-\gamma_q^2)(\bar{t}_L - \bar{t}_R)\right. \\
& \left. + i\gamma_e(\gamma_e^2 + \gamma_q^2)(1-\bar{t}_L)(1-\bar{t}_R)\right] F_{ss}
\end{aligned} \tag{4.34}$$

Where $\frac{\partial \gamma_e}{\partial k_p}$, $\frac{\partial \gamma_q}{\partial k_p}$, $\frac{\partial \bar{t}_L}{\partial k_p}$ and $\frac{\partial \bar{t}_R}{\partial k_p}$ are given by Eqs. (3.48a), (3.48b) and Table 3.2.

4.6 Validation

4.6.1 Numerical Example

The proposed frequency equation for a beam with a crack located at the bending node was verified by comparing the quantitative results with those from finite element analysis and experiment. The numerical examples used for validation employed the same free-free beam as illustrated in Fig. 3.6. The crack is located at the center of the beam, and the crack depth ratio varies from 0 to 0.7. The elastic modulus, Poisson's ratio, and density of the beam are 69 GPa, 0.34, and 2700 kg/m3, respectively. Due to the symmetry of the free-free beam, bending nodes are created at the center of the beam for even-numbered modes, whereas bending antinodes are generated at the center for odd-numbered modes. As described in Table 3.1, the contribution of the mode II crack becomes a maximum, whereas no contribution of the mode I crack exists that concerns the NMFS associated with even-numbered bending modes. Note that the opposite applies to the NMFS associated with odd-numbered bending modes, as explained in Chapter 3.

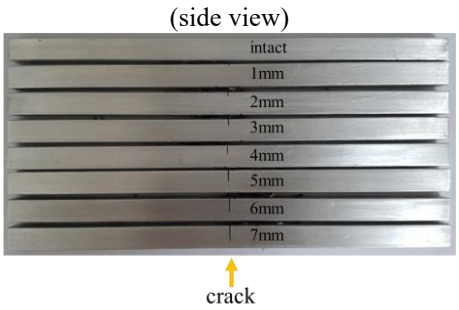
Similar to Section 3.4.1, the proposed method, which considers only the impact of the mode II crack, is suitable for numerical models of beams with an aspect ratio above 10. Since the influence of the mode II crack is proportional to the thickness of the beam, its effects are almost negligible in bending modes below the third order in shallow beams, where errors arise due to the impact of evanescent waves. The influence of the mode II crack also becomes more sensitive to frequency reduction

in higher modes. Consequently, the proposed method is expected to accurately predict the influence of mode II crack in higher modes where the effects of evanescent waves are not significant.

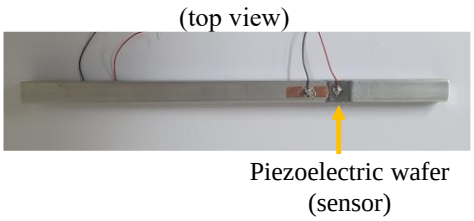
4.6.2 Experimental Setup

Fig. 4.5 shows the experimental setup used to verify the proposed frequency equation. Four groups of aluminum beams with various crack depth ratios were fabricated, as shown in Fig. 4.5. One group consists of one intact beam and seven beams with different crack depth ratios from 0.1 to 0.7. The crack at the bottom center of the beam was manufactured in the form of a 0.3 mm wide notch with depths ranging from 1 mm to 7 mm (Fig. 4.5(a)). Two piezoelectric wafers (Piezo Systems Inc. PSI-5A4E L 10 mm × T 0.191 mm × W 10 mm) were mounted on each beam to obtain the dynamic response using the pitch-catch method. A sensing piezoelectric wafer was mounted 43 mm away from the left end on the top of the beam (Fig. 4.5(b)), and an actuating piezoelectric wafer was mounted 50 mm away from the center crack on the bottom of the beam (Fig. 4.5(c)). The support-free conditions of the beam were realized by suspending the beams with two strings 10 mm in from each end of the beam (Fig. 4.5(d)). The effect of the string locations on the modal frequencies of the beams is negligible compared with the experimental uncertainties caused by manufacturing errors, temperature variations, and measurement noise. A chirp voltage input signal with a driving frequency ranging from 1 kHz to 130 kHz was applied to the actuating piezoelectric wafer using a 16-bit arbitrary waveform

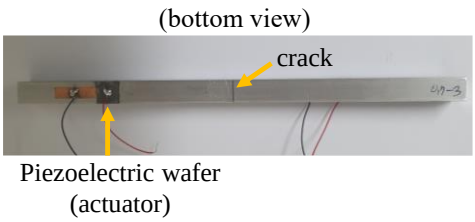
generator (NI PXI-5422). The duration and amplitude of the chirp voltage input signal were 1 s and 5 V, respectively. The corresponding output voltage signal was measured using a 14-bit high-speed digitizer (NI PXIe-5122). The sampling rate and frequency resolution were 5 MHz and 1 Hz, respectively. The measurement time corresponding to the frequency resolution was set to 1 s to allow sufficient time for



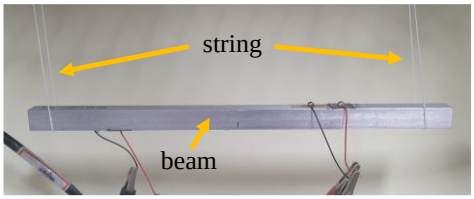
(a) group of eight aluminum beams with increasing crack depths



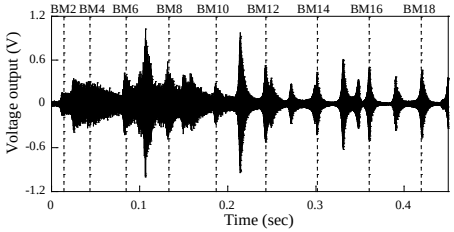
(b) sensing piezoelectric wafers mounted on the top of an aluminum beam



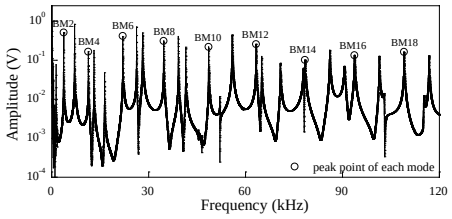
(c) actuating piezoelectric wafers mounted on the bottom of an aluminum beam



(d) beam suspended by two strings in a free–free support condition



(e) example of intact beam average output voltage signal



(f) frequency response spectrum of (e) and modal frequencies

Fig. 4.5 Experimental setup.

the dynamic behavior of the beam to decay. The experiment repeated 10 measurements automatically using LabVIEW™ software to obtain the measured average output voltage signal. An example of the average output voltage signal of the intact beam is shown in Fig. 4.5(e). The dotted line indicates the moment when the driving frequency of the input chirp signal becomes equal to the even-numbered mode frequency of the intact beam. The resonance phenomenon associated with the even-numbered mode frequencies from 1 kHz to 130 kHz is clearly shown in Fig. 4.5(e). The frequency response spectrum of the beam was calculated by Fast Fourier Transform using the input and output voltage signals. The peak frequency was extracted from the frequency response spectrum and compared with the modal frequency calculated using finite element analysis to identify the corresponding mode.

4.6.3 Finite Element Analysis Setup

Finite element analysis was performed using ABAQUS 6.14/standard software on the Nurion supercomputer located at the KISTI Supercomputing Center. The actual thickness and length of the four groups of aluminum beams were measured using a caliper with a resolution of 1/100 mm. The average thickness and length values used to obtain numerical results from the proposed method and finite element analysis were 10.25 mm and 197.94 mm, respectively. Note that this is the same specimen used in Section 3.6.3. A mesh layout (811,800 8-node secondary solid element L 50 μm × T 50 μm) was used for element discretization to accurately calculate the change

in modal frequency. The mechanical behavior of the crack was simulated by creating double nodes on the frictionless crack surface during finite element discretization [Par18]. The modal frequency was calculated for comparison with the finite element analysis in which the finite element associated with the notch region had been removed because the effect of mass reduction due to the notch can cause a significant change in the modal frequency of the cracked beam. The effect of mass reduction due to the notch on the calculated modal frequency was negligible compared with the experimental uncertainty [Par18]. For the finite element analysis, the increments of the different crack depth ratios were set to 0.05.

4.6.4 Free-Free Beam with a Crack at the Bending Node for an Aspect Ratio of 19.8

Table 4.2(a) shows the mean values of the modal frequencies of the four intact beams obtained through the experiment. There are nine even-numbered bending modes from the 2nd to the 18th bending mode. The modal frequencies associated with the odd-numbered bending modes have been omitted because no contribution from the mode II crack existed for the crack on the antinodes.

The consistency of the modal frequency for the experiment was confirmed by the standard deviation of the frequency of the experimental mode which was $\leq 0.5796\%$. Table 4.2(b) shows the mean fractional reduction values in the modal frequency of a cracked beam compared to that of an intact beam.

Table 4.2 Experimental results: (a) The mean values of experimental modal frequencies of intact beams (unit: kHz); (b) The mean fractional reduction values in the modal frequency of cracked beams compared to that of an intact beam (unit: %)

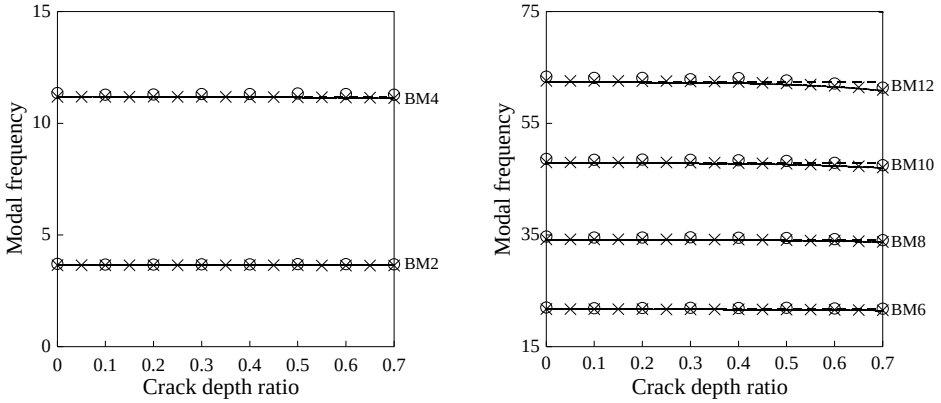
Crack depth ratio / Mode No.	Intact[(a)]	0.0907[(b)**]	0.189[(b)]	0.294[(b)]	0.393[(b)]	0.492[(b)]	0.590[(b)]	0.687[(b)]
BM2*	3.698	0.4597	0.3312	0.2501	0.3042	-0.05408	0.00676	0.08788
BM4	11.35	0.3966	0.2886	0.2313	0.3217	0.1256	0.2776	0.5552
BM6	22.01	0.2590	0.1079	0.1999	0.2510	0.1454	0.5748	0.7963
BM8	34.67	0.2740	0.1471	0.2243	0.4132	0.5466	1.090	1.630
BM10	48.65	0.3849	0.2662	0.3042	0.4918	0.7781	1.468	2.341
BM12	63.33	0.2996	0.2724	-0.1129	0.4070	0.9869	1.874	3.049
BM14	78.52	0.2719	0.1089	0.1984	0.4254	0.9794	2.236	3.880
BM16	93.87	0.3225	0.05646	0.1771	0.5963	1.160	2.336	4.518
BM18	109.2	-0.0490	-0.03045	0.2054	0.9652	1.660	3.399	5.375

* The first letter "BM" stands for bending and the following number represents the number of the corresponding mode.

** The ratio of the mean value of the measured crack depths to the average thickness (10.25 mm) is used to represent the crack depth ratio.

Fig. 4.6 shows the modal frequencies as a function of the crack depth ratio from the proposed frequency equation compared with those obtained from the finite element analysis and several different experiments. Note that the mean values of the modal frequencies from the four groups of aluminum beams are used in the comparison. The frequency range is from 0 to 120 kHz, including the first nine even-numbered bending modes of the beam. Solid lines denote the modal frequencies computed using the proposed frequency equation (Eq. (4.19)), while "x" and "o" represent the modal frequencies obtained from the finite element analysis and our

current experiment, respectively. Because Eq. (4.19) is nonlinear for the modal frequency, the N-R method was used to solve the equation. The increment for varying the crack depth ratio was set to be small enough to guarantee convergence of the N-R method. The initial guess of the N-R method was the modal frequency of an intact beam. Then, the solution for the current crack depth ratio became the initial guess for the next crack depth ratio, which was repeated until the required crack



(a) 0-15 kHz (b)15-75 kHz

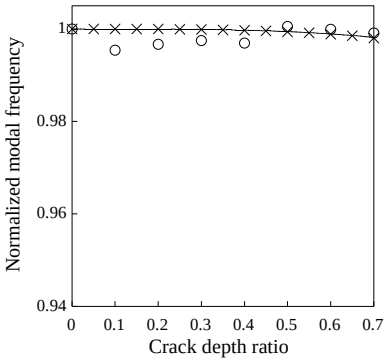
(c) 75-120 kHz

Fig. 4.6 Modal frequencies from the proposed frequency equation as a function of the crack depth ratio compared to those from finite element analysis and actual experiments. (——: proposed method, - - -: conventional method, x: finite element analysis, o: experiment).

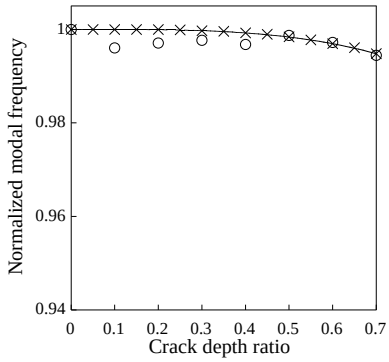
depth ratio was reached. The modal frequencies obtained from the proposed method were consistent with those obtained from the finite element method and our current experiment. The declining trend of the modal frequencies was clearly observed as both the mode number and the crack depth ratio increased. Note that the dotted lines in Fig. 4.6 represent the modal frequencies computed using the proposed method with $F_{ss} = 0$ in which only the mode I crack was considered. The same N-R method was used to solve the frequency equation because it is also nonlinear for the modal frequency. No declining trend in the modal frequencies was observed for the crack depth ratio throughout all bending modes. This implied that mode I crack did not affect the reduction in the modal frequencies of the beam regardless of the crack depth ratio when the crack was on a bending node. The mode II crack then needs to be considered to predict the modal frequency reduction properly.

Fig. 4.7 shows a comparison of the normalized modal frequencies for the even-numbered bending modes in Fig. 4.6, indicating more clearly the declining trend of the modal frequencies with increasing mode number and crack depth ratio. The normalized modal frequency (NMF) represents the modal frequency divided by that of an intact beam. The symbols used in Fig. 4.7 are identical to those in Fig. 4.6. The proposed method is consistent with finite element analysis for all bending modes. Although some discrepancies exist between the proposed method and the experimental results, particularly for incipient cracks in lower bending modes, consistency is observed in terms of the overall declining trend of the NMF with increasing mode number and crack depth ratio. While a similar decreasing trend is

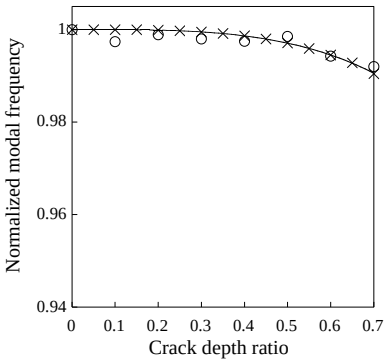
observed, it seems inappropriate to attribute the discrepancy to errors due to the size of the beam, since these errors exclusively occur at incipient cracks in experiments. The author also agrees that this discrepancy is unusual. In particular, in Chapter 2, no similar problems were found in the examples with deep beams. The observation of lower result in the experiment of shallow beams with incipient cracks warrants further investigation. The effects of the mode II crack on the NMF begin to appear when the crack depth ratio is approximately 0.4 for bending modes lower than the 6th and 0.3 for bending modes higher than the 8th. The effects of the mode II crack become more significant as both the mode number and the crack depth ratio increase, as described in Section 2.4.



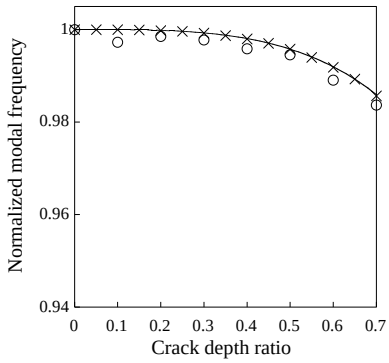
(a) 2nd bending mode



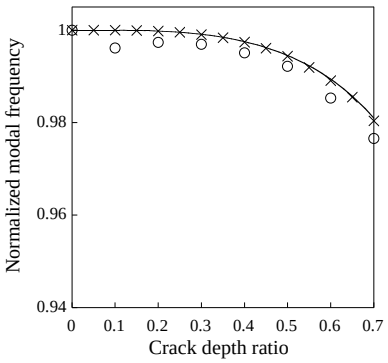
(b) 4th bending mode



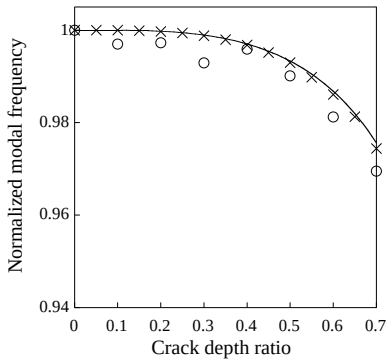
(c) 6th bending mode



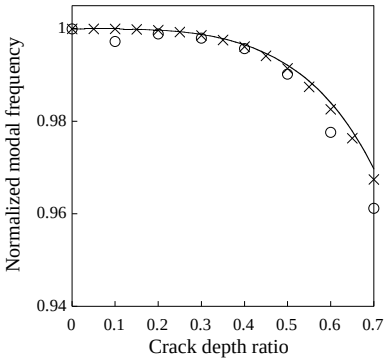
(d) 8th bending mode



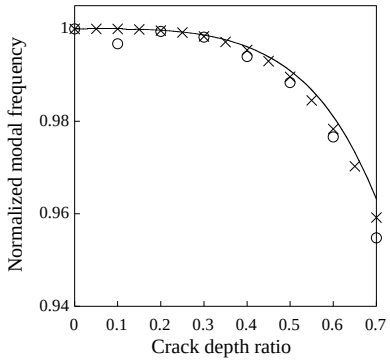
(e) 10th bending mode



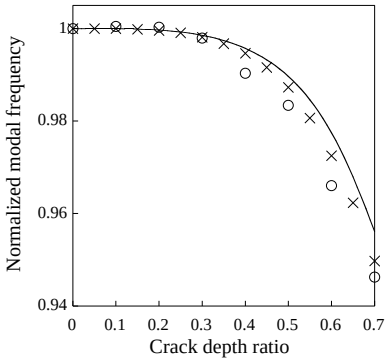
(f) 12th bending mode



(g) 14th bending mode



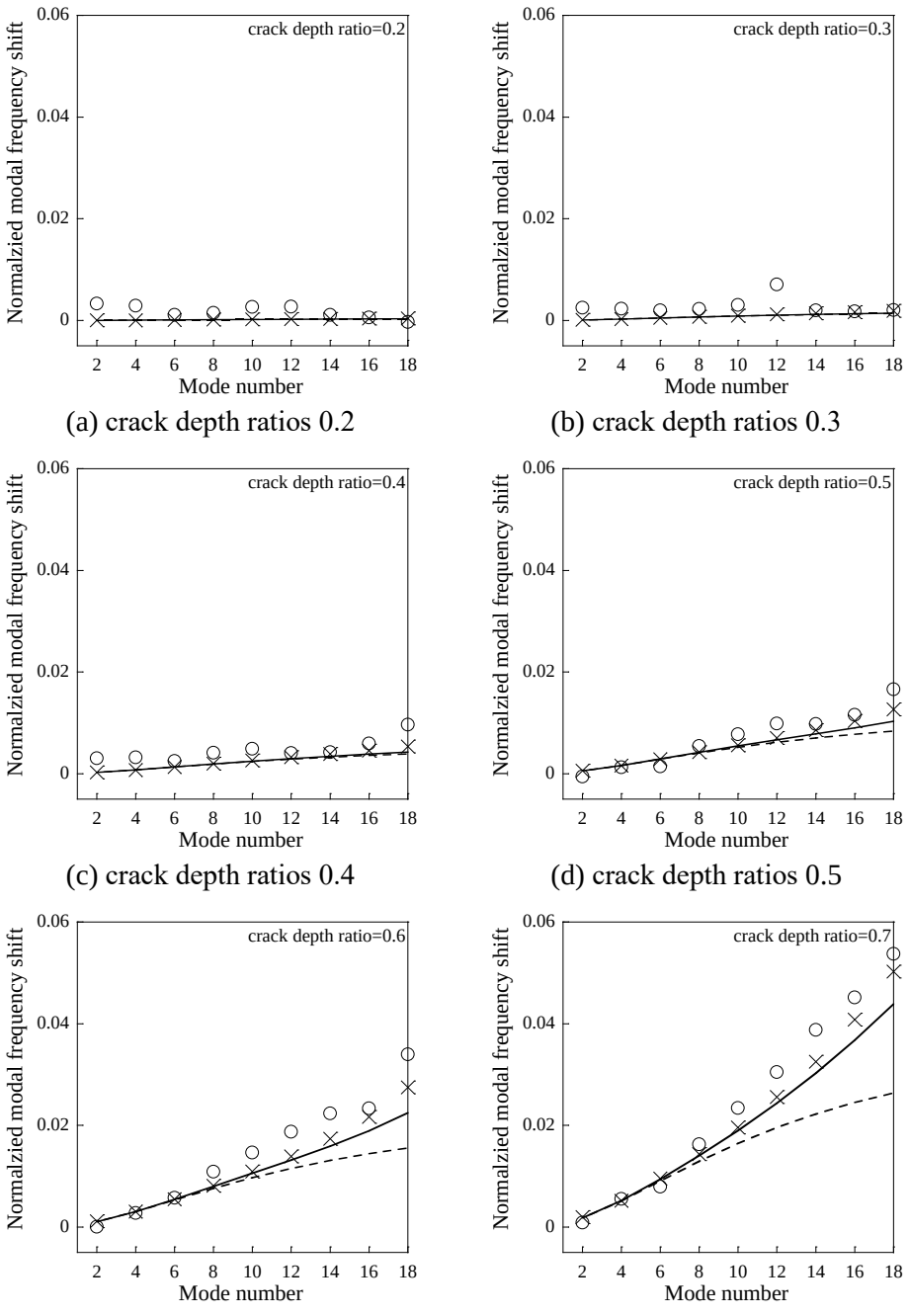
(h) 16th bending mode



(i) 18th bending mode

Fig. 4.7 Normalized modal frequencies as a function of crack depth ratios for different bending modes (——: proposed method, x: finite element analysis, o: experiment).

Fig. 4.8 shows the NMFS's as a function of the mode number for six crack depth ratios from 0.2 to 0.7. As in Fig. 4.7, the symbols used in Fig. 4.8 are identical to those used in Fig. 4.6. Note that the dotted line represents an approximate solution rather than the conventional method. The proposed method using Eq. (4.19) produces satisfactory results compared with those obtained from the finite element analysis and experiment. The NMFS values predicted by Eq. (4.27) are also shown in Fig. 4.8 because Eq. (4.27) produces an approximate solution to Eq. (4.19) as a function of the mode number for different crack depth ratios without the need for the N-R method. Eq. (4.27) yields satisfactory results compared to the experimental results when the crack depth ratio is ≤ 0.4. As the crack depth ratio becomes ≥ 0.5, the numerical results from Eq. (4.27) deviate from the experimental results due to the linear approximation in Eq. (4.21). Furthermore, it is clear that the theoretical implications drawn in Section 4.4 are strongly supported by the NMFSs in Fig. 4.8. The increasing trend of the NMFS as a function of the mode number for all crack depth ratios in Fig. 4.8 implies that the effect of the mode II crack on the fractional reduction of the modal frequency becomes more sensitive as the mode number increases, which is consistent with the SHM premise. Note that the sensitivity of the mode II crack to the fractional reduction in the modal frequency has been expressed by the simplified NMFS-factor for the mode II crack ($\tilde{\psi}_{II}$) in Section 4.4. In the past, a bending node was regarded as a blind zone for assessing cracks. However, this blind zone can be significantly reduced using the higher modal frequencies, as shown in Fig. 4.8.



(a) crack depth ratios 0.2 (b) crack depth ratios 0.3

(c) crack depth ratios 0.4 (d) crack depth ratios 0.5

(e) crack depth ratios 0.6 (f) crack depth ratios 0.7

Fig. 4.8 Normalized modal frequency shifts as a function of mode number for different crack depth ratios (——:proposed method, - - - : approximate solution, x: finite element analysis, o: experiment).

Fig. 4.9 shows a comparison of the bending mode shapes for the 4th, 10th, 14th, and 18th modes as a function of the crack depth ratio for the proposed method and the finite element analysis. The solid and dotted lines represent the mode shapes of the finite element analysis and the proposed method, respectively. Once the modal frequencies were calculated using Eq. (4.19), the two-dimensional mode shape vectors on the neutral axis of the beam were obtained at the left and right sides of a crack from Eq. (4.2), respectively. Two-dimensional mode shape vectors were then calculated at the feature edge of the beam by combining the kinematics of the Timoshenko beam theory. The mode shape vectors were magnified using a proper scaling factor for the readability of the mode shapes. The proposed method and the finite element analysis are consistent in the evolution of the mode shapes as a function of the crack depth ratio. As described in Section 2.1, a discontinuity of the neutral axis in the transverse direction occurs at crack locations because the mode II crack affects the bending mode shape in the vicinity of the crack. For the 4th mode, all bending mode shapes are practically identical to that of an intact beam because the effect of the mode II crack on the bending mode shape rarely appears throughout the range of crack depth ratios. The effect of the mode II crack begins to appear slightly in the 10th mode when the crack depth ratio is 0.7, becoming more evident in the 14th mode when the crack depth ratio is > 0.6. For the 18th mode, the evolution of mode II crack in the vicinity of a crack is clearly observed in the bending mode shapes when the crack depth ratio > 0.4. Note that the comparative result in Fig. 4.9 justifies the assumption that only the mode II crack influences the modal behavior

of the beam in the vicinity of a crack on a bending node.

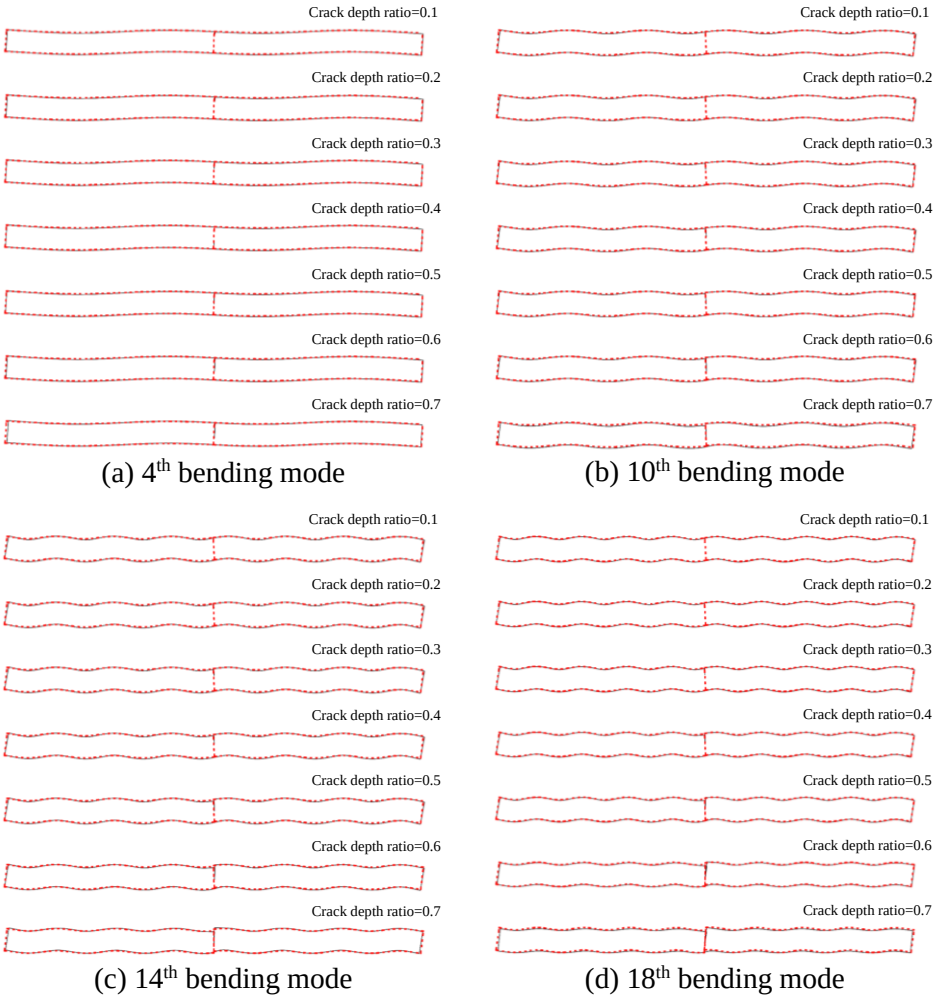


Fig. 4.9 Evolution of mode II crack in the vicinity of a crack in bending mode shapes as a function of the crack depth ratio for different bending modes (- - - : proposed method, ——: finite element analysis).

Chapter 5
Conclusion

This study has proposed a new analytical model capable of predicting the modal frequencies of two-dimensional beams with a transverse crack, regardless of the aspect ratio of the beam and crack location. The conventional method used by most researchers predicted the modal frequencies on the cracked beam by considering only the discontinuity of the rotational angles on either side of the crack. The conventional method produced errors in the prediction of modal frequencies, especially in beams with low aspect ratios and in the higher-numbered bending modes. This study has proposed a new analytical model capable of predicting the modal frequencies of two-dimensional beams with a transverse crack, regardless of the aspect ratio of the beam and crack location. The conventional method used by most researchers predicted the modal frequencies on the cracked beam by considering only the discontinuity of the rotational angles on either side of the crack. The conventional method produced errors in the prediction of modal frequencies, especially in beams with low aspect ratios and in the higher-numbered bending modes. Since accurate modal frequency prediction is essential for structural health monitoring, these errors limit the use of the equations of the conventional method.

In Chapter 2, a frequency equation was presented that accurately predicts the behavior of two-dimensional beams with a transverse crack. The proposed method incorporates three compatibility conditions along with five local flexibility

coefficients to account for the ABSMC at the crack. The ABSMC refers collectively to the axial-bending modal coupling (ABMC) caused by the mode I crack and the shear effects induced by the mode II crack. The three compatibility equations were derived from the constitutive equations at the crack site and the principles of linear elasticity theory. The proposed method for the beam was based on the derivation of spectral solutions from both the Timoshenko beam theory and the elementary rod theory. By considering rotational inertia and shear deformation, the proposed method is accessible for higher modes or cases with low aspect ratios. The proposed method was represented by a 12 x 12 characteristic matrix, and to ensure a non-trivial solution, the corresponding frequency equation was expressed such that the determinant of the characteristic matrix equals zero. Furthermore, the N-R method is employed to compute the modal frequencies because of the nonlinearity of the frequency equation with respect to the angular frequency.

The proposed method was validated through a comparison with finite element analysis and experimental results for cases where cracks were located at the center and 0.45 L away from the left end of a free-free beam, respectively. When the crack was located at the center of the beam, the contributions of modes I and II crack to the four types of vibration modes were elucidated following the compatibility conditions. When the crack is located at either the bending antinode or the bending node, the effects of modes I and II crack act independently without influencing each other. In cases where the crack was located 0.45 L from the beam, the evolution of the mode shapes allowed a clear observation of the contributions of both modes I

and II crack. In the first two bending modes or up to a crack depth of 0.3, the influence of the mode I crack was dominant. However, as the mode number increases, the influence of the mode II crack significantly increases and becomes comparable to that of the mode I crack. Finally, the proposed method has successfully predicted the influence of the ABSMC on cantilever deep beams with various crack locations through a comparison with finite element analysis.

In Chapter 3, the study presented a closed-form frequency equation for beams with a crack located at the bending antinodes. When a crack is located at the bending antinode, it is solely influenced by the mode I crack, eliminating the effects of the mode II crack. Since only the mode I crack was considered, the proposed method applied the compatibility equation from Chapter 2 by setting the local flexibility F_{ss}, corresponding to the mode II crack, to zero. In the higher modes, the evanescent waves generated by supports or cracks tended to decay before reaching other cracks or supports, thus allowing for the assumption that these evanescent waves could be neglected.

A numerical example where the crack is located at the bending antinode was used to validate the proposed method by comparing the results with those of finite element analysis and experimental data for crack depth ratios ranging from 0 to 0.7. The effects of ABMC were particularly significant concerning the crack depth ratio, notably when the axial and bending modes were adjacent to each other. Using a beam with an aspect ratio of 19.8, ABMC was observed for bending modes above the third order without the influence of evanescent waves. The ABMC found that the axial

and fifth order and above bending modes occur adjacent to each other, so the proposed method accurately predicts the modal frequencies regardless of the influence of evanescent waves.

In Chapter 4, a closed-form frequency equation was presented for beams with a crack located at the bending node. When a crack is located at the bending node, it is only affected by the mode II crack, which eliminates the effects of the mode I crack. Since only the mode II crack was considered, the proposed method applied the compatibility equation from Chapter 2 by setting the local flexibilities F_{aa}, F_{bb}, F_{ab}, F_{ba}, corresponding to the mode I crack, to zero. Similar to Chapter 3, evanescent waves occurring at cracks or supports were not considered.

This study identifies two crucial findings from a comparison between the proposed approximate solution for the mode II crack and the existing solution for the mode I crack. First, the influence of the mode II crack on the normalized modal frequency shifts (NMFS) is maximized at the bending nodes and minimized at the bending antinodes, in contrast to the mode I crack where the effects are reversed. Second, the sensitivity of mode II crack effects to NMFS increases with higher mode numbers, as shown analytically by the NMFS-factor for mode II crack. However, the sensitivity of mode I crack effects to NMFS decreases with the number of modes.

The proposed method was validated by comparing it with the results of finite element analysis and experiments. The proposed frequency equation satisfactorily predicted the fractional reduction of modal frequencies caused by a crack at a bending node compared to those of finite element analysis and experiments. The

NMFS for increasing mode number was observed to be sensitive for all crack depth ratios, as predicted by the NMFS factor for the mode II crack in the approximate solution. The effects of shear became more pronounced with increasing crack depth and mode number when observed through mode shapes. Considering only the occurrence of shear at the crack without crack opening, this justifies the assumption that only the mode II crack affects the modal behavior of the beam near a crack at a bending node, whereas the mode I crack has no effect. In addition, there were some discrepancies in the incipient cracks in the experimental results; however, it is difficult to attribute them to environmental factors, and further research is needed.

Appendices

1) Appendix (A1)

Displacements on either side of the crack can be represented as elastic strain energy using Castigliano's theorem, as follows [Dar04]:

$$u_i^L = \frac{\partial (U^0)^L}{\partial P_i^L} \tag{A1.1a}$$

$$u_i^R = \frac{\partial (U^0)^L}{\partial P_i^R} + \frac{\partial U^C}{\partial P_i^R} \tag{A1.1b}$$

where U^0 and U^C denote elastic strain energy of the intact and by the crack, respectively. u_i and P_i are displacement and force, respectively.

The displacement jump can be represented as follows using Eq. (A1.1).

$$u_i^R - u_i^L = \frac{\partial U^C}{\partial P_i} \tag{A1.2}$$

By substituting Eq. (A1.2) into Eq. (2.2), which is the constitutive equation of the crack as follows:

$$\frac{\partial U^C}{\partial P_i} = c_{ij} P_j \tag{A1.3}$$

where c_{ij} are the compliance coefficient.

The partial derivative for P_k is applied to both sides in Eq. (A1.3).

$$\frac{\partial}{\partial P_k}\left(\frac{\partial U^C}{\partial P_i}\right) = \frac{\partial}{\partial P_k}(c_{ij} P_j) \tag{A1.4}$$

By rearranging Eq. (A1.4), the compliance coefficients can be defined as shown in Eq. (2.13).

2) Appendix (A2)

The six equations for a fixed-free support condition are expressed as follows:

(i) Axial displacement boundary condition at *A*

$$\begin{gathered} u_L = 0 \\ \Rightarrow A_2 = -A_1 e^{ika} \end{gathered} \tag{A2.1}$$

(ii) Transverse displacement boundary condition at *A*

$$\begin{gathered} w_L = 0 \\ \Rightarrow A_3 + A_4 e^{-ik_p a} + A_5 + A_6 e^{-k_e a} = 0 \end{gathered} \tag{A2.2}$$

(iii) Rotational angle boundary condition at *A*

$$\begin{gathered} \theta_L = 0 \\ -iPA_3 + iPA_4 e^{-ik_p a} - NA_5 + NA_6 e^{-k_e a} = 0 \end{gathered} \tag{A2.3}$$

(iv) Axial force boundary condition at *B*

$$\begin{gathered} EAu_R' = 0 \\ \Rightarrow B_2 = B_1 e^{-ikb} \end{gathered} \tag{A2.4}$$

(v) Shear force boundary condition at *B*

$$\begin{gathered} \kappa GA(w_R' - \theta_R) = 0 \\ \Rightarrow -i\big(k_p - P\big)B_3 e^{-ik_p b} + i\big(k_p - P\big)B_4 - (k_e - N)B_5 e^{-k_e b} \\ + (k_e - N)B_6 = 0 \end{gathered} \tag{A2.5}$$

(vi) Moment boundary condition at B

$$\begin{gathered} EI\theta_R' = 0 \\ \Rightarrow -k_p P B_3 e^{-ik_p b} - k_p P B_4 + k_e N B_5 e^{-k_e b} + k_e N B_6 = 0 \end{gathered} \tag{A2.6}$$

The six equations for a free–free support condition are expressed as follows:

(i) Axial force boundary condition at *A*

$$\begin{gathered} EAu_L' = 0 \\ \Rightarrow A_1 e^{ika} = A_2 \end{gathered} \tag{A2.7}$$

(ii) Shear force boundary condition at *A*

$$\begin{gathered} \kappa GA(w_L' - \theta_L) = 0 \\ \Rightarrow -i\big(k_p - P\big)A_3 + i\big(k_p - P\big)A_4 e^{-ik_p a} + (N - k_e)A_5 \\ + (k_e - N)A_6 e^{-k_e a} = 0 \end{gathered} \tag{A2.8}$$

(iii) Moment boundary condition at *A*

$$\begin{gathered} EI\theta_L' = 0 \\ \Rightarrow -k_p P A_3 - k_p P A_4 e^{-ik_p a} + k_e N A_5 + k_e N A_6 e^{-k_e a} = 0 \end{gathered} \tag{A2.9}$$

(iv) Axial force boundary condition at *B*

$$\begin{gathered} EAu_R' = 0 \\ \Rightarrow B_2 = B_1 e^{-ikb} \end{gathered} \tag{A2.10}$$

(v) Shear force boundary condition at *B*

$$\begin{gathered} \kappa GA(w_R' - \theta_R) = 0 \\ \Rightarrow -i\big(k_p - P\big)B_3 e^{-ik_p b} + i\big(k_p - P\big)B_4 - (k_e - N)B_5 e^{-k_e b} \\ + (k_e - N)B_6 = 0 \end{gathered} \tag{A2.11}$$

(vi) Moment boundary condition at *B*

$$\begin{gathered} EI\theta_R' = 0 \\ \Rightarrow -k_p P B_3 e^{-ik_p b} - k_p P B_4 + k_e N B_5 e^{-k_e b} + k_e N B_6 = 0 \end{gathered} \tag{A2.12}$$

The six equations for a fixed-fixed support condition are expressed as follows:

(i) Axial displacement boundary condition at *A*

$$\begin{gathered} u_L = 0 \\ \Rightarrow A_2 = -A_1 e^{ika} \end{gathered} \tag{A2.13}$$

(ii) Transverse displacement boundary condition at *A*

$$\begin{gathered} w_L = 0 \\ \Rightarrow A_3 + A_4 e^{-ik_p a} + A_5 + A_6 e^{-k_e a} = 0 \end{gathered} \tag{A2.14}$$

(iii) Rotational angle boundary condition at *A*

$$\begin{gathered} \theta_L = 0 \\ -iPA_3 + iPA_4 e^{-ik_p a} - NA_5 + NA_6 e^{-k_e a} = 0 \end{gathered} \tag{A2.15}$$

(iv) Axial displacement boundary condition at *B*

$$\begin{gathered} u_R = 0 \\ B_2 = -B_1 e^{-ikb} \end{gathered} \tag{A2.16}$$

(v) Transverse displacement boundary condition at *B*

$$\begin{gathered} w_R = 0 \\ \Rightarrow B_3 e^{-ik_p b} + B_4 + B_5 e^{-k_e b} + B_6 = 0 \end{gathered} \tag{A2.17}$$

(vi) Rotational angle boundary condition at *B*

$$\begin{gathered} \theta_R = 0 \\ \Rightarrow -iPB_3 e^{-ik_p b} + iPB_4 - NB_5 e^{-k_e b} + NB_6 = 0 \end{gathered} \tag{A2.18}$$

The six equations for a fixed–roller support condition are expressed as follows:

(i) Axial displacement boundary condition at *A*

$$\begin{gathered} u_L = 0 \\ \Rightarrow A_2 = -A_1 e^{ika} \end{gathered} \tag{A2.19}$$

(ii) Transverse displacement boundary condition at *A*

$$\begin{gathered} w_L = 0 \\ \Rightarrow A_3 + A_4 e^{-ik_p a} + A_5 + A_6 e^{-k_e a} = 0 \end{gathered} \tag{A2.20}$$

(iii) Rotational angle boundary condition at *A*

$$\begin{gathered} \theta_L = 0 \\ \Rightarrow -iPA_3 + iPA_4 e^{-ik_p a} - NA_5 + NA_6 e^{-k_e a} = 0 \end{gathered} \tag{A2.21}$$

(iv) Axial force boundary condition at *B*

$$\begin{gathered} EAu_R' = 0 \\ \Rightarrow B_2 = B_1 e^{-ikb} \end{gathered} \tag{A2.22}$$

(v) Transverse displacement boundary condition at *B*

$$\begin{gathered} w_R = 0 \\ \Rightarrow B_3 e^{-ik_p b} + B_4 + B_5 e^{-k_e b} + B_6 = 0 \end{gathered} \tag{A2.23}$$

(vi) Moment boundary condition at *B*

$$\begin{gathered} EI\theta_R' = 0 \\ \Rightarrow -k_p PB_3 e^{-ik_p b} - k_p PB_4 + k_e NB_5 e^{-k_e b} + k_e NB_6 = 0 \end{gathered} \tag{A2.24}$$

The six equations for a hinge–free support condition are expressed as follows:

(i) Axial displacement boundary condition at *A*

$$\begin{gathered} u_L = 0 \\ \Rightarrow A_1 e^{ika} = -A_2 \end{gathered} \tag{A2.25}$$

(ii) Transverse displacement boundary condition at *A*

$$\begin{gathered} w_L = 0 \\ \Rightarrow A_3 + A_4 e^{-ik_p a} + A_5 + A_6 e^{-k_e a} = 0 \end{gathered} \tag{A2.26}$$

(iii) Moment boundary condition at *A*

$$\begin{gathered} EI\theta_L' = 0 \\ \Rightarrow -k_p P A_3 - k_p P A_4 e^{-ik_p a} + k_e N A_5 + k_e N A_6 e^{-k_e a} = 0 \end{gathered} \tag{A2.27}$$

(iv) Axial force boundary condition at *B*

$$\begin{gathered} EAu_R' = 0 \\ \Rightarrow B_2 = B_1 e^{-ikb} \end{gathered} \tag{A2.28}$$

(v) Shear force boundary condition at *B*

$$\begin{gathered} \kappa GA(w_R' - \theta_R) = 0 \\ \Rightarrow -i\big(k_p - P\big)B_3 e^{-ik_p b} + i\big(k_p - P\big)B_4 - (k_e - N)B_5 e^{-k_e b} \\ + (k_e - N)B_6 = 0 \end{gathered} \tag{A2.29}$$

(vi) Moment boundary condition at *B*

$$\begin{gathered} EI\theta_R' = 0 \\ \Rightarrow -k_p P B_3 e^{-ik_p b} - k_p P B_4 + k_e N B_5 e^{-k_e b} + k_e N B_6 = 0 \end{gathered} \tag{A2.30}$$

3) Appendix (A3)

The characteristic matrix $\mathbf{C}$ for the different support conditions can be obtained by substituting c_{ij} in the last six rows ($7 \leq i \leq 12$) corresponding to each support condition in Eq. (2.42) using the six equations provided in Appendix (A2). The non-zero components c_{ij} ($7 \leq i \leq 12$) for the fixed-free support condition are defined by combining Eqs. (A2.1) to (A2.6).

$$
\begin{aligned}
&c_{7,1} = e^{ika},\ c_{7,2} = 1,\ c_{8,3} = 1,\ c_{8,4} = e^{-ik_p a},\ c_{8,5} = 1 \\
&c_{8,6} = e^{-k_e a},\ c_{9,3} = -iP,\ c_{9,4} = iPe^{-ik_p a},\ c_{9,5} = -N \\
&c_{9,6} = Ne^{-k_e a},\ c_{10,7} = e^{-ikb},\ c_{10,8} = -1, \\
&c_{11,9} = -i\big(k_p - P\big)e^{-ik_p b},\ c_{11,10} = i\big(k_p - P\big) \\
&c_{11,11} = -(k_e - N)e^{-k_e b},\ c_{11,12} = k_e - N,\ c_{12,9} = -k_p Pe^{-ik_p b} \\
&c_{12,10} = -k_p P,\ c_{12,11} = k_e Ne^{-k_e b},\ c_{12,12} = k_e N
\end{aligned}
\tag{A3.1}
$$

The non-zero components c_{ij} ($7 \leq i \leq 12$) for the free-free support condition are formulated by amalgamating Eqs. (A2.7) to (A2.12).

$$
\begin{aligned}
&c_{7,1} = e^{ika},\ c_{7,2} = -1,\ c_{8,3} = -i\big(k_p - P\big),\ c_{8,4} = i\big(k_p - P\big)e^{-ik_p a} \\
&c_{8,5} = N - k_e,\ c_{8,6} = (k_e - N)e^{-k_e a},\ c_{9,3} = -k_p P \\
&c_{9,4} = -k_p Pe^{-ik_p a},\ c_{9,5} = k_e N,\ c_{9,6} = k_e Ne^{-k_e a},\ c_{10,7} = e^{-ikb} \\
&c_{10,8} = -1,\ c_{11,9} = -i\big(k_p - P\big)e^{-ik_p b},\ c_{11,10} = i\big(k_p - P\big) \\
&c_{11,11} = -(k_e - N)e^{-k_e b},\ c_{11,12} = k_e - N,\ c_{12,9} = -k_p Pe^{-ik_p b} \\
&c_{12,10} = -k_p P,\ c_{12,11} = k_e Ne^{-k_e b},\ c_{12,12} = k_e N
\end{aligned}
\tag{A3.2}
$$

For the fixed-fixed support condition, the non-zero components c_{ij} $(7 \leq i \leq 12)$ are represented by combining Eqs. (A2.13) to (A2.18).

$$\begin{aligned}
&c_{7,1} = e^{ika},\ c_{7,2} = 1,\ c_{8,3} = 1,\ c_{8,4} = e^{-ik_p a},\ c_{8,5} = 1 \\
&c_{8,6} = e^{-k_e a},\ c_{9,3} = -iP,\ c_{9,4} = iPe^{-ik_p a},\ c_{9,5} = -N \\
&c_{9,6} = Ne^{-k_e a},\ c_{10,7} = e^{-ikb},\ c_{10,8} = 1,\ c_{11,9} = e^{-ik_p b},\ c_{11,10} = 1 \\
&c_{11,11} = e^{-k_e b},\ c_{11,12} = 1,\ c_{12,9} = -iPe^{-ik_p b},\ c_{12,10} = iP \\
&c_{12,11} = -Ne^{-k_e b},\ c_{12,12} = N
\end{aligned} \tag{A3.3}$$

The non-zero components c_{ij} $(7 \leq i \leq 12)$ of a fixed-roller support condition are constructed by merging Eqs. (A2.19) to (A2.24).

$$\begin{aligned}
&c_{7,1} = e^{ika},\ c_{7,2} = 1,\ c_{8,3} = 1,\ c_{8,4} = e^{-ik_p a},\ c_{8,5} = 1 \\
&c_{8,6} = e^{-k_e a},\ c_{9,3} = -iP,\ c_{9,4} = iPe^{-ik_p a},\ c_{9,5} = -N \\
&c_{9,6} = Ne^{-k_e a},\ c_{10,7} = e^{-ikb},\ c_{10,8} = -1,\ c_{11,9} = e^{-ik_p b} \\
&c_{11,10} = 1,\ c_{11,11} = e^{-k_e b},\ c_{11,12} = 1,\ c_{12,9} = -k_p Pe^{-ik_p b} \\
&c_{12,10} = -k_p P,\ c_{12,11} = k_e Ne^{-k_e b},\ c_{12,12} = k_e N
\end{aligned} \tag{A3.4}$$

The non-zero components c_{ij} $(7 \leq i \leq 12)$ for a hinge-free support condition are defined by amalgamating Eqs. (A2.25) to (A2.30).

$$\begin{aligned}
&c_{7,1} = e^{ika},\ c_{7,2} = 1,\ c_{8,3} = 1,\ c_{8,4} = e^{-ik_p a},\ c_{8,5} = 1 \\
&c_{8,6} = e^{-k_e a},\ c_{9,3} = -k_p P,\ c_{9,4} = -k_p Pe^{-ik_p a},\ c_{9,5} = k_e N \\
&c_{9,6} = k_e Ne^{-k_e a},\ c_{10,7} = e^{-ikb},\ c_{10,8} = -1 \\
&c_{11,9} = -i\big(k_p - P\big)e^{-ik_p b},\ c_{11,10} = i\big(k_p - P\big) \\
&c_{11,11} = -(k_e - N)e^{-k_e b},\ c_{11,12} = k_e - N,\ c_{12,9} = -k_p Pe^{-ik_p b} \\
&c_{12,10} = -k_p P,\ c_{12,11} = k_e Ne^{-k_e b},\ c_{12,12} = k_e N
\end{aligned} \tag{A3.5}$$

4) Appendix (A4)

For a simply supported condition, the non-zero components γ_{ij} in $\frac{\partial \mathbf{C}}{\partial k}$, $\frac{\partial \mathbf{C}}{\partial k_p}$, $\frac{\partial \mathbf{C}}{\partial k_e}$, $\frac{\partial \mathbf{C}}{\partial P}$ and $\frac{\partial \mathbf{C}}{\partial N}$ are expressed as follows:

(i) Non-zero components in $\frac{\partial \mathbf{C}}{\partial k}$

$$\begin{aligned}
&\gamma_{1,1} = -iF_{aa}e^{-ika} - ia(1 - ikF_{aa})e^{-ika},\ \gamma_{1,2} = iF_{aa},\\
&\gamma_{1,8} = ibe^{-ikb},\ \gamma_{3,1} = iF_{ba}e^{-ika} + akF_{ba}e^{-ika},\ \gamma_{3,2} = -iF_{ba}\\
&\gamma_{4,1} = -iae^{-ika},\ \gamma_{4,8} = -ibe^{-ikb},\ \gamma_{7,1} = iae^{ika}\\
&\gamma_{10,7} = -ibe^{-ikb}
\end{aligned} \tag{A4.1}$$

(ii) Non-zero components in $\frac{\partial \mathbf{C}}{\partial k_p}$

$$\begin{aligned}
&\gamma_{1,3} = -F_{ab}Pe^{-ik_pa} + iaF_{ab}k_pPe^{-ik_pa},\ \gamma_{1,4} = -F_{ab}P\\
&\gamma_{2,3} = -iF_{ss}e^{-ik_pa} - ia\{1 - i(k_p - P)F_{ss}\}e^{-ik_pa},\ \gamma_{2,4} = iF_{ss}\\
&\gamma_{2,10} = ibe^{-ik_pb},\ \gamma_{3,3} = PF_{bb}e^{-ik_pa} - ia(iP + k_pPF_{bb})e^{-ik_pa}\\
&\gamma_{3,4} = PF_{bb},\ \gamma_{3,10} = bPe^{-ik_pb},\ \gamma_{5,3} = ie^{-ik_pa} - a(P - k_p)e^{-ik_pa}\\
&\gamma_{5,4} = -i,\ \gamma_{5,9} = -i,\ \gamma_{5,10} = \{i - b(P - k_p)\}e^{-ik_pb}\\
&\gamma_{6,3} = Pe^{-ik_pa} - iak_pPe^{-ik_pa},\ \gamma_{6,4} = P,\ \gamma_{6,9} = -P\\
&\gamma_{6,10} = -Pe^{-ik_pb} + ibk_pPe^{-ik_pb},\ \gamma_{8,4} = -iae^{-ik_pa},\ \gamma_{9,3} = -P\\
&\gamma_{9,4} = -Pe^{-ik_pa} + iak_pPe^{-ik_pa},\ \gamma_{11,9} = -ibe^{-ik_pb}\\
&\gamma_{12,9} = -Pe^{-ik_pb} + ibk_pPe^{-ik_pb},\ \gamma_{12,10} = -P
\end{aligned} \tag{A4.2}$$

(iii) Non-zero components in $\frac{\partial \mathbf{C}}{\partial k_e}$

$$\gamma_{1,5} = F_{ab}N(1-ak_e)e^{-k_e a},\ \gamma_{1,6} = F_{ab}N$$
$$\gamma_{2,5} = \{-F_{ss} - a + a(k_e - N)F_{ss}\}e^{-k_e a},\ \gamma_{2,6} = F_{ss},\ \gamma_{2,12} = be^{-k_e b}$$
$$\gamma_{3,5} = (-NF_{bb} - aN + ak_eNF_{bb})e^{-k_e a},\ \gamma_{3,6} = -NF_{bb}$$
$$\gamma_{3,12} = -bNe^{-k_e b},\ \gamma_{5,5} = e^{-k_e a} - a(k_e - N)e^{-k_e a},\ \gamma_{5,6} = -1$$
$$\gamma_{5,11} = -1$$
$$\gamma_{5,12} = e^{-k_e b} - b(k_e - N)e^{-k_e b},\ \gamma_{6,5} = -Ne^{-k_e a} + ak_eNe^{-k_e a} \quad \text{(A4.3)}$$
$$\gamma_{6,6} = -N,\ \gamma_{6,11} = N,\ \gamma_{6,12} = Ne^{-k_e b} - bk_eNe^{-k_e b}$$
$$\gamma_{8,6} = -ae^{-k_e a},\ \gamma_{9,5} = N,\ \gamma_{9,6} = Ne^{-k_e a} - ak_eNe^{-k_e a}$$
$$\gamma_{11,11} = -be^{-k_e b},\ \gamma_{12,11} = N(1-bk_e)e^{-k_e b},\ \gamma_{12,12} = N$$

(iv) Non-zero components in $\frac{\partial \mathbf{C}}{\partial P}$

$$\gamma_{1,3} = -F_{ab}k_p e^{-ik_p a},\ \gamma_{1,4} = -F_{ab}k_p,\ \gamma_{2,3} = iF_{ss}e^{-ik_p a}$$
$$\gamma_{2,4} = -iF_{ss},\ \gamma_{3,3} = \left(i + k_p F_{bb}\right)e^{-ik_p a},\ \gamma_{3,4} = -i + k_p F_{bb}$$
$$\gamma_{3,9} = -i,\ \gamma_{3,10} = ie^{-ik_p b},\ \gamma_{5,3} = -ie^{-ik_p a},\ \gamma_{5,4} = i,\ \gamma_{5,9} = i$$
$$\gamma_{5,10} = -ie^{-ik_p b},\ \gamma_{6,3} = k_p e^{-ik_p a},\ \gamma_{6,4} = k_p,\ \gamma_{6,9} = -k_p \quad \text{(A4.4)}$$
$$\gamma_{6,10} = -k_p e^{-ik_p b},\ \gamma_{9,3} = -k_p,\ \gamma_{9,4} = -k_p e^{-ik_p a},$$
$$\gamma_{12,9} = -k_p e^{-ik_p b},\ \gamma_{12,10} = -k_p$$

(v) Non-zero components in $\frac{\partial \mathbf{C}}{\partial N}$

$$\gamma_{1,5} = F_{ab}k_e e^{-k_e a},\ \gamma_{1,6} = F_{ab}k_e,\ \gamma_{2,5} = F_{ss}e^{-k_e a},\ \gamma_{2,6} = -F_{ss}$$
$$\gamma_{3,5} = (1 - k_e F_{bb})e^{-k_e a},\ \gamma_{3,6} = -1 - k_e F_{bb},\ \gamma_{3,11} = -1$$
$$\gamma_{3,12} = e^{-k_e b},\ \gamma_{5,5} = -e^{-k_e a},\ \gamma_{5,6} = 1,\ \gamma_{5,11} = 1,\ \gamma_{5,12} = -e^{-k_e b} \quad \text{(A4.5)}$$
$$\gamma_{6,5} = -k_e e^{-k_e a},\ \gamma_{6,6} = -k_e,\ \gamma_{6,11} = k_e,\ \gamma_{6,12} = k_e e^{-k_e b}$$
$$\gamma_{9,5} = k_e,\ \gamma_{9,6} = k_e e^{-k_e a},\ \gamma_{12,11} = k_e e^{-k_e b},\ \gamma_{12,12} = k_e$$

Note that for all support conditions, $\frac{\partial \mathbf{C}}{\partial k}$ aligns with the simply supported condition as detailed in Eq. (A4.1). Consequently, other support conditions focus solely on $\frac{\partial \mathbf{C}}{\partial k_p}$, $\frac{\partial \mathbf{C}}{\partial k_e}$, $\frac{\partial \mathbf{C}}{\partial P}$ and $\frac{\partial \mathbf{C}}{\partial N}$. Given that the first six rows are commonly applicable to all cracked beams, the discussion is restricted to rows 7 to 12, which relate to the boundary conditions.

The non-zero components γ_{ij}, from rows 7 to 12, for a fixed-free support condition are as follows:

(i) Non-zero components in $\frac{\partial \mathbf{C}}{\partial k_p}$

$$\begin{aligned}&\gamma_{8,4} = -iae^{-ik_p a},\ \gamma_{9,4} = aPe^{-ik_p a}\\ &\gamma_{11,9} = -ie^{-ik_p b} - b\big(k_p - P\big)e^{-ik_p b},\ \gamma_{11,10} = i\\ &\gamma_{12,9} = -Pe^{-ik_p b} + ibk_p Pe^{-ik_p b},\ \gamma_{12,10} = -P\end{aligned} \tag{A4.6}$$

(ii) Non-zero components in $\frac{\partial \mathbf{C}}{\partial k_e}$

$$\begin{aligned}&\gamma_{8,6} = -ae^{-k_e a},\ \gamma_{9,6} = -aNe^{-k_e a}\\ &\gamma_{11,11} = -e^{-k_e b} + b(k_e - N)e^{-k_e b},\ \gamma_{11,12} = 1\\ &\gamma_{12,11} = Ne^{-k_e b} - bk_e Ne^{-k_e b},\ \gamma_{12,12} = N\end{aligned} \tag{A4.7}$$

(iii) Non-zero components in $\frac{\partial \mathbf{C}}{\partial P}$

$$\begin{aligned}&\gamma_{9,3} = -i,\ \gamma_{9,4} = ie^{-ik_p a},\ \gamma_{11,9} = ie^{-ik_p b},\ \gamma_{11,10} = -i\\ &\gamma_{12,9} = -k_p e^{-ik_p b},\ \gamma_{12,10} = -k_p\end{aligned} \tag{A4.8}$$

(iv) Non-zero components in $\frac{\partial \mathbf{C}}{\partial N}$

$$\begin{aligned}&\gamma_{9,5} = -1,\ \gamma_{9,6} = e^{-k_e a},\ \gamma_{11,11} = e^{-k_e b},\ \gamma_{11,12} = -1\\ &\gamma_{12,11} = k_e e^{-k_e b},\ \gamma_{12,12} = k_e\end{aligned} \tag{A4.9}$$

The non-zero components γ_{ij}, from rows 7 to 12, for a free-free support condition are as follows:

(i) Non-zero components in $\frac{\partial \mathbf{C}}{\partial k_p}$

$$\begin{aligned}&\gamma_{8,3} = -i,\ \gamma_{8,4} = ie^{-ik_p a} + a\big(k_p - P\big)e^{-ik_p a},\ \gamma_{9,3} = -P\\&\gamma_{9,4} = \big(-P + iak_p P\big)e^{-ik_p a},\ \gamma_{11,9} = \big\{-i - b\big(k_p - P\big)\big\}e^{-ik_p b}\\&\gamma_{11,10} = i,\ \gamma_{12,9} = P\big(-1 + ibk_p\big)e^{-ik_p b},\ \gamma_{12,10} = -P\end{aligned} \tag{A4.10}$$

(ii) Non-zero components in $\frac{\partial \mathbf{C}}{\partial k_e}$

$$\begin{aligned}&\gamma_{8,5} = -1,\ \gamma_{8,6} = e^{-k_e a} - a(k_e - N)e^{-k_e a},\ \gamma_{9,5} = N\\&\gamma_{9,6} = Ne^{-k_e a} - ak_e Ne^{-k_e a},\ \gamma_{11,11} = -e^{-k_e b} + b(k_e - N)e^{-k_e b}\\&\gamma_{11,12} = 1,\ \gamma_{12,11} = N(1 - bk_e)e^{-k_e b},\ \gamma_{12,12} = N\end{aligned} \tag{A4.11}$$

(iii) Non-zero components in $\frac{\partial \mathbf{C}}{\partial P}$

$$\begin{aligned}&\gamma_{8,3} = i,\ \gamma_{8,4} = -ie^{-ik_p a},\ \gamma_{9,3} = -k_p,\ \gamma_{9,4} = -k_p e^{-ik_p a}\\&\gamma_{11,9} = ie^{-ik_p b},\ \gamma_{11,10} = -i,\ \gamma_{12,9} = -k_p e^{-ik_p b},\ \gamma_{12,10} = -k_p\end{aligned} \tag{A4.12}$$

(iv) Non-zero components in $\frac{\partial \mathbf{C}}{\partial N}$

$$\begin{aligned}&\gamma_{8,5} = 1,\ \gamma_{8,6} = -e^{-k_e a},\ \gamma_{9,5} = k_e,\ \gamma_{9,6} = k_e e^{-k_e a}\\&\gamma_{11,11} = e^{-k_e b},\ \gamma_{11,12} = -1,\ \gamma_{12,11} = k_e e^{-k_e b},\ \gamma_{12,12} = k_e\end{aligned} \tag{A4.13}$$

The non-zero components γ_{ij}, from rows 7–12, for a fixed-fixed support condition are as follows:

(i) Non-zero components in $\frac{\partial \mathbf{C}}{\partial k_p}$

$$\gamma_{8,4} = -iae^{-ik_p a},\ \gamma_{9,4} = aPe^{-ik_p a},\ \gamma_{11,9} = -ibe^{-ik_p b} \tag{A4.14}$$

$$\gamma_{12,9} = -bPe^{-ik_p b}$$

(ii) Non-zero components in $\frac{\partial \mathbf{C}}{\partial k_e}$

$$\gamma_{8,6} = -ae^{-k_e a},\ \gamma_{9,6} = -aNe^{-k_e a},\ \gamma_{11,11} = -be^{-k_e b}$$
$$\gamma_{12,11} = bNe^{-k_e b} \quad \text{(A4.15)}$$

(iii) Non-zero components in $\frac{\partial \mathbf{C}}{\partial P}$

$$\gamma_{9,3} = -i,\ \gamma_{9,4} = ie^{-ik_p a},\ \gamma_{12,9} = -ie^{-ik_p b},\ \gamma_{12,10} = i \quad \text{(A4.16)}$$

(iv) Non-zero components in $\frac{\partial \mathbf{C}}{\partial N}$

$$\gamma_{9,5} = -1,\ \gamma_{9,6} = e^{-k_e a},\ \gamma_{12,11} = -e^{-k_e b},\ \gamma_{12,12} = 1 \quad \text{(A4.17)}$$

The non-zero components γ_{ij}, from rows 7 to 12, for a fixed-roller support condition are as follows:

(i) Non-zero components in $\frac{\partial \mathbf{C}}{\partial k_p}$

$$\gamma_{8,4} = -iae^{-ik_p a},\ \gamma_{9,4} = aPe^{-ik_p a},\ \gamma_{11,9} = -ibe^{-ik_p b}$$
$$\gamma_{12,9} = -Pe^{-ik_p b} + ibk_p Pe^{-ik_p b},\ \gamma_{12,10} = -P \quad \text{(A4.18)}$$

(ii) Non-zero components in $\frac{\partial \mathbf{C}}{\partial k_e}$

$$\gamma_{8,6} = -ae^{-k_e a},\ \gamma_{9,6} = -aNe^{-k_e a},\ \gamma_{11,11} = -be^{-k_e b}$$
$$\gamma_{12,11} = N(1 - bk_e)e^{-k_e b},\ \gamma_{12,12} = N \quad \text{(A4.19)}$$

(iii) Non-zero components in $\frac{\partial \mathbf{C}}{\partial P}$

$$\gamma_{9,3} = -i,\ \gamma_{9,4} = ie^{-ik_p a},\ \gamma_{12,9} = -k_p e^{-ik_p b},\ \gamma_{12,10} = -k_p \quad \text{(A4.20)}$$

(iv) Non-zero components in $\frac{\partial \mathbf{C}}{\partial N}$

$$\gamma_{9,5} = -1,\ \gamma_{9,6} = e^{-k_e a},\ \gamma_{12,11} = k_e e^{-k_e b},\ \gamma_{12,12} = k_e \tag{A4.21}$$

The non-zero components γ_{ij}, from rows 7–12, for a hinge-free support condition are as follows:

(i) Non-zero components in $\frac{\partial \mathbf{C}}{\partial k_p}$

$$\begin{aligned}&\gamma_{8,4} = -iae^{-ik_p a},\ \gamma_{9,3} = -P,\ \gamma_{9,4} = -Pe^{-ik_p a} + iak_p Pe^{-ik_p a}\\ &\gamma_{11,9} = \{-i - b(k_p - P)\}e^{-ik_p b},\ \gamma_{11,10} = i\\ &\gamma_{12,9} = P(-1 + ibk_p)e^{-ik_p b},\ \gamma_{12,10} = -P\end{aligned} \tag{A4.22}$$

(ii) Non-zero components in $\frac{\partial \mathbf{C}}{\partial k_e}$

$$\begin{aligned}&\gamma_{8,6} = -ae^{-k_e a},\ \gamma_{9,5} = N,\ \gamma_{9,6} = Ne^{-k_e a} - ak_e Ne^{-k_e a}\\ &\gamma_{11,11} = -e^{-k_e b} + b(k_e - N)e^{-k_e b},\ \gamma_{11,12} = 1\\ &\gamma_{12,11} = N(1 - bk_e)e^{-k_e b},\ \gamma_{12,12} = N\end{aligned} \tag{A4.23}$$

(iii) Non-zero components in $\frac{\partial \mathbf{C}}{\partial P}$

$$\begin{aligned}&\gamma_{9,3} = -k_p,\ \gamma_{9,4} = -k_p e^{-ik_p a},\ \gamma_{11,9} = ie^{-ik_p b},\ \gamma_{11,10} = -i\\ &\gamma_{12,9} = -k_p e^{-ik_p b},\ \gamma_{12,10} = -k_p\end{aligned} \tag{A4.24}$$

(iv) Non-zero components in $\frac{\partial \mathbf{C}}{\partial N}$

$$\begin{aligned}&\gamma_{9,5} = k_e,\ \gamma_{9,6} = k_e e^{-k_e a},\ \gamma_{11,11} = e^{-k_e b},\ \gamma_{11,12} = -1\\ &\gamma_{12,11} = k_e e^{-k_e b},\ \gamma_{12,12} = k_e\end{aligned} \tag{A4.25}$$

5) Appendix (A5)

For each support of the beam, β_L can be derived from the boundary conditions associated with the axial of support *A*.

(i) Hinge or fixed support condition

The axial displacement boundary condition at the left end of the beam is as follows:

$$A_1 e^{ika} = -A_2 \tag{A5.1}$$

Multiplying Eq. (A5.1) by e^{-ika} provides the form of Eq. (3.38).

$$A_2 = \underbrace{-e^{2ika}}_{t_L} A_1 e^{-ika} \tag{A5.2}$$

In Eq. (3.37a), t_L is represented as $-e^{2ika}$, which leads to the conclusion that β_L is equal to -1, as it is derived from $\beta_L e^{2ika}$.

(ii) Free support condition

The axial force boundary condition at the left end of the beam is as follows:

$$A_1 e^{ika} = A_2 \tag{A5.3}$$

Multiplying Eq. (A5.3) by e^{-ika} provides the form of Eq. (3.38).

$$A_2 = \underbrace{e^{2ika}}_{t_L} A_1 e^{-ika} \tag{A5.4}$$

In Eq. (3.37a), t_L is represented as e^{2ika}, which leads to the conclusion that β_L is equal to 1, as it is derived from $\beta_L e^{2ika}$.

For each support, β_R can be computed from the boundary conditions associated

with the axial of support *B*.

(i) Roller or free support condition

The axial force boundary condition at the right end of the beam is as follows:

$$B_2 = B_1 e^{-ikb} \tag{A5.5}$$

Multiplying Eq. (A5.5) by e^{-ikb} provides the form of Eq. (3.39).

$$B_2 e^{-ikb} = \underbrace{e^{-2ikb}}_{t_R} B_1 \tag{A5.6}$$

In Eq. (3.37b), t_R is represented as e^{-2ikb}, which leads to the conclusion that β_R is equal to 1, as it is derived from $\beta_R e^{-2ikb}$.

(ii) Fixed support condition

The axial displacement boundary condition at the right end of the beam is as follows:

$$B_2 = -B_1 e^{-ikb} \tag{A5.7}$$

Multiplying Eq. (A5.7) by e^{-ikb} provides the form of Eq. (3.39).

$$B_2 e^{-ikb} = \underbrace{-e^{-2ikb}}_{t_R} B_1 \tag{A5.8}$$

In Eq. (3.37b), t_R is represented as $-e^{-2ikb}$, which leads to the conclusion that β_R is equal to -1, as it is derived from $\beta_R e^{-2ikb}$.

For each support, $\bar{t}_L$ can be computed from the boundary conditions associated with the bending of support *A*.

(i) Hinge support condition

The transverse displacement boundary condition at the right end of the beam is as follows:

$$A_3 + A_4 e^{-ik_p a} + A_5 + \underbrace{A_6 e^{-k_e a}}_{0} = 0 \tag{A5.9}$$

The moment boundary condition at the right end of the beam is as follows:

$$-k_p P A_3 - k_p P A_4 e^{-ik_p a} + k_e N A_5 + \underbrace{k_e N A_6 e^{-k_e a}}_{0} = 0 \tag{A5.10}$$

Substituting $k_e N \times$ Eq. (A5.9) into Eq. (A5.10) results in :

$$A_3 = -A_4 e^{-ik_p a} \tag{A5.11}$$

Multiplying Eq. (A5.11) by $e^{-ik_p a}$ provides the form of Eq. (3.40).

$$A_4 = \underbrace{-e^{2ik_p a}}_{\bar{t}_L} A_3 e^{-ik_p a} \tag{A5.12}$$

In Eq. (3.37c), $\bar{t}_L$ is represented as $-e^{2ik_p a}$, which leads to the conclusion that $\bar{\beta}_L$ is equal to -1, as it is derived from $\bar{\beta}_L e^{2ik_p a}$.

(ii) Fixed support condition

The transverse displacement boundary condition at the right end of the beam is as follows:

$$A_3 + A_4 e^{-ik_p a} + A_5 + \underbrace{A_6 e^{-k_e a}}_{0} = 0 \tag{A5.13}$$

The rotational angle boundary condition at the right end of the beam is as follows:

$$-iP A_3 + iP A_4 e^{-ik_p a} - N A_5 + \underbrace{N A_6 e^{-k_e a}}_{0} = 0 \tag{A5.14}$$

Substituting $N \times$ Eq. (A5.13) into Eq. (A5.14) results in:

$$A_3 = -\frac{N + iP}{N - iP} A_4 e^{-ik_p a} \tag{A5.15}$$

Multiplying Eq. (A5.15) by $e^{-ik_p a}$ provides the form of Eq. (3.40).

$$A_4 = \underbrace{\frac{P + iN}{P - iN} e^{2ik_p a}}_{\bar{t}_L} A_3 e^{-ik_p a} \tag{A5.16}$$

In Eq. (3.37c), $\bar{t}_L$ is represented as $\frac{P+iN}{P-iN} e^{2ik_p a}$, which leads to the conclusion that $\bar{\beta}_L$ is equal to $\frac{P+iN}{P-iN}$, as it is derived from $\bar{\beta}_L e^{2ik_p a}$.

(iii) Free support condition

The shear force boundary condition at the right end of the beam is as follows:

$$\begin{aligned} -i(k_p - P)A_3 + i(k_p - P)A_4 e^{-ik_p a} + (N - k_e)A_5 \\ + \underbrace{(k_e - N)A_6 e^{-k_e a}}_{0} = 0 \end{aligned} \tag{A5.17}$$

The moment boundary condition at the right end of the beam is as follows:

$$-k_p P A_3 - k_p P A_4 e^{-ik_p a} + k_e N A_5 + \underbrace{k_e N A_6 e^{-k_e a}}_{0} = 0 \tag{A5.18}$$

Substituting $k_e N \times$ Eq. (A5.17) into $(N - k_e) \times$ Eq. (A5.18) results in:

$$A_3 = -\frac{P(N - k_e) + i\gamma_e N(k_p - P)}{P(N - k_e) - i\gamma_e N(k_p - P)} A_4 e^{-ik_p a} \tag{A5.19}$$

where $\frac{k_p - P}{N - k_e} = \frac{k_e}{k_p} = \gamma_e$

Multiplying Eq. (A5.19) by $e^{-ik_p a}$ provides the form of Eq. (3.40).

$$A_4 = \underbrace{-\frac{P - i\gamma_e^2 N}{P + i\gamma_e^2 N} e^{2ik_p a}}_{\bar{t}_L} A_3 e^{-ik_p a} \tag{A5.20}$$

In Eq. (3.37c), $\bar{t}_L$ is represented as $-\frac{P-i\gamma_e^2 N}{P+i\gamma_e^2 N}e^{2ik_p a}$, which leads to the conclusion that $\bar{\beta}_L$ is equal to $-\frac{P-i\gamma_e^2 N}{P+i\gamma_e^2 N}$, as it is derived from $\bar{\beta}_L e^{2ik_p a}$.

For each support, $\bar{t}_R$ can be computed from the boundary conditions associated with the bending of support *B*.

(i) Roller support condition

The transverse displacement boundary condition at the right end of the beam is as follows:

$$B_3 e^{-ik_p b} + B_4 + \underbrace{B_5 e^{-k_e b}}_{0} + B_6 = 0 \tag{A5.21}$$

The moment boundary condition at the right end of the beam is as follows:

$$-k_p P B_3 e^{-ik_p b} - k_p P B_4 + \underbrace{k_e N B_5 e^{-k_e b}}_{0} + k_e N B_6 = 0 \tag{A5.22}$$

Substituting $k_e N \times$ Eq. (A5.21) into Eq. (A5.22) results in :

$$B_3 e^{-ik_p b} = -B_4 \tag{A5.23}$$

Multiplying Eq. (A5.23) by $e^{-ik_p b}$ provides the form of Eq. (3.41).

$$B_4 e^{-ik_p b} = \underbrace{-e^{-2ik_p b}}_{\bar{t}_R} B_3 \tag{A5.24}$$

In Eq. (3.37d), $\bar{t}_R$ is represented as $-e^{-2ik_p b}$, which leads to the conclusion that $\bar{\beta}_R$ is equal to -1, as it is derived from $\bar{\beta}_R e^{-2ik_p b}$.

(ii) Fixed support condition

The transverse displacement boundary condition at the right end of the beam is as follows:

$$B_3 e^{-ik_p b} + B_4 + \underbrace{B_5 e^{-k_e b}}_{0} + B_6 = 0 \tag{A5.25}$$

The rotational angle boundary condition at the right end of the beam is as follows:

$$-iPB_3 e^{-ik_p b} + iPB_4 - \underbrace{NB_5 e^{-k_e b}}_{0} + NB_6 = 0 \tag{A5.26}$$

Substituting $N \times$ Eq. (A5.25) into Eq. (A5.26) results in :

$$B_3 e^{-ik_p b} = -\frac{N - iP}{N + iP} B_4 \tag{A5.27}$$

Multiplying Eq. (A5.27) by $e^{-ik_p b}$ provides the form of Eq. (3.41).

$$B_4 e^{-ik_p b} = \underbrace{\frac{P - iN}{P + iN} e^{-2ik_p b}}_{\bar{t}_R} B_3 \tag{A5.28}$$

In Eq. (3.37d), $\bar{t}_R$ is represented as $\frac{P-iN}{P+iN} e^{-2ik_p b}$, which leads to the conclusion that $\bar{\beta}_R$ is equal to $\frac{P-iN}{P+iN}$, as it is derived from $\bar{\beta}_R e^{-2ik_p b}$. A comparison with Eq. (A5.16) under the fixed support condition shows that $\bar{\beta}_R$ represents the reciprocal of $\bar{\beta}_L$.

(iii) Free support condition

The shear force boundary condition at the right end of the beam is as follows:

$$\begin{aligned} -i(k_p - P)B_3 e^{-ik_p b} + i(k_p - P)B_4 - \underbrace{(k_e - N)B_5 e^{-k_e b}}_{0} \\ + (k_e - N)B_6 = 0 \end{aligned} \tag{A5.29}$$

The moment boundary condition at the right end of the beam is as follows:

$$-k_p P B_3 e^{-ik_p b} - k_p P B_4 - \underbrace{k_e N B_5 e^{-k_e b}}_{0} + k_e N B_6 = 0 \qquad \text{(A5.30)}$$

Substituting $k_e N \times$ Eq. (A5.29) into $(k_e - N) \times$ Eq. (A5.30) results in:

$$B_3 e^{-ik_p b} = -\frac{k_p P(k_e - N) + ik_e N(k_p - P)}{k_p P(k_e - N) - ik_e N(k_p - P)} B_4 \qquad \text{(A5.31)}$$

where $\frac{k_p - P}{k_e - N} = -\frac{k_e}{k_p} = -\gamma_e$

Multiplying Eq. (A5.31) by $e^{-ik_p b}$ provides the form of Eq. (3.41).

$$B_4 e^{-ik_p b} = \underbrace{-\frac{P + i\gamma_e^2 N}{P - i\gamma_e^2 N} e^{-2ik_p b}}_{\bar{t}_R} B_3 \qquad \text{(A5.32)}$$

In Eq. (3.37d), $\bar{t}_R$ is represented as $-\frac{P+i\gamma_e^2 N}{P-i\gamma_e^2 N} e^{-2ik_p b}$, which leads to the conclusion that $\bar{\beta}_R$ is equal to $-\frac{P+i\gamma_e^2 N}{P-i\gamma_e^2 N}$, as it is derived from $\bar{\beta}_R e^{-2ik_p b}$. A comparison with Eq. (A5.20) under the free support condition shows that $\bar{\beta}_R$ represents the reciprocal of $\bar{\beta}_L$.

6) Appendix (A6)

By differentiating Eq. (4.19) with respect to F_{ss}.

$$-2(1+\hat{\gamma}_e^2)\left(\frac{\partial \hat{t}_l}{\partial F_{ss}}-\frac{\partial \hat{t}_r}{\partial F_{ss}}\right)\gamma_e + \hat{\gamma}_q^2\left[\left(1-\hat{\gamma}_q^2\right)(\hat{t}_L-\hat{t}_R) + i\hat{\gamma}_e\left(\hat{\gamma}_e^2+\hat{\gamma}_q^2\right)(1-\hat{t}_L)(1-\hat{t}_R)\right]\hat{k}_p = 0 \quad \text{(A6.1)}$$

The derivative $\frac{\partial \hat{t}_l}{\partial F_{ss}}$ in Eq. (A6.1) can be derived using the chain rule.

$$\frac{\partial \hat{t}_l}{\partial F_{ss}} = \frac{\partial \hat{t}_l}{\partial \hat{k}_p}\frac{\partial \hat{k}_p}{\partial F_{ss}} = \left(\frac{\partial \beta_L}{\partial \hat{k}_p} + 2ia\beta_L\right)e^{2ik_p a}\frac{\partial \hat{k}_p}{\partial F_{ss}} \quad \text{(A6.2)}$$

The derivative $\frac{\partial \hat{t}_r}{\partial F_{ss}}$ in Eq. (A6.1) can be expressed using the same method as in Eq. (A6.2).

$$\frac{\partial \hat{t}_r}{\partial F_{ss}} = \frac{\partial \hat{t}_r}{\partial \hat{k}_p}\frac{\partial \hat{k}_p}{\partial F_{ss}} = \left(\frac{\partial \beta_R}{\partial \hat{k}_p} - 2ib\beta_R\right)e^{-2ik_p a}\frac{\partial \hat{k}_p}{\partial F_{ss}} \quad \text{(A6.3)}$$

Calculate $\frac{\partial \hat{t}_l}{\partial F_{ss}}-\frac{\partial \hat{t}_r}{\partial F_{ss}}$ in Eq. (A6.1) by subtracting Eq. (A6.3) from Eq. (A6.2).

$$\frac{\partial \hat{t}_l}{\partial F_{ss}}-\frac{\partial \hat{t}_r}{\partial F_{ss}} = \left\{\left(\frac{\partial \beta_L}{\beta_L \partial \hat{k}_p}-\frac{\partial \beta_R}{\beta_R \partial \hat{k}_p}\right)+2iL\right\}\hat{t}_L\frac{\partial \hat{k}_p}{\partial F} \quad \text{(A6.4)}$$

Substituting Eq. (A6.4) into Eq. (A6.1) and rearranging for $\frac{\partial \hat{k}_p}{\partial F}$ yields the following expression:

$$\frac{\partial \hat{k}_p}{\partial F}$$

$$= \frac{\hat{\gamma}_q^2\left[\left(1-\hat{\gamma}_q^2\right)\left(\hat{t}_L-\hat{t}_R\right)+i\hat{\gamma}_e\left(\hat{\gamma}_e^2+\hat{\gamma}_q^2\right)\left(1-\hat{t}_L-\hat{t}_R+\hat{t}_R\hat{t}_L\right)\right]}{4i\left(1+\hat{\gamma}_e^2\right)\left\{1+\left(\frac{\partial \beta_l}{\beta_l \partial \hat{k}_p}-\frac{\partial \beta_r}{\beta_r \partial \hat{k}_p}\right)/2iL\right\}\hat{t}_L\hat{\gamma}_e}\frac{\hat{k}_p}{L} \qquad \text{(A6.5)}$$

Defining $\hat{\zeta}$ as $\frac{\partial \beta_l}{\beta_l \partial \hat{k}_p}-\frac{\partial \beta_r}{\beta_r \partial \hat{k}_p}$ in Eq. (A4.5) yields Eq. (4.23).

References

Alt17

Altunışık, A. C., Okur, F. Y., Kahya, V. Structural identification of a cantilever beam with multiple cracks: Modeling and validation. International Journal of Mechanical Sciences, 130, 74-89 (2017).

Alt19

Altunışık, A. C., Okur, F. Y., Kahya, V. Vibrations of a box-sectional cantilever Timoshenko beam with multiple cracks. International Journal of Steel Structures, 19, 635-649 (2019).

Ast15

American Society for Testing and Materials. ASTM E1820: Standard Test Method for Measurement of Fracture Toughness (2015).

Bha04

Bhalla, S., Soh, C. K. High frequency piezoelectric signatures for diagnosis of seismic/blast induced structural damages. NDT & E International, 37(1), 23-33 (2004).

Cad09

Caddemi, S., Calio, I. Exact closed-form solution for the vibration modes of the Euler–Bernoulli beam with multiple open cracks. Journal of Sound and Vibration, 327(3-5), 473-489 (2009).

Cal16

Caliò, I., Greco, A., D'Urso, D. Structural models for the evaluation of eigen-properties in damaged spatial arches: a critical appraisal. Archive of Applied Mechanics, 86, 1853-1867 (2016).

Car02

Carneiro, S. H., Inman, D. J. Continuous model for the transverse vibration of cracked Timoshenko beams. Journal of Vibration and Acoustics, 124(2), 310-320 (2002).

Che05

Chen, X. F., He, Z. J., Xiang, J. W. Experiments on crack identification in cantilever beams. Experimental Mechanics, 45, 295-300 (2005).

Chr84

Christides, S., Barr, A. D. S. One-dimensional theory of cracked Bernoulli-Euler beams. International Journal of Mechanical Sciences, 26(11-12), 639-648 (1984).

Chi01

Chinchalkar, S. Determination of crack location in beams using natural frequencies. Journal of Sound and Vibration, 247(3), 417-429 (2001).

Chi21

Chinka, S. S. B., Putti, S. R., Adavi, B. K. Modal testing and evaluation of cracks on cantilever beam using mode shape curvatures and natural frequencies. In Structures (Vol. 32, pp. 1386-1397) Elsevier (2021).

Cho01

Chondros, T. G. The continuous crack flexibility model for crack identification. Fatigue & Fracture of Engineering Materials & Structures, 24(10), 643-650 (2001).

Dad03

Dado, M. H. F., Abuzeid, O. Coupled transverse and axial vibratory behaviour of cracked beam with end mass and rotary inertia. Journal of Sound and Vibration, 261(4), 675-696 (2003).

Dar04

Darpe, A. K., Gupta, K., Chawla, A. Coupled bending, longitudinal and torsional vibrations of a cracked rotor. Journal of Sound and Vibration, 269(1-2), 33-60 (2004).

Dah17

Dahak, M., Touat, N., Benseddiq, N. On the classification of normalized natural frequencies for damage detection in cantilever beam. Journal of Sound and Vibration, 402, 70-84 (2017).

Das18

Das, M. T., Yılmaz, A. Experimental modal analysis of curved composite beam with transverse open crack. Journal of Sound and Vibration, 436, 155-164 (2018).

Der21

De Rosa, M. A., Lippiello, M. Closed-form solutions for vibrations analysis of cracked Timoshenko beams on elastic medium: An analytically approach. Engineering Structures, 236, 111946 (2021).

Dim83

Dimarogonas, A. D., Papadopoulos, C. A. Vibration of cracked shafts in bending. Journal of Sound and Vibration, 91(4), 583-593 (1983).

Dim96

Dimarogonas, A. D. Vibration of cracked structures: a state of the art review. Engineering Fracture Mechanics, 55(5), 831-857 (1996).

Doy89

J.F. Doyle, Wave Propagation in Structures, Springer, New York, NY, (1989).

Fan11

Fan, W., Qiao, P. Vibration-based damage identification methods: a review and comparative study. Structural Health Monitoring, 10(1), 83-111 (2011).

Fer02

Fernandez-Saez, J., Navarro, C. Fundamental frequency of cracked beams in bending vibrations: an analytical approach. Journal of Sound and Vibration, 256(1), 17-31 (2002)

Fer99

Fernandez-Saez, J., Rubio, L., & Navarro, C. Approximate calculation of the fundamental frequency for bending vibrations of cracked beams. Journal of Sound and Vibration, 225(2), 345-352 (1999).

Fun65

Fung, Y. C. Foundation of Solid Mechanics, Englewood Cliffs, NJ, (1965).

Gom14

Gomes, H. M., de Almeida, F. J. F. An analytical dynamic model for single-cracked beams including bending, axial stiffness, rotational inertia, shear deformation and coupling effects. Applied Mathematical Modelling, 38(3), 938-948 (2014).

Gud83

Gudmundson, P. The dynamic behaviour of slender structures with cross-sectional cracks. Journal of the Mechanics and Physics of Solids, 31(4), 329-345 (1983).

Jog20

Joglekar, D. M. Analysis of nonlinear frequency mixing in Timoshenko beams with a breathing crack using wavelet spectral finite element method. Journal of Sound and Vibration, 488, 115532 (2020).

Kan16

Kang, J.K. Predicting the natural frequencies of a cracked beam considering axial–bending coupling from wave propagation perspective, M.S. Thesis, Dong-A University South Korea, (2016)

Kan19

Kang, J.K., Lim, T., Park, H. W. Predicting the modal frequencies of a cracked beam considering axial-bending coupling, Transactions of the Korean Society for Noise and Vibration Engineering29 (2) 270-279 (2019)

Kas08

Kasper, D. G., Swanson, D. C., Reichard, K. M. Higher-frequency wavenumber shift and frequency shift in a cracked, vibrating beam. Journal of Sound and Vibration, 312(1-2), 1-18 (2008).

Kha09

Khaji, N., Shafiei, M., Jalalpour, M. Closed-form solutions for crack detection problem of Timoshenko beams with various boundary conditions. International Journal of Mechanical Sciences, 51(9-10), 667-681 (2009).

Kim03a

Kim, J. T., Ryu, Y. S., Cho, H. M., Stubbs, N. Damage identification in beam-type structures: frequency-based method vs mode-shape-based method. Engineering Structures, 25(1), 57-67 (2003).

Kim03b

Kim, J. T., Stubbs, N. Crack detection in beam-type structures using frequency data. Journal of Sound and Vibration, 259(1), 145-160 (2003).

Kim18

Kim, K., Kim, S., Sok, K., Pak, C., Han, K. A modeling method for vibration analysis of cracked beam with arbitrary boundary condition. Journal of Ocean Engineering and Science, 3(4), 367-381 (2018).

Kra03

Krawczuk, M., Palacz, M., Ostachowicz, W. The dynamic analysis of a cracked Timoshenko beam by the spectral element method. Journal of Sound and Vibration, 264(5), 1139-1153 (2003).

Lee00

Lee, Y. S., Chung, M. J. A study on crack detection using eigenfrequency test data. Computers & Structures, 77(3), 327-342 (2000).

Lee18

R. Lee, ABAQUS for Engineer: A Practical Guide, PUBPLE; (2018).

Lel02

Lele, S. P., Maiti, S. K. Modelling of transverse vibration of short beams for crack detection and measurement of crack extension. Journal of Sound and Vibration, 257(3), 559-583 (2002).

Li02

Li, Q. S. Free vibration analysis of non-uniform beams with an arbitrary number of cracks and concentrated masses. Journal of Sound and Vibration, 252(3), 509-525 (2002).

Lia92

Liang, R. Y., Hu, J., Choy, F. Theoretical study of crack-induced eigenfrequency changes on beam structures. Journal of Engineering Mechanics, 118(2), 384-396 (1992).

Lin04

Lin, H. P. Direct and inverse methods on free vibration analysis of simply supported beams with a crack. Engineering Structures, 26(4), 427-436 (2004).

Liu13

Liu, X. L., Jiang, Z. W., Ji, L. Investigation on the design of piezoelectric actuator/sensor for damage detection in beam with lamb waves. Experimental Mechanics, 53, 485-492 (2013).

Liu20

Liu, B., Yang, J., Gang, T. Analysis of sound and vibration interaction on a crack and its use in high-frequency parameter selection for vibro-acoustic modulation testing. Mechanical Systems and Signal Processing, 143, 106835 (2020).

Loy06

Loya, J. A., Rubio, L., Fernández-Sáez, J. Natural frequencies for bending vibrations of Timoshenko cracked beams. Journal of Sound and Vibration, 290(3-5), 640-653 (2006).

Loy22

Loya, J. A., Aranda-Ruiz, J., Zaera, R. Natural frequencies of vibration in cracked Timoshenko beams within an elastic medium. Theoretical and Applied Fracture Mechanics, 118, 103257 (2022).

Lev72

Levy, N., Rice, J. R. The part-through surface crack in an elastic plate. Journal of Applied Mechanics, 39(1), 185-194 (1972).

Mag19

Magnus, J. R., Neudecker, H. Matrix differential calculus with applications in statistics and econometrics. John Wiley & Sons (2019).

Mas98

Masoud, S., Jarrah, M. A., Al-Maamory, M. Effect of crack depth on the natural frequency of a prestressed fixed–fixed beam. Journal of Sound and Vibration, 214(2), 201-212 (1998).

Mea94

Mead, D. J. Waves and modes in finite beams: application of the phase-closure principle. Journal of Sound and Vibration, 171(5), 695-702 (1994).

Mei05

Mei, C., Mace, B. R. Wave reflection and transmission in Timoshenko beams and wave analysis of Timoshenko beam structures (2005).

Mei06

Mei, C., Karpenko, Y., Moody, S., Allen, D. Analytical approach to free and forced vibrations of axially loaded cracked Timoshenko beams. Journal of Sound and Vibration, 291(3-5), 1041-1060 (2006).

Mon90

Montalvão E Silva, J. M., Aráujo Gomes, A. J. M. Experimental dynamic analysis of cracked free-free beams. Experimental Mechanics, 30, 20-25 (1990).

Mor93

Morassi, A. Crack-induced changes in eigenparameters of beam structures. Journal of Engineering Mechanics, 119(9), 1798-1803 (1993).

Nah05

Nahvi, H., Jabbari, M. Crack detection in beams using experimental modal data and finite element model. International Journal of Mechanical Sciences, 47(10), 1477-1497 (2005).

Nar94

Narkis, Y. Identification of crack location in vibrating simply supported beams. Journal of Sound and Vibration, 172(4), 549-558 (1994).

Ost91

Ostachowicz, W. M., Krawczuk, M. Analysis of the effect of cracks on the natural frequencies of a cantilever beam. Journal of Sound and Vibration, 150(2), 191-201 (1991).

Pap87

Papadopoulos, C. A., Dimarogonas, A. D. Coupled longitudinal and bending vibrations of a rotating shaft with an open crack. Journal of Sound and Vibration, 117(1), 81-93 (1987).

Pap88

Papadopoulos, C. A., Dimarogonas, A. D. Coupled longitudinal and bending vibrations of a cracked shaft. Journal of Vibration and Acoustics, 110 (1), 1-8 (1988).

Par03

Park, G., Sohn, H., Farrar, C. R., Inman, D. J. Overview of piezoelectric impedance-based health monitoring and path forward. Shock and Vibration Digest, 35(6), 451-464 (2003).

Par17

Park, H. W. A simplified frequency equation and its approximate solution of a beam with an incipient crack from a wave perspective. Wave Motion, 75, 1-12 (2017).

Par18

Park, H. W., Lim, T. Investigating a common premise in structural health monitoring: Are higher modal frequencies more sensitive to an incipient crack on a beam than lower ones?. Engineering Structures, 176, 385-395 (2018).

Psi19

PSI-5A4E PIEZOCERAMIC SHEETS and their properties. www.piezo.com/prodsheet1sq5A.html (accessed 01 April 2019).

Riz90

Rizos, P. F., Aspragathos, N., Dimarogonas, A. D. Identification of crack location and magnitude in a cantilever beam from the vibration modes. Journal of Sound and Vibration, 138(3), 381-388 (1990).

Sal97

Salawu, O. S. Detection of structural damage through changes in frequency: a review. Engineering Structures, 19(9), 718-723 (1997).

Sar14

Sarfaraz, E., Hamidzadeh, H.R., Analytical Verification for Vibration Analysis Technique used in Determination of Cracking in Cantilever Beams, Materials Evaluation 72 (2), 11-21 (2014).

Sat17

Satpute, D., Baviskar, P., Gandhi, P., Chavanke, M., Aher, T. Crack detection in cantilever shaft beam using natural frequency. Materials Today: Proceedings, 4(2), 1366-1374 (2017).

Sha11

Shafiei, M., Khaji, N. Analytical solutions for free and forced vibrations of a multiple cracked Timoshenko beam subject to a concentrated moving load. Acta Mechanica, 221(1-2), 79-97 (2011).

She90

Shen, M. H., Pierre, C. Natural modes of Bernoulli-Euler beams with symmetric cracks. Journal of Sound and Vibration, 138(1), 115-134 (1990).

She94

Shen, M. H., Pierre, C. Free vibrations of beams with a single-edge crack. Journal of Sound and Vibration, 170(2), 237-259 (1994).

Shi99

Shifrin, E. I., Ruotolo, R. Natural frequencies of a beam with an arbitrary number of cracks. Journal of Sound and Vibration, 222(3), 409-423 (1999).

Tad20

H. Tada, P.C. Paris, G. R. Irwin, The stress analysis of cracks. Handbook, 2. New York: ASME Press; (2000).

Tsa96

Tsai, T. C., Wang, Y. Z.. Vibration analysis and diagnosis of a cracked shaft. Journal of Sound and Vibration, 192(3), 607-620 (1996)

Vio07

Viola, E., Ricci, P., Aliabadi, M. H. Free vibration analysis of axially loaded cracked Timoshenko beam structures using the dynamic stiffness method. Journal of Sound and Vibration, 304(1-2), 124-153 (2007).

Wan15

Wang, K., Wang, B. Timoshenko beam model for the vibration analysis of a cracked nanobeam with surface energy. Journal of Vibration and Control, 21(12), 2452-2464 (2015).

Wan12

Wang, C. S., Lee, L. T. Modified and simplified sectional flexibility of a cracked beam. Journal of Applied Mathematics, (2012).

Wor07

Worden, K., Farrar, C. R., Manson, G., Park, G. The fundamental axioms of structural health monitoring. Proceedings of the Royal Society A: Mathematical, Physical and Engineering Sciences, 463(2082), 1639-1664 (2007).

Abstract

Modal Behavior of a Two-Dimensional Beam with a Transverse Crack: An Analytical Approach Considering Mode I and II Loadings with Experimental Verification Using Surface-Bonded Piezoelectric Wafers

by
LIM TAE JEONG

Dept. of Civil Engineering
Graduate School, Dong-A University
Busan, Korea

This study proposes a new analytical model capable of predicting the modal frequencies of two-dimensional beams with a transverse crack, regardless of the aspect ratio of the beam and crack location. The conventional method used by most researchers predicts the modal frequencies by considering only the discontinuity of the rotational angles on either side of the crack. The conventional method produces errors in the prediction of modal frequencies, especially for beams with low aspect ratios and higher-numbered bending modes. Since accurate modal frequency prediction is essential for structural health monitoring, these errors limit the use of the equations of the conventional method. Therefore, there is a need for an analysis model that can accurately analyze beams with all open-edge transverse cracks and overcome the limitations of the conventional method.

Since the importance of shear deformation and rotational inertia becomes more

pronounced in situations with increasing mode numbers or low aspect ratios, a spectral solution based on the Timoshenko beam theory is presented. For a two-dimensional crack, the reduction in frequency occurs simultaneously with the axial-bending modal coupling caused by the mode I crack and the effects of the shear mode introduced by the mode II crack. Based on this, a frequency equation is proposed that considers the axial-bending-shear modal coupling. This equation uses compatibility equations for discontinuities in the rotational angle, axial displacement, and transverse displacement in a crack. The proposed method is validated by comparing it with the results of finite element analysis and experiments, varying the crack position and support conditions. In addition, the calculated modal frequencies were applied to the spectral solutions on both sides of the crack to predict the mode shapes, and the crack opening phenomena and shear mode were visually observed.

In this study, we perform experimental verification by transmitting and receiving signals using surface-bonded piezoelectric wafers. This approach has two main advantages. First, the use of surface-bonded piezoelectric wafers allows the simultaneous acquisition of the axial and bending modes, thereby increasing the efficiency of the experiment. Second, this method allows the measurement of a wide range of frequencies within the cut-off frequency, thereby expanding the scope of experimental verification.

The compatibility equations used in the proposed method involve five local flexibilities. By activating these local flexibilities, it is possible to derive a closed-form frequency equation for predicting modal frequencies under specific conditions. First, a closed-form frequency equation is proposed for cases where the crack is located at the bending antinode, by activating only the local flexibilities corresponding to the mode I crack. Second, a closed-form frequency equation is presented for cases where the crack is located at the bending node, which is achieved by activating only the local flexibility corresponding to the mode II crack. In particular, an approximate solution was used to show that the assumption of no frequency reduction when the crack is located at the bending node does not hold. The closed-form frequency equations were validated by applying them to numerical

examples in which the crack is located at the center of the beam and comparing the results with those of finite element analysis and experiment. Through this approach, the role of local flexibilities in relation to crack location is clarified, and it is anticipated to make a significant contribution to the damage diagnosis of structures.

Key word: Axial-bending-shear modal coupling, Timoshenko beam theory, Cracked beam, Open crack mode (mode I crack), Sliding crack mode (mode II crack), Modal frequency, Frequency equation, Surface-bonded piezoelectric wafers, Mode shapes, Local flexibility, Damage diagnosis, Structural health monitoring.